



## **JAEA-Tokai Tandem Annual Report 2011**

**April 1, 2011 – March 31, 2012**

---

Department of Research Reactor and Tandem Accelerator

Nuclear Science Research Institute  
Tokai Research and Development Center

**April 2013**

**Japan Atomic Energy Agency**

日本原子力研究開発機構

# JAEA-Review

本レポートは独立行政法人日本原子力研究開発機構が不定期に発行する成果報告書です。  
本レポートの入手並びに著作権利用に関するお問い合わせは、下記あてにお問い合わせ下さい。  
なお、本レポートの全文は日本原子力研究開発機構ホームページ（<http://www.jaea.go.jp>）  
より発信されています。

独立行政法人日本原子力研究開発機構 研究技術情報部 研究技術情報課  
〒319-1195 茨城県那珂郡東海村白方白根 2 番地 4  
電話 029-282-6387, Fax 029-282-5920, E-mail: ird-support@jaea.go.jp

This report is issued irregularly by Japan Atomic Energy Agency  
Inquiries about availability and/or copyright of this report should be addressed to  
Intellectual Resources Section, Intellectual Resources Department,  
Japan Atomic Energy Agency  
2-4 Shirakata Shirane, Tokai-mura, Naka-gun, Ibaraki-ken 319-1195 Japan  
Tel +81-29-282-6387, Fax +81-29-282-5920, E-mail: ird-support@jaea.go.jp

## **JAEA-Tokai Tandem Annual Report 2011**

**April 1, 2011 – March 31, 2012**

### **Department of Research Reactor and Tandem Accelerator**

Nuclear Science Research Institute  
Tokai Research and Development Center  
Japan Atomic Energy Agency  
Tokai-mura, Naka-gun, Ibaraki-ken

(Received January 23, 2013)

The JAEA-Tokai tandem accelerator complex has been used in various research fields such as nuclear science and material science by researchers not only of JAEA but also from universities, research institutes and industrial companies. This annual report covers developments of accelerators and research activities carried out using the tandem accelerator, superconducting booster, and radioactive nuclear beam accelerator, from April 1, 2011 to March 31, 2012. Twenty-seven summary reports were categorized into seven research/development fields:

- (1) accelerator operation and development
- (2) nuclear structure
- (3) nuclear reaction
- (4) nuclear chemistry
- (5) nuclear theory
- (6) atomic physics and solid state physics
- (7) radiation effects in materials.

This report also lists publications, meetings, personnel, committee members, cooperative researches and common use programs.

Keywords : JAEA-Tokai Tandem Accelerator, Operation Results, Nuclear Structure, Nuclear Reaction, Nuclear Chemistry, Nuclear Theory, Atomic Physics, Solid State Physics, Radiation Effects in Materials, Progress Report

---

Editors: Katsuhisa NISHIO, Kazuaki TSUKADA, Norito ISHIKAWA,  
Yosuke TOH, Hiroyuki KOURA and Makoto MATSUDA

## 原子力機構東海タンデム加速器 2011 年度年次報告

日本原子力研究開発機構  
東海研究開発センター原子力科学研究所  
研究炉加速器管理部

(2013 年 1 月 23 日受理)

原子力機構東海タンデム加速器施設は、原子核科学や物質科学などの様々な分野において、原子力機構を始めとして、大学や公立研究機関、民間企業に利用されている。本年次報告書は、タンデム加速器、ブースター加速器、放射性核種加速装置を利用し、2011 年 4 月 1 日から 2012 年 3 月 31 日までの期間に実施された研究活動の英文要約をまとめたものである。総数 27 件の要約を下記の 7 部門に分類した。

- (1) 加速器の運転状況と開発
- (2) 原子核構造
- (3) 原子核反応
- (4) 核化学
- (5) 原子核理論
- (6) 原子物理及び固体物理
- (7) 材料の照射効果

また、発表論文と会議での口頭発表、タンデム加速器に関与した職員、タンデム加速器専門部会委員、大学等との共同研究課題、及び施設共用課題のリストを掲載した。

---

原子力科学研究所：〒319-1195 茨城県那珂郡東海村白方白根 2-4

編集者：西尾 勝久、小浦 寛之、石川 法人、藤 暢輔、塚田 和明、松田 誠

## Foreword

This report covers research and development activities with the tandem accelerator and its superconducting booster at JAEA Tokai, for the period of FY 2011 (April 1, 2011 to March 31, 2012). The tandem accelerator was operated over a total of 106 days and delivered 18 different ion beams to experiments in the fields of nuclear physics, nuclear chemistry, atomic physics, solid state physics and radiation effects in materials.

A massive earthquake, named “*The 2011 off the Pacific coast of Tohoku Earthquake*”, hit us on March 11, 2011. The accelerator column withstood the earthquake with the help of quake-absorbers attached to its bottom, and no acceleration tubes were damaged. However, thirty three column posts out of 240 had a crack, a vacuum leak happened at the terminal ion source, and the beam line of the superconducting booster lost its proper alignment. By recovering these damages as quickly as possible, we were able to open the tandem accelerator for experiment on September 15, 2011. We would express sincere thanks for kind support and encouragement received in this severe time.

The following are the highlights in FY 2011:

*In the field of accelerator development:* The NRA experiment system using the BGO detector of 3 "x3" was installed at the H1 beam line. The energy calibration of the tandem accelerator was performed using  $^{15}\text{N}+\text{H}$  resonance reaction. The indication energy of the accelerator was found to be 3 keV (0.05%) higher than the resonance energy of 6.385 MeV.

*In the field of nuclear structure:* In order to study the shape phase transition from vibrational (U(5)) to  $\gamma$ -unstable (O(6)) nuclei, Coulomb excitation experiments of  $^{128}\text{Xe}$  and  $^{130}\text{Xe}$  beams were performed with  $^{208}\text{Pb}$  target. De-excitation  $\gamma$ -rays of  $^{128}\text{Xe}$  and  $^{130}\text{Xe}$  were observed eight and six, respectively.

*In the field of nuclear reactions:* Surrogate reaction method was used to determine the neutron-induced fission cross sections of  $^{239}\text{U}$  having a half-life of 23.5 min from the reaction of  $^{238}\text{U}(^{18}\text{O}, ^{16}\text{O}) ^{240}\text{U}^*$ . This method was studied to determine the capture cross sections.

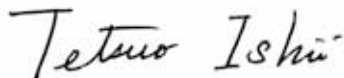
*In the field of nuclear chemistry:*  $^{256}\text{Lr}$  atoms were successfully ionized and mass-separated using a newly designed surface ionization source at the JAEA-ISOL, which allows us to gain the 1st ionization potential of Lr. Radiotracers produced at the tandem accelerator were used to determine the detector efficiency for the measurement of radioisotope,  $^{131}\text{I}$ , discharged by the accident of the Fukushima Daiichi Nuclear Power Plant.

*In the field of nuclear theory:* The evolution of the shell structure is studied in a full  $1\hbar\omega$  shell model framework. Considering the tensor force of the nuclear force, the location of  $0g_{9/2}$  orbit in calcium isotopes

was evaluated and the  $3^-$  excitation energy was calculated. It reproduces well experimental trends. Furthermore, a new phenomenological relation between Q-values and half-lives of alpha decay was presented. This formula estimates two or three times longer half-lives and closer to experimental ones than those of the Viola-Seaborg formula, which is one of conventional formulae, in the superheavy mass region.

*In the field of atomic physics and solid-state physics:* Equilibrium and non-equilibrium charge state distributions were measured for 2 MeV/u  $C^{q+}$  ( $q=2-6$ ) projectile ions penetrating through 0.9-200  $\mu\text{g}/\text{cm}^2$  thick carbon films. For  $C^{2-5+}$  projectile ions, all the measured charge fractions except for  $C^{6+}$  charge fraction showed maxima as a function of film thickness in the non-equilibrium region.

*In the field of radiation effects in materials:* In order to realize mass-production of the evanescent-field-coupled waveguide-mode (EFC-WM) sensor, large area irradiation setup is developed at the beamline of the tandem accelerator. As a result, wide irradiation with a width of 50 mm was achieved. Ion-irradiated single crystalline  $\text{Ba}(\text{Fe}_{0.5}\text{Mn}_{0.5})\text{O}_{3.8}$  thin films showed close correlation between the lattice constant and the saturation magnetization. The observed correlation has the same trend observed for the thermally treated samples with different oxygen deficiencies, suggesting that the magnetic property of this material is determined by the irradiation-induced oxygen deficiencies.



---

Tetsuro ISHII, Deputy Director, Department of Research Reactor and Tandem Accelerator

## Contents

1. ACCELERATOR OPERATION AND DEVELOPMENT .....	1
1.1 Operation and usage of tandem accelerator and booster .....	3
A. Osa, Y. Tsukihashi, S. Hanashima, S. Abe, T. Ishii, N. Ishizaki, H. Tayama, M. Matsuda, T. Nakanoya, H. Kabumoto, M. Nakamura, K. Kutsukake, Y. Otokawa and T. Asozu	
1.2 Re-alignment of superconducting booster .....	5
H. Kabumoto, N. Ishizaki, M. Matsuda, S. Takeuchi, T. Yoshida, K. Yamaguchi and R. Nukaga	
1.3 Development of the hydrogen analysis technique using the $^{15}\text{N}$ -NRA method .....	7
M. Matsuda, A. Asozu and M. Sataka	
2. NUCLEAR STRUCTURE .....	9
2.1 Coulomb Excitation Experiment of $^{128,130}\text{Xe}$ .....	11
M. Koizumi, Y. Toh, M. Oshima, A. Kimura, Y. Hatsukawa, K. Furutaka, H. Harada, F. Kitatani, S. Nakamura, M. Sugawara and E. Ideguchi	
3. NUCLEAR REACTION .....	13
3.1 Fission of proton-rich mercury nuclei populated by fusion reaction .....	15
A. Andreyev, K. Nishio, J. Benlliure, M. Caamano, X. Derkx, L. Guys, F.P. Heßberger, B. Kindler, J. Lane, V. Liberati, B. Lommel, H. Makii, S. Mitsuoka, T. Nagayama, I. Nishinaka, S. Ohta, T. Ohtsuki, K. Sandhu, P. Van Dupen, M. Veselsky and Y. Wakabayashi	
3.2 Measurement of fission cross section for $^{239}\text{U}(\text{n},\text{f})$ using surrogate reaction method .....	17
K. Nishio, T. Nagayama, I. Nishinaka, S. Mitsuoka, H. Makii, Y. Wakabayashi, S. Ohta, K. Furutaka, K. Tsukada, M. Asai, S. Chiba, T. Ishii and T. Ohtsuki	
3.3 Surrogate ratio method for determination of $(\text{n},\gamma)$ cross sections .....	19
H. Makii, T. Ishii, S. Ota, Y. Wakabayashi, M. Asai, K. Furutaka, K. Nishio, S. Mitsuoka, I. Nishinaka and S. Chiba	
3.4 Measurement of grazing angles of $^{136}\text{Xe}+^{198}\text{Pt}$ at energy region around Coulomb barrier .....	21
Y.X. Watanabe, H. Miyatake, S.C. Jeong, H. Ishiyama, Y. Hirayama, S. Mitsuoka, K. Nishio, Y. Wakabayashi, H. Makii and I. Nishinaka	
3.5 Fission fragment anisotropy in heavy-ion-induced fission of actinide nuclei .....	23
I. Nishinaka, M. Tanikawa, K. Nishio, H. Makii, S. Mitsuoka, Y. Wakabayashi and A. Yokoyama	
3.6 Measurement of branching ratio of $^{22}\text{Ne}(\alpha, \gamma)^{26}\text{Mg} / ^{22}\text{Ne}(\alpha, \text{n})^{25}\text{Mg}$ reactions .....	24
S. Ota, H. Makii, T. Ishii, K. Nishio, S. Mitsuoka, I. Nishinaka and S. Chiba	

4. NUCLEAR CHEMISTRY .....	27
4.1 First successful ionization of Lr applying an ISOL-technique with an improved surface-ionization type ion-source .....	29
N. Sato, T.K. Sato, M. Asai, K. Tsukada, A. Toyoshima, K. Ooe, Y. Kaneya, Y. Nagame, S. Ichikawa, M. Schädel, A. Osa, T. Stora and J.V. Kratz	
4.2 Studies on isothermal chromatographic behavior of volatile compounds of Hf isotopes with various half-lives .....	31
S. Goto, T. Kojima, T. Tomitsuka, M. Murakami, H. Kudo, K. Tsukada, M. Asai, T. K. Sato, A. Toyoshima, K. Ooe, Y. Kanaya and Y. Nagame	
4.3 Production and utilization of radioactive astatine isotopes using lithium ion beams .....	33
I. Nishinaka, A. Yokoyama, K. Washiyama, R. Amano, N. Yamada, E. Maeda, K. Li, N.S. Ishioka, K. Hashimoto, S. Watanabe, A. Toyoshima and H. Makii	
4.4 Production of medical radio isotope, $^{95m}\text{Tc}$ . (II) .....	35
Y. Hatsukawa, K. Hashimoto, K. Tsukada, T. Sato, M. Asai, T. Kin, A. Toyoshima and Y. Nagai	
4.5 Measurement of radioisotopes on soil in Ibaraki prefecture discharged by the accident of the Fukushima Daiich Nuclear Power Plant .....	37
T. K. Sato, Y. Kaneya, M. Asai, K. Tsukada, A. Toyoshima, N. Sato, K. Ooe, Y. Miyamoto, K. Yasuda, K. Ninomiya, M. Matsuda, S. Mitsuoka, H. Ishiyama and Y. Nagame	
5. NUCLEAR THEORY .....	39
5.1 Location of the neutron $g_{9/2}$ orbit in neutron-rich calcium isotopes .....	41
Y. Utsuno, T. Otsuka, N. Shimizu, T. Mizusaki and M. Honma	
5.2 Dynamical approach to heavy-ion induced fission using actinide target nuclei at energies around the Coulomb barrier .....	43
Y. Aritomo, K. Hagino, S. Chiba and K. Nishio	
5.3 Phenomenological formula for alpha-decay half-lives .....	45
H. Koura	
6. ATOMIC PHYSICS AND SOLID STATE PHYSICS .....	47
6.1 Charge state distribution of carbon ions after penetration of C-foil targets (II) .....	49
M. Imai, M. Sataka, K. Kawatsura, K. Takahiro, K. Komaki, K. Nishio and H. Shibata	
6.2 Effective charge of high-energy heavy ions in $\text{WO}_3$ and W .....	51
N. Matsunami, M. Sataka and S. Okayasu	



7.	RADIATION EFFECTS IN MATERIALS .....	53
7.1	Dependence of ion-track size on the electronic stopping power in ion-irradiated $\text{UO}_2$ .....	55
	N. Ishikawa, T. Sonoda, T. Sawabe and M. Sataka	
7.2	Preliminary evaluation of high energy ion irradiation effects on electrical resistivity of ceramics .....	57
	N. Okubo, N. Ishikawa, M. Sataka and S. Jitsukawa	
7.3	Shape and property control of metal nanoparticles by swift heavy ion irradiation .....	59
	H. Amekura, N. Okubo and N. Ishikawa	
7.4	Swift heavy ion irradiation effect on structural and magnetic properties for epitaxial $\text{Ba}(\text{Fe}_{0.5}\text{Mn}_{0.5})\text{O}_{3-\delta}$ thin films .....	61
	R. Shinoda, T. Matsui, N. Ishikawa and A. Iwase	
7.5	Nano-fabrication on Ag-Zeolite using high energy heavy ion radiation .....	63
	S. Okayasu and Y. Sasaki	
7.6	Application of high-aspect-ratio nanoholes formed by etching of latent tracks for sensors .....	64
	M. Fujimaki, M. Sataka and M. Matsuda	
7.7	Influence of multiple angled columnar defects on flux pinning properties in YBCO thin films .....	66
	T. Sueyoshi, T. Nishimura, T. Fujiyoshi, F. Mitsugi, T. Ikegami and N. Ishikawa	
8.	PUBLICATION IN JOURNAL AND PROCEEDINGS, AND CONTRIBUTION TO SCIENTIFIC MEETINGS .....	69
8.1	Accelerator Operation and Development .....	71
8.2	Nuclear Structure .....	72
8.3	Nuclear Reaction .....	73
8.4	Nuclear Chemistry .....	75
8.5	Nuclear Theory .....	78
8.6	Atomic Physics and Solid-state Physics .....	82
8.7	Radiation Effects in Materials .....	83
9.	PERSONNEL AND COMMITTEE .....	87
9.1	Personnel .....	89
9.2	Research Planning and Assessment Committee .....	92
10.	NEW RESEARCH PROGRAMS .....	93
10.1	New Research Programs Approved in the FY2011 .....	95
10.2	New Research Programs Approved in the FY2010 .....	97

## 目 次

1. 加速器の運転状況及び開発 .....	1
1.1 タンデム加速器とブースターの運転及び利用状況 .....	3
長 明彦、月橋 芳廣、花島 進、阿部 信市、石井 哲朗、石崎 暢洋、田山 豪一、 松田 誠、仲野谷 孝充、株本 裕史、中村 暢彦、杳掛 健一、乙川 義憲、遊津 拓洋	
1.2 超伝導ブースターの再アライメント .....	5
株本 裕史、石崎 暢洋、松田 誠、竹内 末広、吉田 崇宏、山口 和司、額賀 凌	
1.3 $^{15}\text{N}$ -NRA 法による水素分析技術の開発 .....	7
松田 誠、遊津 拓洋、左高 正雄	
2. 原子核構造 .....	9
2.1 $^{128,130}\text{Xe}$ のクーロン励起実験 .....	11
小泉 光生、藤 暢輔、大島 真澄、木村 敦、初川 雄一、古高 和禎、 原田 秀郎、北谷 文人、中村 詔司、菅原 昌彦、井手口 栄治	
3. 原子核反応 .....	13
3.1 重イオン反応による陽子過剰水銀原子核の核分裂 .....	15
A. Andreyev、西尾 勝久、J. Benlliure、M. Caamano、X. Derkx、L. Guys、F. P. Heßberger、 B. Kindler、J. Lane、V. Liberati、B. Lommel、牧井 宏之、光岡 真一、永山 達郎、 西中 一郎、太田 周也、大槻 勤、K. Sandhu、P. Van Dupen、M. Veselsky、若林 泰夫	
3.2 代理反応法による $^{239}\text{U}(\text{n}, \text{f})$ の核分裂断面積の測定 .....	17
西尾 勝久、永山 達郎、西中 一郎、光岡 真一、牧井 宏之、若林 泰夫、 太田 周也、古高 和禎、塚田 和明、浅井 雅人、千葉 敏、石井 哲朗、大槻 勤	
3.3 代理比反応法による中性子捕獲断面積の導出 .....	19
牧井 宏之、石井 哲朗、太田 周也、若林 泰生、浅井 雅人、古高 和禎、 西尾 勝久、光岡 真一、西中 一郎、千葉 敏	
3.4 クーロン障壁近傍のエネルギー領域における $^{136}\text{Xe}+^{198}\text{Pt}$ のかすり角の測定 .....	21
渡辺 裕、宮武 宇也、鄭 淳讃、石山 博恒、平山 賀一、光岡 真一、 西尾 勝久、若林 泰生、牧井 宏之、西中 一郎	
3.5 アクチノイド原子核の重イオン誘起核分裂における分裂片角度異方性 .....	23
西中 一郎、谷川 勝至、西尾 勝久、牧井 宏之、光岡 真一、若林 泰生、横山 明彦	
3.6 $^{22}\text{Ne}(\alpha, \gamma)^{26}\text{Mg}/^{22}\text{Ne}(\alpha, \text{n})^{25}\text{Mg}$ 分岐比の測定 .....	24
太田 周也、牧井 宏之、石井 哲朗、西尾 勝久、光岡 真一、西中 一郎、千葉 敏	
4. 核化学 .....	27
4.1 改良型表面電離イオン源および ISOL を用いた Lr のイオン化 .....	29
佐藤 望、佐藤 哲也、浅井 雅人、塚田 和明、豊嶋 厚史、 大江 一弘、金谷 佑亮、永日諭一郎、市川 進一、Matthias Schadel、 長 明彦、Thierry Stora、Jens Volker Kratz	

4.2	種々の半減期をもつ Hf 揮発性化合物の等温クロマトグラフィ挙動に関する研究	31
	後藤 真一、小嶋 貴幸、富塚 知博、村山 昌史、工藤 久昭、塚田 和明、 浅井 雅人、佐藤 哲也、豊嶋 厚史、大江 一弘、金谷 佑亮、永目 諭一郎	
4.3	リチウムイオンビームによる放射性アスタチンの合成と利用	33
	西中 一朗、横山 明彦、鷺山 幸信、天野 良平、山田 記大、前田 英太、 李 恵子、石岡典子、橋本 和幸、渡邊 茂樹、豊嶋 厚史、牧井 宏之	
4.4	加速器による医療用 RI 生成-II	35
	初川 雄一、橋本 和幸、塚田 和明、佐藤 哲也、浅井 雅人、金 政浩 豊嶋 厚史、永井 泰樹	
4.5	茨城県土壌中の福島第一原子力発電所事故起源放射性核種の測定	37
	佐藤 哲也、金谷 佑亮、浅井 雅人、塚田 和明、豊嶋 厚史、佐藤 望、 大江 一弘、宮本 ユタカ、安田 健一郎、二宮 和彦、松田 誠、光岡 真一、 石山 博恒、永目 諭一郎	
5.	原子核理論	39
5.1	中性子過剰カルシウム同位体における中性子 $g_{9/2}$ 軌道の位置	41
	宇都野 穰、大塚 孝治、清水 則孝、水崎 高浩、本間 道雄	
5.2	クーロンバリア近傍におけるアクチノイド標的核を用いた 重イオン誘起分裂反応に対する動力学的アプローチ	43
	有友 嘉浩、萩野 浩一、千葉 敏、西尾 勝久	
5.3	$\alpha$ 崩壊半減期の現象論的公式	45
	小浦 寛之	
6.	原子物理及び固体物理	47
6.1	高速炭素イオンの炭素薄膜通過による電荷分布変化	49
	今井 誠、左高 正雄、川面 澄、高廣 克己、小牧 研一郎、西尾 勝久、柴田 裕実	
6.2	$WO_3$ 及び W 中の高エネルギー重イオンの有効電荷	51
	松波 紀明、左高 正雄、岡安 悟	
7.	材料の照射効果	53
7.1	イオン照射した $UO_2$ におけるイオントラックサイズの電子的阻止能依存性	55
	石川 法人、園田 健、澤部 孝史、左高 正雄	
7.2	セラミックスの電気抵抗における高エネルギーイオン照射効果の予備評価	57
	大久保 成彰、石川 法人、左高 正雄、實川 資朗	
7.3	高速重イオン照射による Zn 系ナノ粒子の形状・物性制御	59
	雨倉 宏、大久保 成彰、石川 法人	
7.4	高エネルギー重イオン照射が $Ba(Fe_{0.5}Mn_{0.5})O_{3-\delta}$ 単結晶薄膜の構造 及び磁気特性に及ぼす影響	61
	篠田 遼一、松井 利之、石川 法人、岩瀬 彰宏	
7.5	高エネルギー重イオン照射による銀ゼオライトの微細組織形成	63
	岡安 悟、佐々木 優吉	

7.6	潜トラックエッチングにより形成される高アスペクト比ナノ孔のセンサー応用	64
	藤巻 真、左高 正雄、松田 誠	
7.7	YBCO 薄膜の磁束ピンニングに対する複数方向に交差した柱状欠陥の影響	66
	末吉 哲郎、西村 太宏、藤吉 孝則、光木 文秋、池上 知顯、石川 法人	
8.	雑誌及び国際会議等の刊行物、学会発表	69
8.1	加速器の運転状況及び開発	71
8.2	原子核構造	72
8.3	原子核反応	73
8.4	核化学	75
8.5	原子核理論	78
8.6	原子物理及び固体物理	82
8.7	材料の照射効果	83
9.	関連課室職員及び委員会	87
9.1	課室職員	89
9.2	委員会	92
10.	新規研究テーマ	93
10.1	2011 年度に採択された新規研究テーマ	95
10.2	2010 年度に採択された新規研究テーマ	97

## **CHAPTER 1**

### **Accelerator Operation and Development**

- 1.1 Operation and usage of tandem accelerator and booster
- 1.2 Re-alignment of superconducting booster
- 1.3 Development of the hydrogen analysis technique using the  $^{15}\text{N}$ -NRA method

This is a blank page.

## 1.1 Operation and usage of tandem accelerator and booster

A. Osa<sup>1</sup>, Y. Tsukihashi<sup>1</sup>, S. Hanashima<sup>1</sup>, S. Abe<sup>1</sup>, T. Ishii<sup>1</sup>, N. Ishizaki<sup>1</sup>, H. Tayama<sup>1</sup>, M. Matsuda<sup>1</sup>,  
T. Nakanoya<sup>1</sup>, H. Kabumoto<sup>1</sup>, M. Nakamura<sup>1</sup>, K. Kutsukake<sup>1</sup>, Y. Otokawa<sup>1</sup> and T. Asozu<sup>1</sup>

First half of FY2011, we buckled down to repair the tandem accelerator from damages of “*The 2011 off the Pacific coast of Tohoku Earthquake*” on March 11, 2011. The tandem accelerator was opened for experiment on September 15, 2011. It was operated for experiments from September 15, 2011 to December 14, 2011, and from February 13, 2012 to March 31, 2012. The total operation time of the tandem accelerator for FY2011 (from April 1, 2011 to March 31, 2012) was 106 days and 18 different beams were delivered for experiments. The experimental proposal and the usage of the beam times for FY2011 are summarized in Table 1 and Table 2, respectively.

Table 1. Experimental proposals.

Research proposals accepted by the program advisory committee:	
In-house staff proposals	3
Collaboration proposals	17
Number of experiments proposed	33
Total number of scientists participating in research	
from outside	60
in-house	131
Number of institutions presented	24

Table 2. Usage of beam-times  
in different research fields.

Research field	Beam time (days) (%)	
Nuclear physics	38	35.8
Nuclear chemistry	31	29.2
Atomic and materials sciences	22	20.8
Accelerator development	15	14.2
total	106	100

Distributions of the terminal voltages and ion species for experiments are shown in Fig.1 and Fig.2, respectively. Half of the beams were extracted from three negative ion sources, SNICS-2. The proton, carbon, nitrogen, oxygen and rare gases were ionized and extracted from in-terminal ECR ion source. The ECR ion source was used as much as 48% of all the beam time.

The superconducting booster was operated for a total of 9 days to boost the energies of 4 different beams from the tandem accelerator, as is summarized in Table 3. These beams were used for experiments of nuclear physics and accelerator development.

<sup>1</sup> Japan Atomic Energy Agency (JAEA)

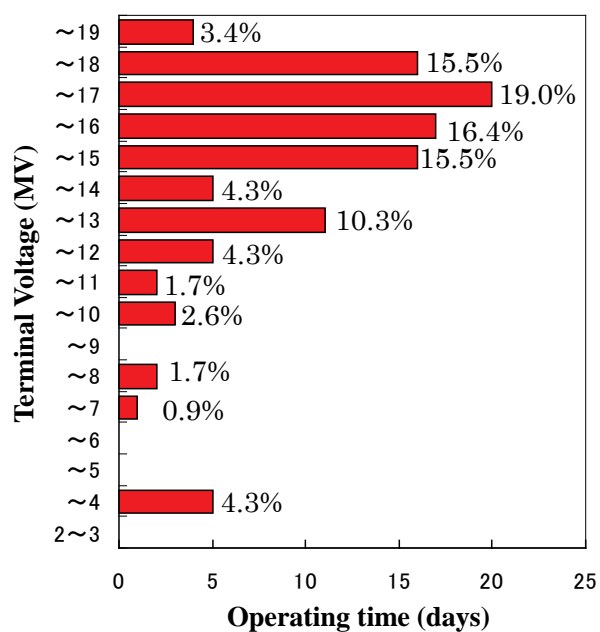


Fig.1 Distribution of terminal voltages.

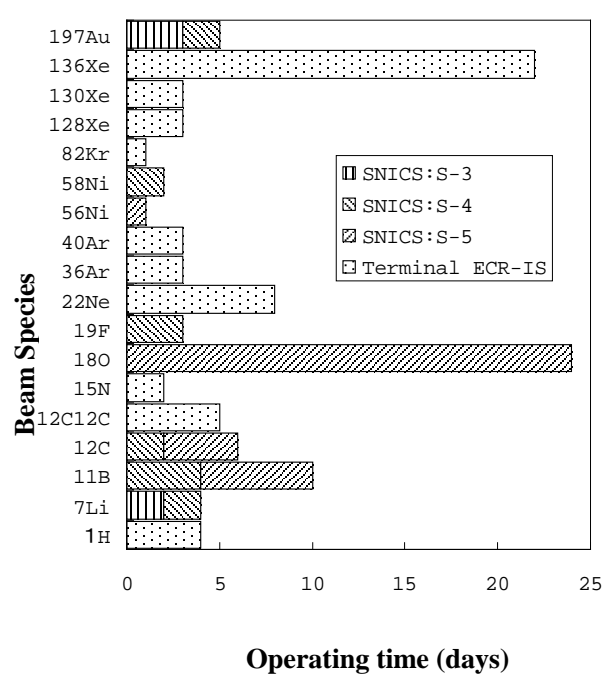


Fig.2 Distribution of beam species accelerated for experiments.

Table 3. Boosted ion beams for experiments.

Beam species	Boosted energies (MeV)	Beam time (days)
<sup>82</sup> Kr	288	1
<sup>128</sup> Xe	548	3
<sup>130</sup> Xe	550	3
<sup>136</sup> Xe	816, 884, 952, 1020	2



## 1.2 Re-alignment of superconducting booster

H. Kabumoto<sup>1</sup>, N. Ishizaki<sup>1</sup>, M. Matsuda<sup>1</sup>, S. Takeuchi<sup>1</sup>, T. Yoshida<sup>2</sup>, K. Yamaguchi<sup>2</sup> and R. Nukaga<sup>2</sup>

The beam-line of superconducting booster lost its proper alignment because of “The 2011 off the pacific coast of Tohoku Earthquake”. In the moment of the earthquake occurred, fortunately both of the superconducting booster and helium refrigerator were not operated, so there was no serious damage in the booster facility. However, this earthquake made the level difference about 10 mm at the joint of the buildings. Figure 1 shows the schematic layout of the tandem and booster building. The building of superconducting booster was extended from the tandem accelerator building in 1992. We had already measured the alignment of superconducting booster in 2010, it has turned out that the booster building has been sagging down a little at the joint of the two buildings. This earthquake made the level difference much bigger. It was difficult to accelerate the beams by superconducting booster, thus we carried out the re-alignment.

The superconducting booster consisted of 40 acceleration resonator and 10 cryostat vessels, each cryostat contained 4 resonators (Fig.3). For the alignment of vertical direction, we jacked up the cryostats so that it became proper position. Figure 2 shows the vertical position of cryostats before and after the alignment. The quantities of jack-up were about 8 mm at the cryostat No.1, and 3 mm at the cryostat No.10. For the alignment of horizontal direction, ‘the alignment metal fittings’ were attached to the beam-line flange of cryostats, and we adjusted the horizontal position by using of optical theodolite. Moreover, we also carried out the adjustment of vertical position of the valve-boxes of helium refrigerator, because it was necessary to attach transfer-line of liquid helium to the upper part of cryostats.

The two heavyweight electromagnets moved 30-40 mm because of the earthquake. One was the energy analyzing electromagnet (BM B4-1, Weight: 14 ton), another was the target-line switching electromagnet (BM B4-2, Weight: 21ton). The anchor bolts for fixing to the floor concrete were broken by movement of the electromagnets, so we made the new anchor bolts around the mount of electromagnets. The vacuum chambers of the electromagnets also moved with the steel yokes together, and it pressed the beam-line bellows by the side of the down stream of beam-line (Fig.4). One of them caused the vacuum break, we changed the broken bellows to new one. And more, the one of jack-assemblies of the electromagnet (BM B4-2) was broken. Although the electromagnet did not fall down, it was impossible to alignment of the electromagnet because the adjustment-screw was torn off. We repaired the jack-assembly after removing it from the electromagnet. After finished the alignment of all accelerator components (cryostat vessels, electromagnetic quadruples, electromagnetic steerers, beam profile monitors, apertures, and etc), we checked the beam-pass without acceleration in October. The experiments of using the superconducting booster started in November, which could accelerate the beams satisfactorily up to the present.

---

<sup>1</sup> Japan Atomic Energy Agency (JAEA)

<sup>2</sup> Atox co., ltd.

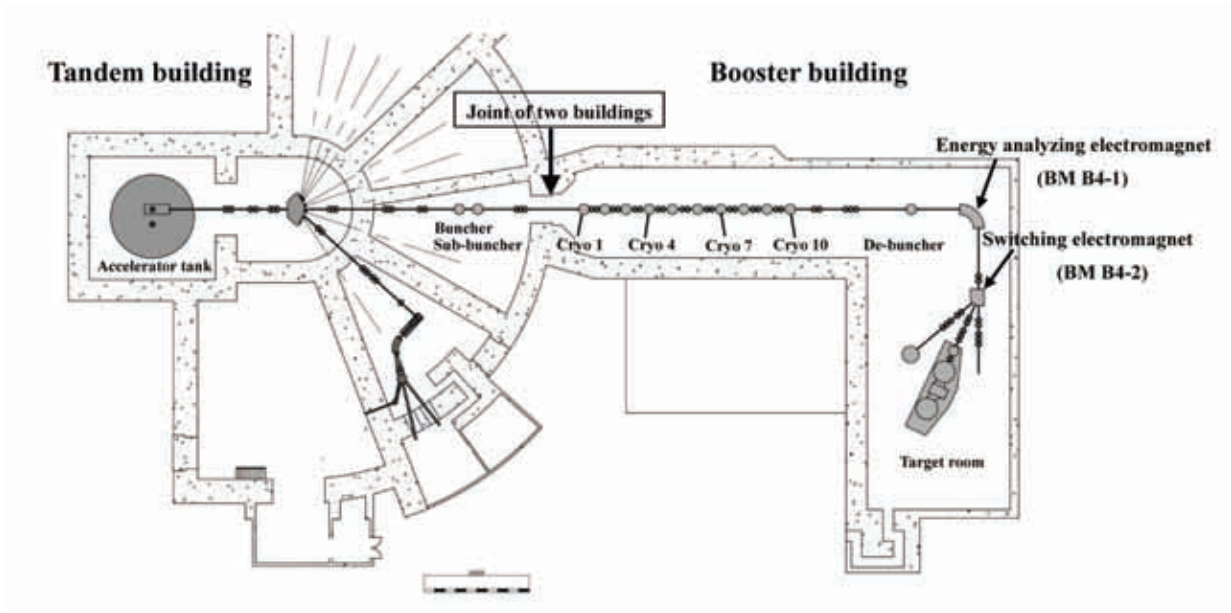


Fig. 1 Schematic layout of the tandem and booster building.

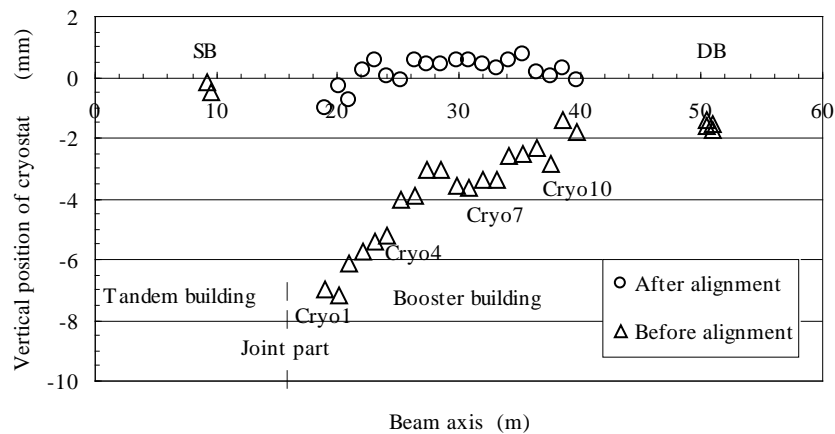


Fig. 2 The vertical position of cryostats before and after the alignment.



Fig. 3 Schematic view of cryostats of the superconducting booster. The back side of this picture is joint of the buildings.



Fig.4 The bellow pressed by the vacuum chamber of the electromagnet, it caused the vacuum break.

### 1.3 Development of the hydrogen analysis technique using the $^{15}\text{N}$ -NRA method

M. Matsuda<sup>1</sup>, A. Asozu<sup>1</sup> and M. Sataka<sup>1</sup>

The NRA (Nuclear Reaction Analysis) experiment system using the BGO detector of 3 "x3" was installed at the H1 beam line. This NRA system uses  $^{15}\text{N}+\text{H}$  or  $^{19}\text{F}+\text{H}$  reaction. The distance from a measurement sample to the detector surface is 17 mm or 29 mm, when a detector is put on 0-degree or 90-degree to a beam axis. According to GEANT4 simulation, the detection efficiency of the photo peak in each position is 6.93% and 4.48% to the gamma ray of 4.43 MeV. The detection efficiency of the energy more than Double escape energy is 11.7% and 7.59% [1]. The energy calibration of the tandem accelerator was performed using  $^{15}\text{N}+\text{H}$  resonance reaction. The acceleration voltage of the accelerator was changed at 1 keV step from 6.37 to 6.40 MV, and hydrogen of the water molecule which adsorbed to Ti surface was measured. Measuring time of one energy point was about 8 minutes, including the change time of beam energy. The obtained NRA data is shown in Fig. 1. The indication energy of the accelerator was 3 keV (0.05%) higher than the resonance energy of 6.385 MeV. The FWHM of resonance peak was 12 keV. The doppler effect by vibration of a hydrogen atom causes an energy spread of about 10 keV.

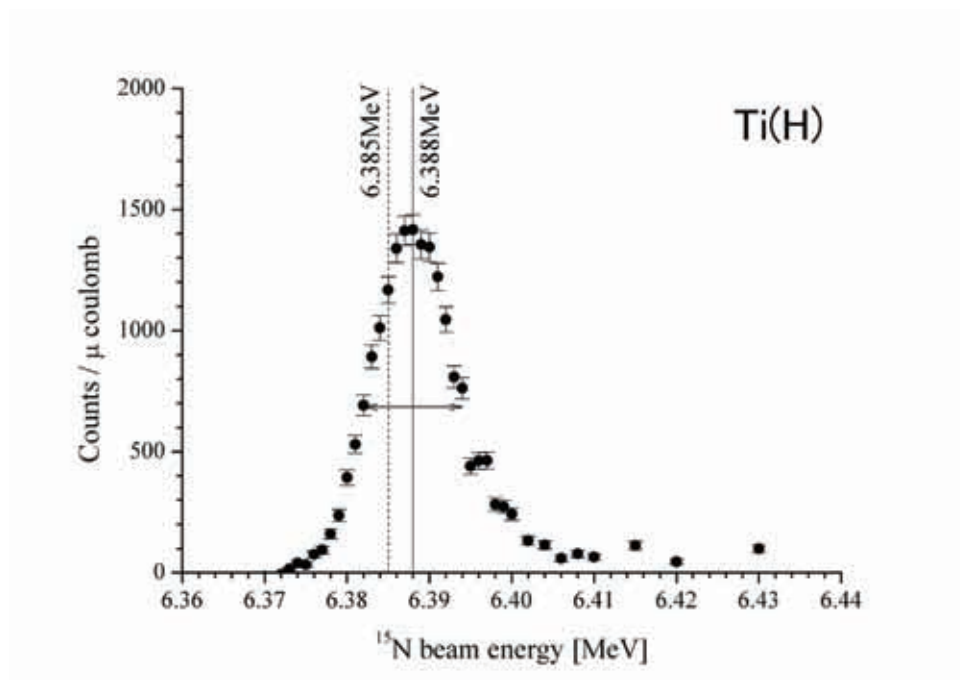


Fig. 1  $^{15}\text{N}$  nuclear reaction profile data for Ti sample.

<sup>1</sup> Japan Atomic Energy Agency (JAEA)

The measurement result of an aluminized polyester film is shown in Fig. 2. Hydrogen of the water adsorbed on the surface and hydrogen inside polyester were observed. The thickness of aluminum was estimated from the width of an area of low gamma ray yield near 6.41 MeV. The estimated thickness was about 43 nm. The result of the thickness measurement by the RBS method was 40 nm, and obtained the almost same result.

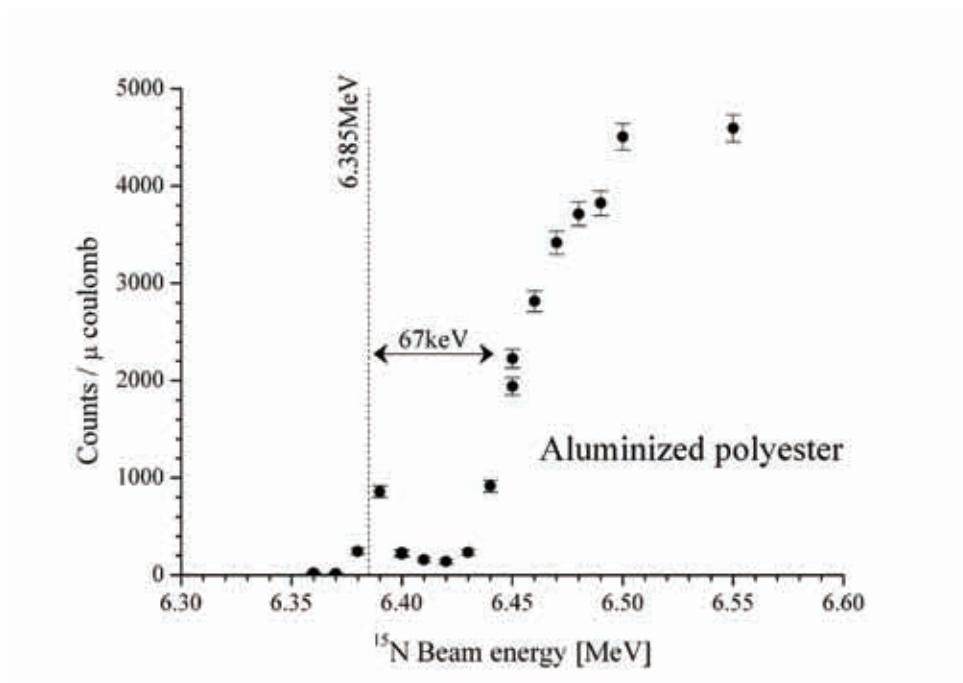


Fig. 2 The raw data for a hydrogen profile of an aluminized polyester film.

The polyimide film was irradiated with  $^{15}\text{N}$  of the energy of 6.5 MeV for the quantification test of hydrogen concentration. The yields of the gamma ray estimated by assuming the resonance width of a reaction to be 10 keV were about 30% of simulation results. It is better to use a standard specimen for quantification of hydrogen concentration.

## References

- [1] H. Makii, private communication.
- [2] M. Matsuda et al., JAEA-Tokai Tandem Annu. Rep. 2010, JAEA-Review 2011-040(2011)9

## **CHAPTER 2**

### **Nuclear Structure**

#### **2.1 Coulomb Excitation Experiment of $^{128,130}\text{Xe}$**

This is a blank page.

## 2.1 Coulomb Excitation Experiment of $^{128,130}\text{Xe}$

M. Koizumi<sup>1</sup>, Y. Toh<sup>1</sup>, M. Oshima<sup>1</sup>, A. Kimura<sup>1</sup>, Y. Hatsukawa<sup>1</sup>, K. Furutaka<sup>1</sup>, H. Harada<sup>1</sup>, F. Kitatani<sup>1</sup>,  
S. Nakamura<sup>1</sup>, M. Sugawara<sup>2</sup> and E. Ideguchi<sup>3</sup>

Stable Xe isotopes gradually change their properties from a  $\gamma$ -unstable character ( $A \sim 124$ ) to a vibrational one ( $A = 134$ ) [1]. The change is considered as a shape phase transition from O(6) to U(5) symmetry, in terms of dynamic symmetry of the IBM. Theoretical calculations suggested that the E(5) critical point of the shape phase transition would appear at around  $A = 130$  in Xe isotopes [2,3]. Information on electromagnetic properties of those nuclei, such as B(E2) values and quadrupole moments, is required to understand the change of the nuclear properties. As for  $^{130}\text{Xe}$ , which is considered to be a  $\gamma$ -unstable nuclei, no B(E2) of the ground and  $2_2^+$  band has been measured except for B(E2:  $2_1^+ \rightarrow 0_1^+$ ). Quadrupole moments of low-lying states of  $^{128,130}\text{Xe}$  have not been measured yet.

Coulomb excitation is a useful method for measurements of B(E2)s and quadrupole moments near the ground states of nuclei [4,5]. Our systematic study of stable nuclei with  $A \sim 70$  revealed nuclear properties and their changes [6-13]. To obtain electromagnetic properties of  $^{126-136}\text{Xe}$  isotopes, we have started Coulomb excitation experiments.

Coulomb excitation experiments of  $^{208}\text{Pb}(^{128}\text{Xe}, \gamma)$  and  $^{208}\text{Pb}(^{130}\text{Xe}, \gamma)$  were carried out with 550-MeV  $^{130}\text{Xe}$  and 548-MeV  $^{128}\text{Xe}$  beams; both beam energies are below each of the Coulomb barrier. The beam

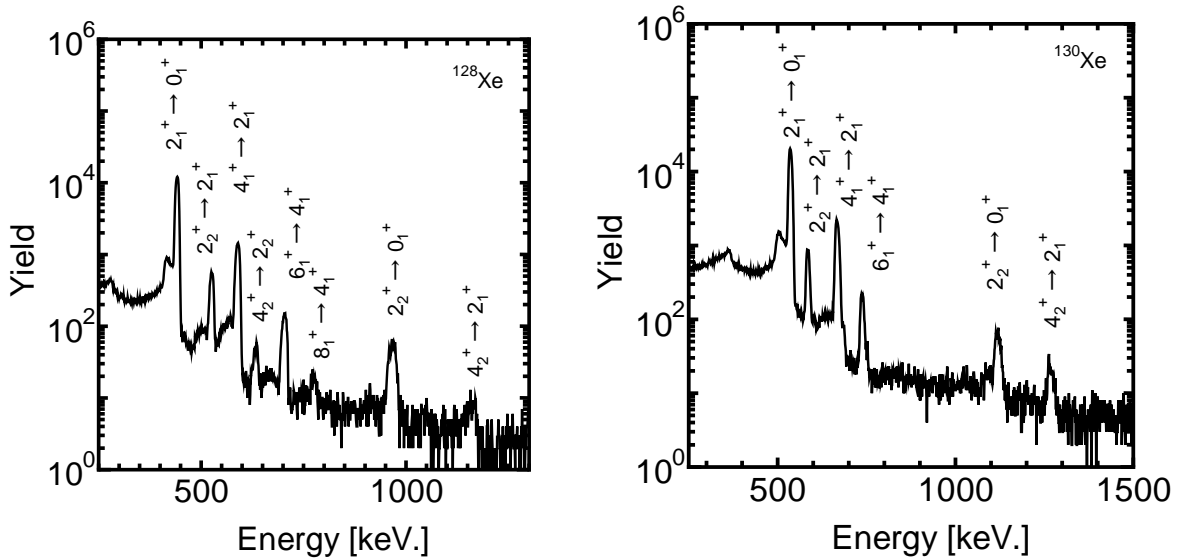


Fig. 1. Doppler-corrected spectra obtained in the  $^{208}\text{Pb}(^{128}\text{Xe}, \gamma)$  and  $^{208}\text{Pb}(^{130}\text{Xe}, \gamma)$  experiments.

<sup>1</sup> Japan Atomic Energy Agency (JAEA)

<sup>2</sup> Chiba Institute of Technology

<sup>3</sup> CNS, the University of Tokyo

currents of  $^{128}\text{Xe}$  and  $^{130}\text{Xe}$  beams were approximately 0.03 pA and 0.5 pA, respectively. The low beam current of  $^{128}\text{Xe}$  was probably due to the low pressure of the Xe gas supply of the terminal ion source. The target thicknesses of  $^{208}\text{Pb}$  foils were approximately  $0.9\text{ }\mu\text{m}$  ( $1\text{ mg/cm}^2$ ). A  $\gamma$ -ray detector array, GEMINI-II [14,15], and a position sensitive particle detector array, LUNA [16], were used to measure de-excitation  $\gamma$  rays and scattering angles of the incident particles, respectively. Approximately,  $0.6 \times 10^6$  and  $1.9 \times 10^7$  particle- $\gamma$  coincidence events were obtained in the  $^{208}\text{Pb}(^{128}\text{Xe}, \gamma)$  and  $^{208}\text{Pb}(^{130}\text{Xe}, \gamma)$  experiments.

The position data of LUNA were used for the corrections of Doppler shift of observed  $\gamma$ -ray energies. Figure 1 shows Doppler-corrected  $\gamma$  spectra, for example.  $^{128}\text{Xe}$  was excited up to the  $8_1^+$  and the  $4_2^+$  state, the excitation energy of which is 2512 keV and 1603 keV, respectively. Totally, eight de-excitation  $\gamma$  rays were observed in the experiment. As for  $^{130}\text{Xe}$ , the nucleus was excited up to the  $6_1^+$  and the  $4_2^+$  state, the excitation energy of which is 1944 keV and 1880 keV. Six de-excitation  $\gamma$  rays were observed.

Coulomb excitation probabilities are determined by experimental conditions: such as interacting particles, incident energy, scattering angles, and electro-magnetic transition probabilities of the nuclei of interest. Yields of observed  $\gamma$  rays, therefore, change as the scattering angle varies. By fitting the observed  $\gamma$ -ray yields for each scattering angle, B(E2) values and quadrupole moments are deduced. The analysis of the experiments with a  $\chi^2$  minimum search code, GOSIA, is in progress.

## References

- [1] R.F. Casten and P.V. Brentano, Phys. Lett. 152 (1985) 22.
- [2] D.L. Zhang and Y.X. Liu, Chin. Phys. Lett. 20 (2003) 1028-1030.
- [3] R. Fossin, D. Bonatsos and G.A. Lalazissis, Phys. Rev. C 73 (2006) 044310.
- [4] K. Alder and A. Winther, Coulomb Excitation (Academic, New York, 1966).
- [5] K. Alder and A. Winther, Electromagnetic Excitation (North Holland, Amsterdam, 1975).
- [6] Y. Toh et al., J. Phys. G 27 (2001) 1475-1480.
- [7] Y. Toh et al., Eur. Phys. J. A 9 (2000) 353-356.
- [8] A. Osa et al., Phys. Lett. B 546 (2002) 48-54.
- [9] M. Zielinska et al., Nucl. Phys. A 712 (2002) 3-13.
- [10] M. Koizumi et al., Eur. Phys. J. A 18 (2003) 87-92.
- [11] M. Sugawara et al., Eur. Phys. J. A 16 (2003) 409-414.
- [12] M. Koizumi et al., Nucl. Phys. A 736 (2003) 46-58.
- [13] T. Hayakawa et al., Phys. Rev. C 67 (2003) 064310.
- [14] K. Furuno et al., Nucl. Instrum. Methods Phys. Res. A 421 (1999) 211; M. Oshima et al., J. Radioanal. Nucl. Chem. 278 (2008) 257-262.
- [15] M. Oshima et al., J. Radioanal. Nucl. Chem., 278 (2008) 257-262.
- [16] Y. Toh et al., Rev. Sci. Instr. 73 (2002) 47-50.



## CHAPTER 3

### Nuclear Reaction

- 3.1 Fission of proton-rich mercury nuclei populated by fusion reaction
- 3.2 Measurement of fission cross section for  $^{239}\text{U}(\text{n},\text{f})$  using surrogate reaction method
- 3.3 Surrogate ratio method for determination of  $(\text{n},\gamma)$  cross sections
- 3.4 Measurement of grazing angles of  $^{136}\text{Xe}+^{198}\text{Pt}$   
at energy region around Coulomb barrier
- 3.5 Fission fragment anisotropy in heavy-ion-induced fission of actinide nuclei
- 3.6 Measurement of branching ratio of  $^{22}\text{Ne}(\alpha, \gamma) ^{26}\text{Mg}$  /  $^{22}\text{Ne}(\alpha, \text{n}) ^{25}\text{Mg}$  reactions

This is a blank page.

### 3.1 Fission of proton-rich mercury nuclei populated by fusion reaction

A. Andreyev<sup>1</sup>, K. Nishio<sup>2</sup>, J. Benlliure<sup>3</sup>, M. Caamano<sup>3</sup>, X. Derkx<sup>1</sup>, L. Guys<sup>4</sup>, F. Heßberger<sup>5</sup>, B. Kindler<sup>5</sup>, J. Lane<sup>1</sup>, V. Liberati<sup>1</sup>, B. Lommel<sup>5</sup>, H. Makii<sup>2</sup>, S. Mitsuoka<sup>2</sup>, T. Nagayama<sup>2,6</sup>, I. Nishinaka<sup>2</sup>, S. Ohta<sup>2</sup>, T. Ohtsuki<sup>7</sup>, K. Sandhu<sup>1</sup>, P. Van Dupen<sup>4</sup>, M. Veselsky<sup>8</sup> and Y. Wakabayashi<sup>2</sup>

Our collaborative program started from the study of low-energy fission of proton-rich nucleus  $^{180}\text{Hg}$  [1]. The fission of  $^{180}\text{Hg}$  was studied by populating its excited states by the  $\beta^+/\text{EC}$  decay of the parent nucleus  $^{180}\text{Tl}$ . The excitation energy of  $^{180}\text{Hg}$  is less than 10 MeV from the constrain of the Q-value, thus the shell effects are preserved. We measured the fission fragment mass distributions for  $^{180}\text{Hg}$  at the ISOLDE mass separator at CERN (Geneva). Based on the typical understanding of the fission process from the typical actinide fissions of the  $N/Z \approx 1.5\text{--}1.6$  nuclei, the  $^{180}\text{Hg}$  should split into two equal fragments  $^{90}\text{Zr} + ^{90}\text{Zr}$ , since the zirconium-90 has the closed neutron shell of  $N=50$ . The result was, however, unexpected. Mercury-180 splits dominantly into fission fragments around  $^{80}\text{Kr}$  and  $^{100}\text{Ru}$  and shows asymmetric mass distribution. The results imply that there is a new region of asymmetric fission in the proton-rich nuclei.

At the JAEA tandem facility, we also performed fission studies at relatively higher excitation energies populated by heavy-ion induced fusion reactions. Advantage of this approach is that by choosing different combinations of projectile and target nucleus, wider variety of fissioning nuclei can be populated, allowing us to study systematic behavior of fission properties along the Chart of Nuclei. Moreover, by changing the beam energy, we can study the excitation energy dependence of the fission fragment mass distribution, and thus the transition from the low-energy fission influenced by the shell effects to the higher-energy fission dominated by the liquid-drop behavior would be studied. We have carried out the fusion-fission experiments in the reactions of  $^{36,40}\text{Ar} + ^{144,154}\text{Sm} \rightarrow ^{180,184,190,194}\text{Hg}^*$  at the bombarding energies corresponding to the excitation energies of  $E^* = 35\text{--}100$  MeV. In this report, mass and total kinetic energy (TKE) distributions for  $^{180}\text{Hg}$  ( $E^* = 34$  MeV) and  $^{190}\text{Hg}$  ( $E^* = 50$  MeV) will be shown.

Experiment was carried out using Ar beams supplied by the tandem accelerator. The thin target foils were made by evaporating the samarium fluoride materials and condensating it on a thin carbon foil ( $36\text{ }\mu\text{g}/\text{cm}^2$ ) with a thickness  $\sim 70\text{ }\mu\text{g}/\text{cm}^2$ . Enrichment for  $^{144}\text{Sm}$  and  $^{154}\text{Sm}$  targets are 93.8 % and 98.9 %, respectively. The targets were made at the target laboratory of GSI, Darmstadt. Fission fragments are detected by using a position-sensitive multi-wire proportional counter (MWPC) with active area of  $200\text{mm(H)} \times 120\text{mm(V)}$  [2]. Two MWPCs were mounted at  $71^\circ$  relative to the beam direction, and the distance

<sup>1</sup> University of the West of Scotland

<sup>2</sup> Japan Atomic Energy Agency (JAEA)

<sup>3</sup> University de Santiago de Compostela

<sup>4</sup> IKS, KU Leuven

<sup>5</sup> GSI Helmholtzzentrum

<sup>6</sup> Ibaraki University

<sup>7</sup> Tohoku University

<sup>8</sup> Slovak Academy of Science

from the target to the center of the MWPC was set 211 mm.

Figure 1 shows the results of mass and *TKE* distributions for the fissions of  $^{180}\text{Hg}^*$  ( $E^*=34\text{MeV}$ ) and  $^{190}\text{Hg}^*$  ( $E^*=57\text{MeV}$ ), produced by the reactions of  $^{36}\text{Ar}+^{144}\text{Sm}$  ( $E_{\text{c.m.}}=126\text{MeV}$ ) and  $^{36}\text{Ar}+^{154}\text{Sm}$  ( $E_{\text{c.m.}}=128\text{MeV}$ ), respectively. The mass distributions are well reproduced by asymmetric fission centered at  $A_L/A_H = 79/101$  and  $82/108$  for  $^{180}\text{Hg}^*$  and  $^{190}\text{Hg}^*$ , respectively, where  $A_L$  and  $A_H$  stand for the light and heavy fragment mass. The fission of  $^{180}\text{Hg}^*$  gives almost the same mass asymmetry as observed in the  $\beta^+/\text{EC}$ -delayed fission of  $^{180}\text{Tl}$  ( $A_L/A_H = 80/100$ ), meaning that the mass asymmetry does not change at the higher excitation energy. The fusion-fission data can be used to study the island (or peninsula) for the asymmetric fission in the proton rich nuclei. As the bombarding energies for the two reactions are nearly the same, the angular momentum brought to the systems of  $^{180}\text{Hg}^*$  and  $^{190}\text{Hg}^*$  (in other words - the rotational energy of the fissioning systems) is nearly the same. The additional 23 MeV excitation energy to the compound nucleus does not wash out the effects of the shells in the fission process. The phenomenon forms contrast to the fission of typical actinide nuclei of around  $N/Z=1.5 - 1.6$ , where the mass asymmetry in low energy changes to symmetry with excitation energy.

In the fission of  $^{180}\text{Hg}^*$ , the average *TKE* is 131.7MeV. The value is nearly the same as the  $\beta^+/\text{EC}$ -delayed fission of  $^{180}\text{Tl}$  (134MeV) [1]. The standard deviation of 11.7 MeV for the *TKE* distribution is larger than that for the  $\beta^+/\text{EC}$ -delayed fission (5.6 MeV) [1]. The *TKE* is nearly equal to the Coulomb energy at the scission point. It means that the higher temperature of the fission system does not change the average distance between the charge centers at the instant of nuclear rupture, but the temperature changes fluctuation of the distance.

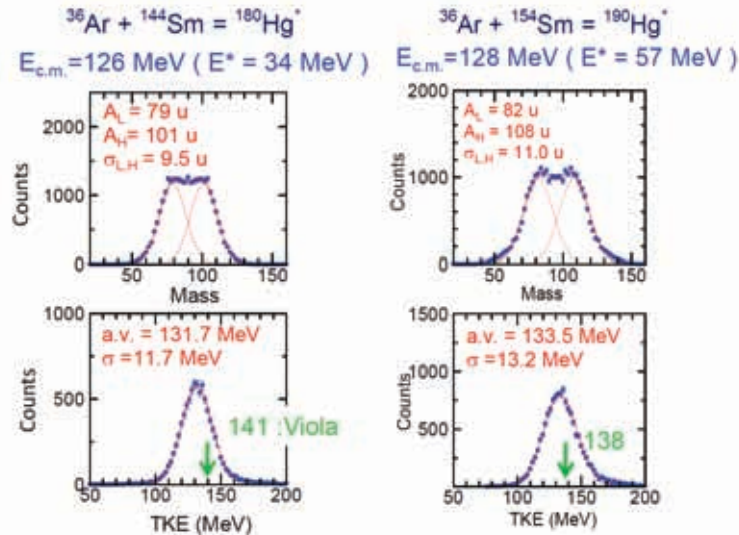


Fig. 1 Fission fragment mass and *TKE* distributions for the fusion-fission of  $^{46}\text{Ar}+^{144}\text{Sm}$  and  $^{46}\text{Ar}+^{154}\text{Sm}$ . The arrows in the *TKE* spectra are the values from the Viola formula [3].

## References

- [1] A. Andreyev et al., Phys. Rev. Lett., 105, 252102 (2010).
- [2] K. Nishio et al., Phys. Rev. C 77, 064607 (2008).
- [3] V.E. Viola, Jr., Nucl. Data, Sect. A 1, 391 (1966).

### 3.2 Measurement of fission cross section for $^{239}\text{U}(\text{n},\text{f})$ using surrogate reaction method

K. Nishio<sup>1</sup>, T. Nagayama<sup>1,2</sup>, I. Nishinaka<sup>1</sup>, S. Mitsuoka<sup>1</sup>, H. Makii<sup>1</sup>, Y. Wakabayashi<sup>1</sup>, S. Ohta<sup>1</sup>,  
K. Furutaka<sup>1</sup>, K. Tsukada<sup>1</sup>, M. Asai<sup>1</sup>, S. Chiba<sup>1,3</sup>, T. Ishii<sup>1</sup> and T. Ohtsuki<sup>4</sup>

Neutron-induced fission cross-sections are important for the design of nuclear reactors. The next generation nuclear reactor is designed to have a high neutron energy spectrum to make an efficient production of burnable isotopes and to transmute long-lived minor actinides. To simulate the criticality and the power response of such reactors, nuclear data for short-lived minor actinides as well as long-lived ones are needed. Some of the data is practically impossible to obtain using a neutron source. To obtain these data, so called ‘surrogate reaction method’ is proposed [1,2]. In this approach, a compound nucleus same as the one produced by neutron capture is populated by heavy-ion induced nucleon-transfer reactions and the decay probability to fission is determined. We have carried out an experiment to obtain the fission cross sections for  $^{239}\text{U}(\text{n},\text{f})$  (the half-life of  $^{239}\text{U}$  is 23 min),  $\sigma_{\text{U}239(\text{n},\text{f})}$ , with the surrogate ratio method, where the cross sections were obtained by referring the well known cross sections for  $^{235}\text{U}(\text{n},\text{f})$ ,  $\sigma_{\text{U}235(\text{n},\text{f})}$ . We have chosen the transfer-reaction  $^{238}\text{U}(^{18}\text{O}, ^{16}\text{O})^{240}\text{U}^*$  as the surrogate of  $\text{n}+^{239}\text{U}$ , and the fission probability of  $^{240}\text{U}^*$ ,  $P_{\text{U}240^*}$ , has been determined. Similarly, the reaction  $^{235}\text{U}(^{18}\text{O}, ^{17}\text{O})^{236}\text{U}^*$  was used as a surrogate of  $\text{n}+^{235}\text{U}$  to determine the fission probability  $P_{\text{U}236^*}$ . Thus, we obtained the cross sections for  $^{239}\text{U}(\text{n},\text{f})$  as,

$$\sigma_{\text{U}239(\text{n},\text{f})} = \sigma_{\text{U}235(\text{n},\text{f})} (P_{\text{U}240^*} / P_{\text{U}236^*}). \quad (1)$$

The experiment was carried out using an  $^{18}\text{O}$  beam (162MeV) supplied by the tandem accelerator. The uranium targets ( $^{235}\text{U}$  and  $^{238}\text{U}$ ) were made by electrically depositing natural or enriched uranium materials on thin nickel foils. Projectile-like nuclei produced by the transfer reaction were identified by silicon  $\Delta\text{E}$ -E detectors mounted on the forward angle from the target to cover the angles from  $22^\circ$  to  $38^\circ$  with respect to the beam direction. The  $\Delta\text{E}$  detector has a 75  $\mu\text{m}$  thickness and is made by an ion implantation technique. An annular type Si-strip detector was used for the E detector to measure the residual energy. Oxygen isotopes of  $^{16,17,18}\text{O}$  were clearly separated on the  $\Delta\text{E}$ -E spectrum, and the particle energy was determined with the resolution of about 0.9 MeV (FWHM). Fission fragments are detected using position-sensitive multi-wire proportional counters (MWPCs) with active area of 200 mm(H)×400 mm(V). The design for the MWPC is based on the one in [3], but the active area was 3.3 times larger. Four MWPCs were mounted at a distance 200 mm from the target. Fission probability at an excitation energy,  $E^*$ , was determined by the number of coincidence events between fission fragments and projectile-like nucleus for the specific transfer channel normalized by the singles events for the projectile-like nucleus. The reference data of  $\sigma_{\text{U}235(\text{n},\text{f})}$  was taken from ENDF/B-VII.

Figure 1 shows the preliminary result of the fission cross sections for  $^{239}\text{U}(\text{n},\text{f})$ . In the spectrum, structures

<sup>1</sup> Japan Atomic Energy Agency (JAEA)

<sup>2</sup> Ibaraki University

<sup>3</sup> Tokyo Institute of Technology

<sup>4</sup> Tohoku University

associated with the first and second chance fissions are seen at the neutron energies of  $E_n = 6.5$  MeV and 13.5 MeV. In the surrogate ratio method using the reactions of  $^{18}\text{O} + ^{235,238}\text{U}$ , different transfer channels and reference data can be used to obtain the same cross sections of  $^{239}\text{U}(n,f)$ . Such an attempt is in progress.

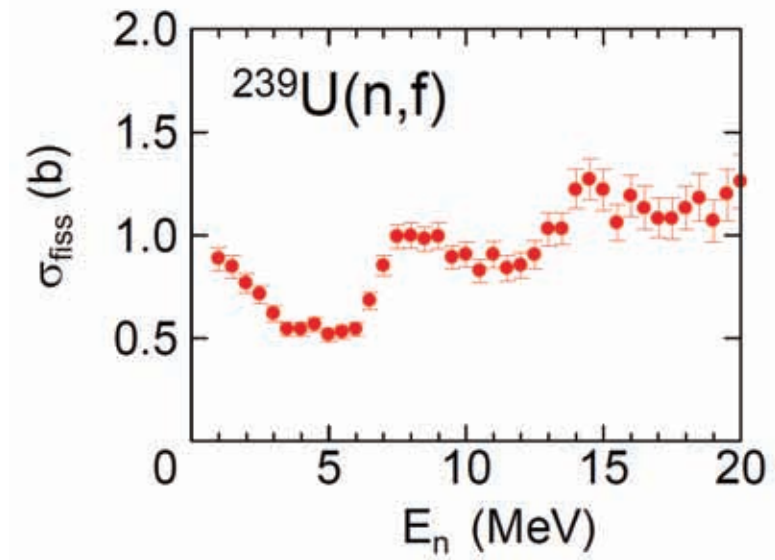


Fig. 1 Neutron-induced fission cross sections for  $^{239}\text{U}$  determined by the surrogate ratio method. The cross sections are plotted as a function of neutron energy.

## References

- [1] J.E. Escher et al., Rev. Mod. Phys. 84, (2012) 353-397.
- [2] S. Chiba et al., Phys. Rev. C 81, (2010) 044604.
- [3] K. Nishio et al., Phys. Rev. C 77, (2008) 064607.

### 3.3 Surrogate ratio method for determination of (n, $\gamma$ ) cross sections

H. Makii<sup>1</sup>, T. Ishii<sup>1</sup>, S. Ota<sup>1</sup>, Y. Wakabayashi<sup>2</sup>, M. Asai<sup>1</sup>, K. Furutaka<sup>1</sup>, K. Nishio<sup>1</sup>, S. Mitsuoka<sup>1</sup>,  
I. Nishinaka<sup>1</sup> and S. Chiba<sup>3</sup>

Neutron-capture [(n, $\gamma$ )] cross sections of unstable nuclei play an important role in the stellar nucleosynthesis [1]. However, measurements of the (n, $\gamma$ ) cross sections of unstable nuclei at the stellar temperature range ( $kT \approx 8 \sim 90$  keV) are very difficult. The main difficulties are due to a sample preparation and/or radioactivity of the sample. These difficulties can be overcome with the surrogate method, which aims at determining reaction cross sections for compound-nuclear reaction on the basis of the assumption that the formation and decay of a compound nucleus are independent of each other [2]. However, the decay branching ratio of the (n, $\gamma$ ) process is sensitive to the spin and parity values of the decaying compound nuclei [2], and they are probably different between the neutron-induced reaction and the surrogate reaction. Recently, Chiba and Iwamoto found that the difference of the spin and parity distributions between the neutron-induced and the surrogate reaction can be compensated if the surrogate ratio method (SRM) [3] is applied. The SRM can yield neutron cross sections with reasonable accuracies if (1) the weak Weisskopf-Ewing condition defined in ref. [3] is satisfied, (2) the spin and parity distributions in two compound nuclei populated by two surrogate reactions used in the SRM are equivalent, and (3) the maximum spin populated by the surrogate reactions is not too large (less than 10 hbar). Although these conditions have been verified theoretically [3-5], the feasibility of the SRM has not been demonstrated experimentally for determination of (n, $\gamma$ ) cross sections. Hence, we have prepared experimental apparatus for the SRM to determine (n, $\gamma$ ) cross sections and measured deexcitation  $\gamma$ -rays in compound nuclei produced by the multinucleon transfer reactions, such as ( $^{18}\text{O}$ ,  $^{16}\text{O}$ ) reaction, using a  $0.9 \text{ mg/cm}^2$   $^{155}\text{Gd}$  target deposited on  $1.1 \text{ }\mu\text{m}$  aluminum foils and  $153 \text{ MeV}$   $^{18}\text{O}$  beam.

In this study, we used two anti-Compton  $\text{LaBr}_3(\text{Ce})$  spectrometers to measure  $\gamma$ -rays from the populated compound nuclei, and a Si  $\Delta E$ - $E$  detector to detect outgoing particles from multinucleon transfer reactions. The anti-Compton  $\text{LaBr}_3(\text{Ce})$  spectrometer consists of a central  $\text{LaBr}_3(\text{Ce})$  detector with a diameter of  $101.6 \text{ mm}$  and a length of  $127 \text{ mm}$ , and an annular BGO detector with a thickness of  $25.4 \text{ mm}$  and a length of  $254 \text{ mm}$ . For the Si  $\Delta E$ - $E$  detector, we used four surface-barrier type Si detectors with a thickness of  $65 \text{ }\mu\text{m}$  and a diameter of  $20 \text{ mm}$ , and an annular Si detector with an inside diameter of  $48 \text{ mm}$ , an outside diameter of  $96 \text{ mm}$ , and a thickness of  $300 \text{ }\mu\text{m}$  as the  $\Delta E$  and  $E$  detector, respectively.

Figure 1 shows an  $E$ - $\Delta E$  plot for outgoing particles measured by the Si  $\Delta E$ - $E$  detector. The particles are clearly separated according to the mass number as well as the atomic number; various isotopes of O, F, N, and C were observed, which correspond to the populations of series of Gd, Eu, Tb, and Dy isotopes as compound nuclei. This demonstrates that the surrogate method using multinucleon transfer reactions with

<sup>1</sup> Japan Atomic Energy Agency (JAEA)

<sup>2</sup> RIKEN

<sup>3</sup> Tokyo Institute of Technology

heavy-ion projectiles has an advantage to obtain experimental data corresponding to a wide variety of reactions in one experimental setup.

Figure 2 shows deexcitation  $\gamma$ -rays in  $^{157}\text{Gd}$  obtained by setting a gate on  $^{16}\text{O}$  particles with the kinetic energies corresponding to the excitation energies of  $^{157}\text{Gd}$  between 3 and 14 MeV. Continuum  $\gamma$  rays up to about 8 MeV are due to deexcitation of highly excited state in  $^{157}\text{Gd}$  populated by the ( $^{18}\text{O}$ ,  $^{16}\text{O}$ ) reaction. The decay branching ratio of the (n, $\gamma$ ) process at the excitation energy  $E_x$  can be determined from the ratio of the number of  $\gamma$ -rays in coincidence with  $^{16}\text{O}$  particles  $N_{\text{O-}\gamma}(E_x)$  to the number of  $^{16}\text{O}$  particles  $N_{\text{O}}(E_x)$ . The  $N_{\text{O-}\gamma}(E_x)$  can be obtained from the  $\gamma$ -ray spectrum in coincidence with  $^{16}\text{O}$  particles by using the weighting function technique [6], which requires complete knowledge of the response functions for the  $\text{LaBr}_3(\text{Ce})$  spectrometers for a broad range of  $\gamma$ -ray energies. These have been determined experimentally using standard  $\gamma$ -ray sources of  $^{60}\text{Co}$  and  $^{88}\text{Y}$ , and  $\gamma$  rays from  $^{27}\text{Al}(\text{p},\gamma)^{28}\text{Si}$  measured at  $E_p = 0.992$  and 2.046 MeV, as is the case of the  $\text{NaI}(\text{Tl})$  spectrometer [7]. For unmeasured  $\gamma$ -ray energies, the response functions of the  $\text{LaBr}_3(\text{Ce})$  spectrometers are deduced by the Monte-Carlo code, GEANT4 [8]. This work remains to be done.

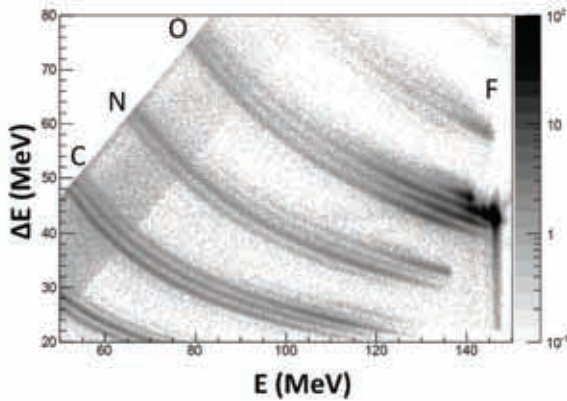


Fig. 1  $E$ - $\Delta E$  plot of scattered particles measured by Si  $\Delta E$ - $E$  detector in the reaction of 153-MeV  $^{18}\text{O}$  beam with  $^{155}\text{Gd}$  target.

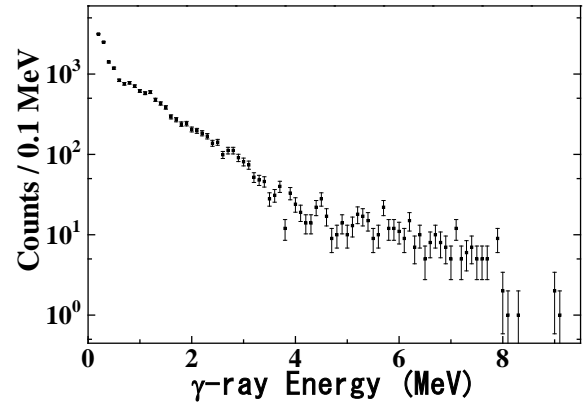


Fig. 2  $\gamma$ -ray spectrum in coincidence with  $^{16}\text{O}$  particles with kinetic energies corresponding to the excitation energies of  $^{157}\text{Gd}$  between 3 and 14 MeV.

## References

- [1] F. Käppeler and A. Mengoni, Nucl. Phys. A777 (2006) 291-310.
- [2] J.E. Escher et al., Rev. Mod. Phys. 84 (2012) 353-397.
- [3] S. Chiba and O. Iwamoto, Phys. Rev. C81 (2010) 044604-1-6.
- [4] Y. Aritomo, S. Chiba and K. Nishio, Phys. Rev. C84 (2011) 024602-1-10.
- [5] K. Ogata, S. Hashimoto and S. Chiba, J. Nucl. Sci. Technol. 48 (2011) 1337-1342.
- [6] R.L. Macklin and J.H. Gibbons, Phys. Rev. 159 (1967) 1007-1012.
- [7] H. Makii et al., Nucl. Instrum. Methods Phys. Res., A547 (2005) 411-423.
- [8] S. Agostinelli et al., Nucl. Instrum. Methods Phys. Res., A506 (2003) 250-303.



### 3.4 Measurement of grazing angles of $^{136}\text{Xe}+^{198}\text{Pt}$ at energy region around Coulomb barrier

Y.X. Watanabe<sup>1</sup>, H. Miyatake<sup>1</sup>, S.C. Jeong<sup>1</sup>, H. Ishiyama<sup>1</sup>, Y. Hirayama<sup>1</sup>,  
S. Mitsuoka<sup>2</sup>, K. Nishio<sup>2</sup>, Y. Wakabayashi<sup>2</sup>, H. Makii<sup>2</sup> and I. Nishinaka<sup>2</sup>

We are now carrying a project to measure lifetimes of neutron-rich nuclei around a neutron magic number of 126 [1], which are considered to be progenitors of a peak around mass number of 195 in the abundance of nuclides, produced by the rapid neutron capture process (r-process) in the universe. The lifetimes of those nuclei are key parameters to determine astrophysical environment for the r-process. Although we will produce those neutron-rich nuclei by using multi-nucleon transfer (MNT) reactions of  $^{136}\text{Xe}+^{198}\text{Pt}$  in our project, mechanisms of those reactions are not fully understood to give adequate estimation of the production yields. To improve the estimation, we have performed an experiment by using the spectrometer VAMOS [2] at GANIL for determination of the cross sections of the MNT reactions. In performing the experiment, the angle of the spectrometer should have been carefully set for efficient collection of the reaction products, since the MNT reactions are considered to be prominent in the scattering around the grazing angle. Therefore, in advance, we have measured angular distributions of the elastic scattering including low-lying inelastic channels at angles around the grazing angle with several energies near the Coulomb barrier for the reaction system of  $^{136}\text{Xe}+^{198}\text{Pt}$  in the JAEA tandem facility.

The experimental setup is shown in Fig. 1. The  $^{198}\text{Pt}$  target with thickness of  $1.6\text{ mg/cm}^2$  was irradiated by the  $^{136}\text{Xe}$  beam accelerated to above the Coulomb barrier by the tandem accelerator and the super-conducting booster accelerator. Scattered particles were detected by two silicon telescopes located at 40 degrees and 60 degrees respect to the beam axis. The telescope consists of a slit with 10 mm vertical opening, a single-sided strip detector (SSSD) with 16 horizontal segments in the area of  $50\times 50\text{ mm}^2$ , and a solid state detector (SSD) with area of  $50\times 50\text{ mm}^2$  and thickness of  $325\text{ }\mu\text{m}$ . The distances between the target and the slit, the SSSD and the SSD are 129 (128) mm, 130.5 mm and 133.5 mm, respectively, subtending angles from 30 (50) degrees to 50 (70) degrees for the telescope at the angle of 40 (60) degrees. The thickness of the SSSD is  $20\text{ }\mu\text{m}$  and  $61\text{ }\mu\text{m}$  for the detector at the angle of 40 and 60 degrees, respectively. The measurements are performed at 5 points of energies in the laboratory system: 6, 6.5, 7, 7.5 and 8 MeV/A. At the highest three energies,

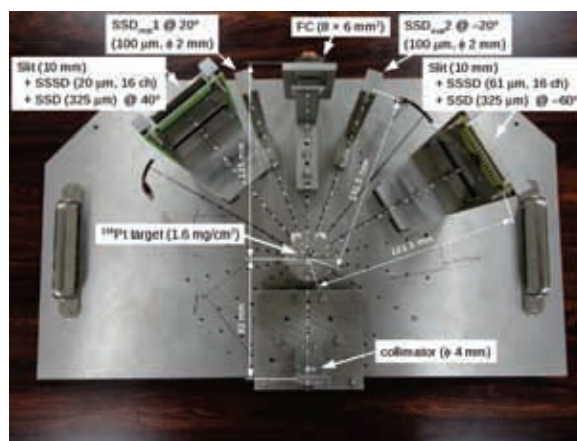


Fig. 1 Experimental setup.

The distances between the target and the slit, the SSSD and the SSD are 129 (128) mm, 130.5 mm and 133.5 mm, respectively, subtending angles from 30 (50) degrees to 50 (70) degrees for the telescope at the angle of 40 (60) degrees. The thickness of the SSSD is  $20\text{ }\mu\text{m}$  and  $61\text{ }\mu\text{m}$  for the detector at the angle of 40 and 60 degrees, respectively. The measurements are performed at 5 points of energies in the laboratory system: 6, 6.5, 7, 7.5 and 8 MeV/A. At the highest three energies,

<sup>1</sup> High Energy Accelerator Research Organization (KEK)

<sup>2</sup> Japan Atomic Energy Agency (JAEA)

measurements are also performed at the setup where the distance between the target and the telescope at the angle of 40 degrees is 60 mm shorter in order to cover a wider range of angles from 22 degrees to 58 degrees. For the normalization of the elastic scattering cross sections, two SSD's with thickness of 100  $\mu\text{m}$  are located at the angle of 20 degrees in both sides of the beam axis with collimators of 2 mm diameters at the distance of 131.5 mm from the target.

The scattered particles penetrate the SSSD and reach the SSD for the telescope at the angle of 40 degrees, although they stopped at the SSSD for the other. Fig. 2 shows correlation between the energy loss through the SSSD ( $\Delta E$ ) and the sum of energies deposited in the SSSD and the SSD for the telescope at the angle of 40 degrees by using the beam energy of 8 MeV/A. The one-dimensional energy spectrum is shown in Fig. 3. The elastic scattering events, including low-lying inelastic channels, are counted by fitting a peak at the higher energy with a Gaussian function and subtracting from it the contribution of damped collision fitted with a Gaussian function.

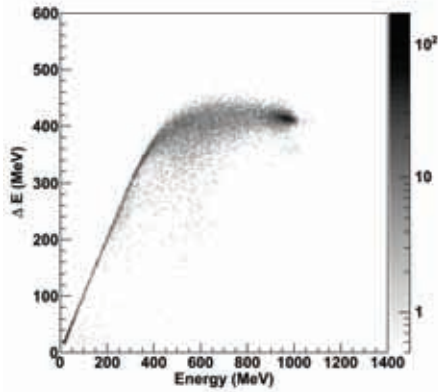


Fig. 2 Correlation between  $\Delta E$  and energy in one segment of SSSD at 40 degrees for beam energy of 8 MeV/A.

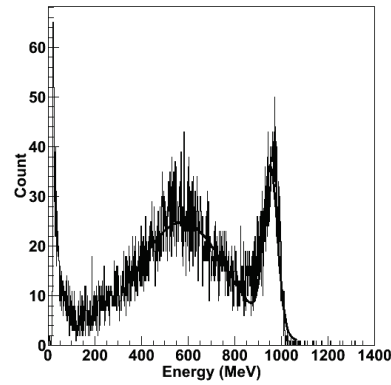


Fig. 3 Energy spectrum in one segment of SSSD at 40 degrees for beam energy of 8 MeV/A.

Fig. 4 shows the measured angular distributions of the elastic scattering normalized by the Rutherford scattering. At the energy of 8 MeV/A, the cross sections decrease steeply around the angle of 30 degrees, indicating that the contribution of MNT reactions are increasing around the angle and that it is proper to set the spectrometer there for the MNT reaction measurements with beam energy of 8 MeV/A.

## References

- [1] S.C. Jeong et al., KISS: KEK isotope separation system for  $\beta$ -decay spectroscopy, KEK Report 2010-2 (2010).
- [2] S. Pullanhiotan et al., Nucl. Instrum. Methods Phys. Res., A593 (2008) 343-352.

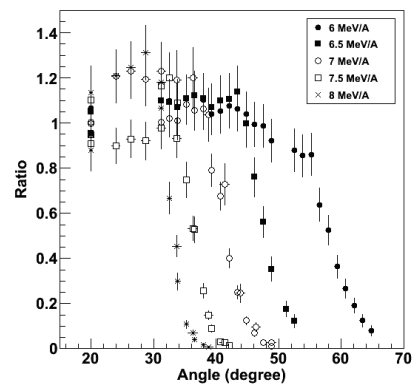


Fig. 4 Angular distributions of the elastic scattering normalized by the Rutherford scattering.

### 3.5 Fission fragment anisotropy in heavy-ion-induced fission of actinide nuclei

I. Nishinaka<sup>1</sup>, M. Tanikawa<sup>2</sup>, K. Nishio<sup>1</sup>, H. Makii<sup>1</sup>, S. Mitsuoka<sup>1</sup>, Y. Wakabayashi<sup>1</sup> and A. Yokoyama<sup>3</sup>

Fission fragment angular distribution in light-ion-induced fission is successfully explained by the standard saddle point model [1]. However, in heavy-ion-induced fission of actinides at near-barrier energies, it has been found that fission fragment anisotropy becomes anomalously high compared with that expected from the standard saddle point model [2, 3]. This anomaly of fission fragment anisotropy was thought to originate from non-equilibrium fission. The pre-equilibrium *K*-states model suggests that fission fragment anisotropy in heavy-ion-induced fission of actinides is governed by the entrance channel mass asymmetry  $\alpha = (A_t - A_p)/(A_t + A_p)$  [4, 5], where  $A_t$  and  $A_p$  refer to mass numbers of target and projectile nuclei, respectively. A limited number of experiments have been carried out to study the effect of different entrance channels leading to the same compound nucleus,  $^{248}\text{Cf}$  ( $^{16}\text{O} + ^{232}\text{Th}$  and  $^{12}\text{C} + ^{236}\text{U}$ ) [6] and  $^{246}\text{Bk}$  ( $^{14}\text{N} + ^{232}\text{Th}$  and  $^{11}\text{B} + ^{235}\text{U}$ ) [7]. In order to study the effect of fission fragment anisotropy on entrance channels we measured fission fragment angular distributions in the reactions of  $^{22}\text{Ne} + ^{232}\text{Th}$  ( $\alpha = 0.827$ ),  $^{16}\text{O} + ^{238}\text{U}$  ( $\alpha = 0.874$ ) and  $^{12}\text{C} + ^{242}\text{Pu}$  ( $\alpha = 0.906$ ) [8], populating the same compound nucleus  $^{254}\text{Fm}$ . As shown in Fig. 1, the anisotropy for  $^{22}\text{Ne} + ^{232}\text{Th}$  with the smallest entrance channel mass asymmetry  $\alpha = 0.827$  is larger than those for  $^{16}\text{O} + ^{238}\text{U}$  and  $^{12}\text{C} + ^{242}\text{Pu}$ . However, the uncertainty of the anisotropy is rather large especially for  $^{22}\text{Ne} + ^{232}\text{Th}$  because of the low statistics. In order to make quantitative understanding, it is important to obtain data with small uncertainty. Therefore, we have carried out the measurement for the  $^{22}\text{Ne} + ^{232}\text{Th}$  reaction to obtain more statistics. Analysis of data is still in progress.

#### References

- [1] R. Vandenbosch and J. R. Huizenga, Nuclear Fission (Academic, New York, 1973).
- [2] S. Kailas, J. Phys. G 23 (1997) 1227-1233.
- [3] J. P. Lestone et al., J. Phys. G 23 (1997) 1349-1357.
- [4] V. S. Ramamurthy et al., Phys. Rev. Lett. 65 (1990) 25-28
- [5] Z. Liu et al., Phys. Lett. B 353 (1995) 173-178
- [6] R. Vandenbosh et al., Phys. Rev. C 54 (1996) R977-R980.
- [7] B. R. Behera et al., Phys. Rev. C 69 (2004) 064603-1-10.
- [8] I. Nishinaka et al., JAEA-Review, 2010-056(2010)46-47;  
I. Nishinaka et al., JAEA-Review, 2011-040(2011)31-32.

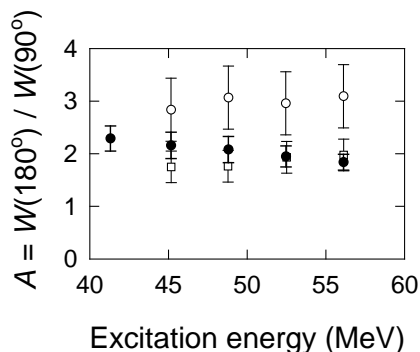


Fig. 1 Results of the fission fragment anisotropy for  $^{16}\text{O} + ^{238}\text{U}$  (solid circles),  $^{12}\text{C} + ^{242}\text{Pu}$  (open squares) and  $^{22}\text{Ne} + ^{232}\text{Th}$  (open circles) as a function of the excitation energy of the compound nucleus  $^{254}\text{Fm}$ .

<sup>1</sup> Japan Atomic Energy Agency (JAEA)

<sup>2</sup> The University of Tokyo

<sup>3</sup> Kanazawa University

### 3.6 Measurement of branching ratio of $^{22}\text{Ne}(\alpha, \gamma)^{26}\text{Mg}$ / $^{22}\text{Ne}(\alpha, n)^{25}\text{Mg}$ reactions

S. Ota<sup>1</sup>, H. Makii<sup>1</sup>, T. Ishii<sup>1</sup>, K. Nishio<sup>1</sup>, S. Mitsuoka<sup>1</sup>, I. Nishinaka<sup>1</sup> and S. Chiba<sup>1,2</sup>

About half of the elemental abundances between Fe and Bi have been thought to have their origins in s-process (slow neutron-capture) which proceeds during stellar He burning stage [1]. While the reaction  $^{22}\text{Ne}(\alpha, n)^{25}\text{Mg}$  is considered to be the dominant neutron source for the s-process in massive stars with  $M > 8 M_{\odot}$  (solar mass), the competing  $^{22}\text{Ne}(\alpha, \gamma)^{26}\text{Mg}$  reaction also may have considerable strength and significantly suppress the neutron production. A branching ratio of the two reactions and resonance states in  $\alpha + ^{22}\text{Ne}$  reaction at  $E_{\alpha} = 400 - 1000$  keV should be experimentally determined with good accuracy. Presently, ambiguity of the resonance state at  $E_x \sim 11.3$  MeV ( $E_{\alpha} \sim 830$  keV) such as level and strength has been one of the largest concerns for s-process study due to its expected significant role in the neutron production. In this work, we aimed to investigate the resonance.

Experiments were performed using 110 MeV  $^{22}\text{Ne}$  beam of JAEA-Tokai tandem accelerator.  $^6\text{Li} (^{22}\text{Ne}, ^{26}\text{Mg})$  d  $\alpha$ -transfer reaction has been employed since a direct  $\alpha$ -capture experiment is extremely difficult because of the high Coulomb barrier for low energy  $\alpha$ -particles. Some past experiments using  $^{22}\text{Ne} (^6\text{Li}, d)^{26}\text{Mg}$  reaction obtained important information about resonance spectrum of  $^{26}\text{Mg}$ , but insufficient energy resolution and background deuteron from compound nuclei reaction kept them from solving the 11.3 MeV resonance clearly enough [2, 3]. Therefore, we attempted to remove contribution from the background deuteron by coincidence detection of  $^{26}\text{Mg}$  and deuteron with high energy-resolution Si  $\Delta E$ -E detector.

$^6\text{Li}_2\text{CO}_3$  (95% enriched) target ( $\sim 20 \mu\text{g}/\text{cm}^2$ ) with C foil ( $20 \mu\text{g}/\text{cm}^2$ ) was exposed to the 10 pA  $^{22}\text{Ne}$  beam which was focused to 1 mm. Focusing the beam size was essentially important process to suppress the angular acceptance for deuteron which limits the energy resolution of spectrum. We had successively realized it with two Ta slits ( $\phi = 1$  and 1.5 mm, respectively) placed in front of the target. Each set of four  $\Delta E$ -E detectors was set at  $\theta = 3^\circ$  (for Mg) and  $-130^\circ$  (for d) with respect to beam direction (in laboratory frame) as shown in Fig. 1. This set up realizes the coincidence measurement of the reaction at  $\theta_{\text{cm}} = 25^\circ$ .

Fig. 2 shows the E- $\Delta E$  cross plot of observed particles with one of the detectors at  $\theta = -130^\circ$ . It enables us to easily identify deuteron from other particles and the energy resolution was measured to 65 keV ( $\Delta E + E$  total) from  $^{241}\text{Am}$   $\alpha$  source test performed just after the beam irradiation. Fig. 3 shows the E- $\Delta E$  cross plot of observed particles with one of the detectors at  $\theta = 3^\circ$ . Charge identification of the detected particles can be possible, but mass separation is unfortunately not enough. In the figure, the coincident events with the deuterons were plotted together. It is obvious that we succeeded in detecting the expected Mg-d coincident events. In next experiment, we are planning to improve the energy resolution of the detector systems and statistics to obtain the resonance information of  $E_x \sim 11.3$  MeV from the deuteron spectrum.

<sup>1</sup> Japan Atomic Energy Agency (JAEA)

<sup>2</sup> Tokyo Institute of Technology

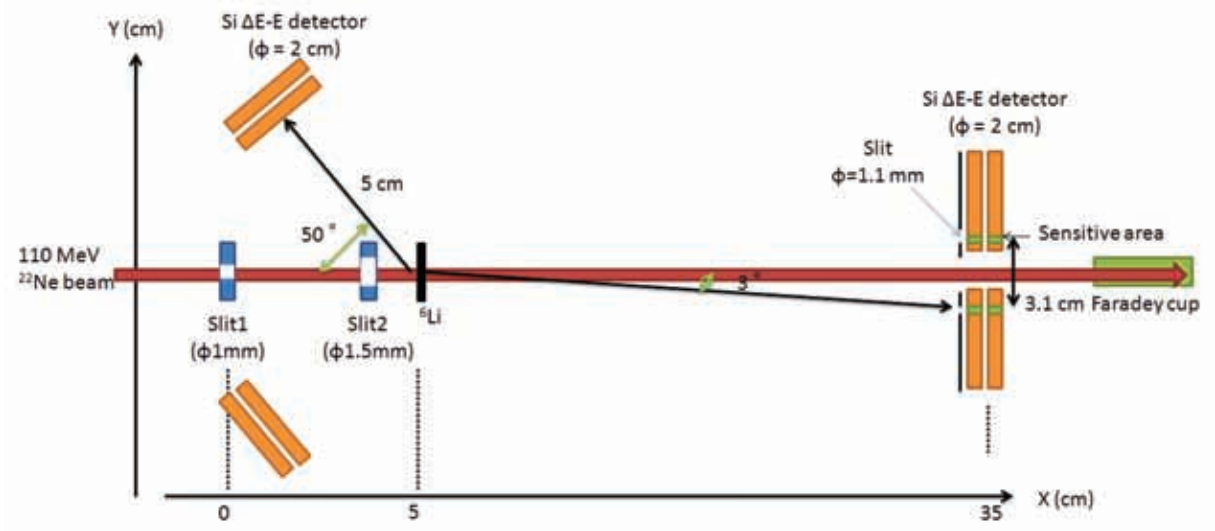


Fig. 1 Schematic view of the experimental set up.

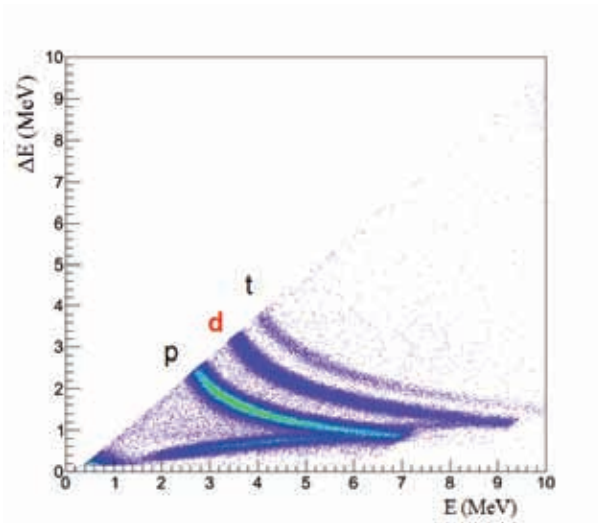


Fig. 2 E- $\Delta E$  cross plot of observed particles with one of the detectors at  $\theta = -130^\circ$ . Light green color shows high count rate.

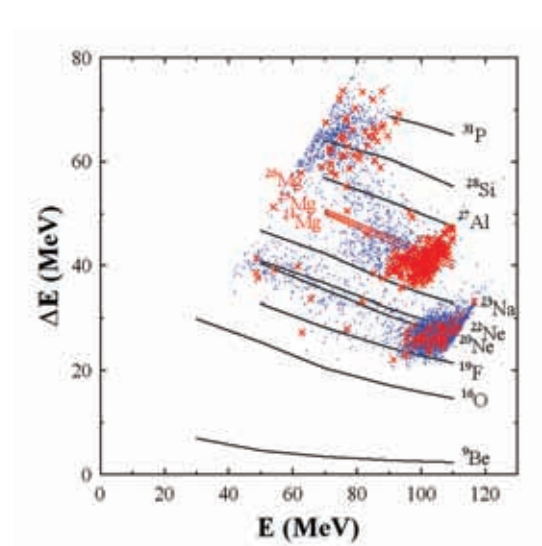


Fig. 3 E- $\Delta E$  cross plot of observed particles with one of the detectors at  $\theta = 3^\circ$  (dot). The coincident events with deuteron were plotted together (cross).

## References

- [1] F. Kappeler et al., Rev. Mod. Phys., 83 (2011) 157-193.
- [2] U. Giesen et al., Nuc. Phys., A 561 (1993) 95-111.
- [3] C. Ugalde et al., Phys. Rev., C 76 (2007) 025802-1-6.

This is a blank page.

## **CHAPTER 4**

### **Nuclear Chemistry**

- 4.1 First successful ionization of Lr applying an ISOL-technique  
with an improved surface-ionization type ion-source
- 4.2 Studies on isothermal chromatographic behavior  
of volatile compounds of Hf isotopes with various half-lives
- 4.3 Production and utilization of radioactive astatine isotopes using lithium ion beams
- 4.4 Production of medical radio isotope,  $^{95m}\text{Tc}$ . (II)
- 4.5 Measurement of radioisotopes on soil in Ibaraki prefecture

This is a blank page.



#### 4.1 First successful ionization of Lr applying an ISOL-technique with an improved surface-ionization type ion-source

N. Sato<sup>1</sup>, T.K. Sato<sup>1</sup>, M. Asai<sup>1</sup>, K. Tsukada<sup>1</sup>, A. Toyoshima<sup>1</sup>, K. Ooe<sup>1</sup>, Y. Kaneya<sup>1,2</sup>, Y. Nagame<sup>1</sup>,  
S. Ichikawa<sup>3</sup>, M. Schädel<sup>1</sup>, A. Osa<sup>1</sup>, T. Stora<sup>4</sup> and J.V. Kratz<sup>1,5</sup>

Study of the heaviest elements is an interesting and challenging subject in the field of nuclear chemistry. One of the most sensitive atomic properties to changes in the electronic structure is the first ionization potential (IP) which provides direct information on the stability of valence electrons in an atom. The ground-state electronic configuration of the last actinide, lawrencium (Lr) is predicted to be  $5f^{14}7s^27p$ . This is different from that of the lanthanide homolog Lu,  $4f^{14}6s^25d$  because the  $7p$  orbital of Lr is stabilized below the  $6d$  orbital by strong relativistic effects. The weakly-bound outermost electron results in a significantly low IP of Lr as compared with its neighboring heavy actinides [1]. Due to the low production rates and short half-lives, properties of the heaviest elements must be measured on an atom-at-a-time scale. To determine the IP of Lr based on the surface ionization efficiency measurement, we have improved our surface-ionization type ion-source [2]. In this study, using the ion-source system, we successfully measured the  $\alpha$ -particles from ionized and mass-separated  $^{256}\text{Lr}$ . To compare the ionization efficiency of Lr with Lu, the ionization of Lu was also performed at the same experimental condition.

Figure 1 shows a schematic view of the experimental setup including a photo of the improved ion-source. The  $^{256}\text{Lr}$  isotope (half-life,  $T_{1/2} = 27$  s) was produced in the  $^{249,250,251}\text{Cf}(^{11}\text{B}, \text{xn})$  reaction. The  $185 \mu\text{g}/\text{cm}^2$  thick Cf target of a 2.3 mm diameter was prepared by electrodeposition onto a  $1.85 \text{ mg}/\text{cm}^2$  Be backing foil. The isotopic composition of the Cf target was  $^{249}\text{Cf}$  (63%),  $^{250}\text{Cf}$  (12%) and,  $^{251}\text{Cf}$  (25%). The Dy target of a  $230 \mu\text{g}/\text{cm}^2$  thick was set downstream of the Cf target to produce the  $^{168\text{m,g}}\text{Lu}$  isotope ( $T_{1/2} = 6.7/5.5$  min) in the  $^{162}\text{Dy}(^{11}\text{B}, 5\text{n})$  reaction. The average intensity of the  $^{11}\text{B}^{4+}$  beam was 0.35 particle- $\mu\text{A}$ . The  $^{11}\text{B}^{4+}$  beam with 67.9 MeV from the JAEA tandem accelerator passed through a  $1.83 \text{ mg}/\text{cm}^2$  HAVAR vacuum window,  $0.09 \text{ mg}/\text{cm}^2$  He cooling gas, and the Be backing foil before entering the target material. The beam energy in the middle of the Cf target was 63.0 MeV. At this energy, the excitation function shows the maximum cross section for the  $^{256}\text{Lr}$  synthesis [3]. Nuclear reaction products recoiling out of the target were then transported with a He/CdI<sub>2</sub> gas-jet system to the ion-source. The helium flow rate was 1.4 L/min. The ionizer made of a tantalum tube was heated by radiant heat and by thermal electron bombardment from surrounding tungsten filaments. The inner surface of the ionizer was covered with a Re foil of 50  $\mu\text{m}$  thickness. To optimize the temperature distribution along the ionizer, we newly installed two filaments in a series (Fig. 1). One filament heated the gas-jet inlet area of the ionizer and the other one did the exit part. Ionized nuclides were accelerated by an electrical potential of 30 kV and were mass-separated with an

<sup>1</sup> Japan Atomic Energy Agency (JAEA)

<sup>2</sup> Ibaraki University

<sup>3</sup> RIKEN

<sup>4</sup> CERN

<sup>5</sup> University of Mainz

Isotope Separator On-Line (ISOL). The mass-separated ions were then implanted in thin polyethylene terephthalate foils of  $0.12 \text{ mg/cm}^2$  thickness and 20 mm diameter of the rotating wheel  $\alpha$ -particle detection system (MANON). After collection for 10 s, the wheel was stepped at 10-s intervals to successively place the implanted sample between 7-pairs of Si PIN photodiodes for  $\alpha$ -particle detection. Energy calibration was performed with standard  $^{241}\text{Am}$  and  $^{244}\text{Cm}$  sources and by making use of  $\alpha$ -emitting by-products synthesized, e.g.,  $^{151}\text{Ho}$  and  $^{213}\text{Fr}$ .

An  $\alpha$ -particle spectrum from mass-separated ions with mass number of 256 is shown in Fig. 2 (a). The  $\alpha$ -energy spectrum clearly shows  $\alpha$  particles from the decay of  $^{256}\text{Lr}$  and its granddaughter nucleus,  $^{252}\text{Fm}$  ( $T_{1/2} = 25.39 \text{ h}$ ). Figure 2 (b) indicates the decay chain fed from  $^{256}\text{Lr}$ . The ionization efficiency of Lr on the Re surface was determined to be 42% at the input power to the ion-source of 880 W. The ionization efficiency of Lu was 20% at the same input power. The present result shows that Lr is easier to be desorbed and ionized than Lu, suggesting that the IP of Lr would be lower than that of Lu.

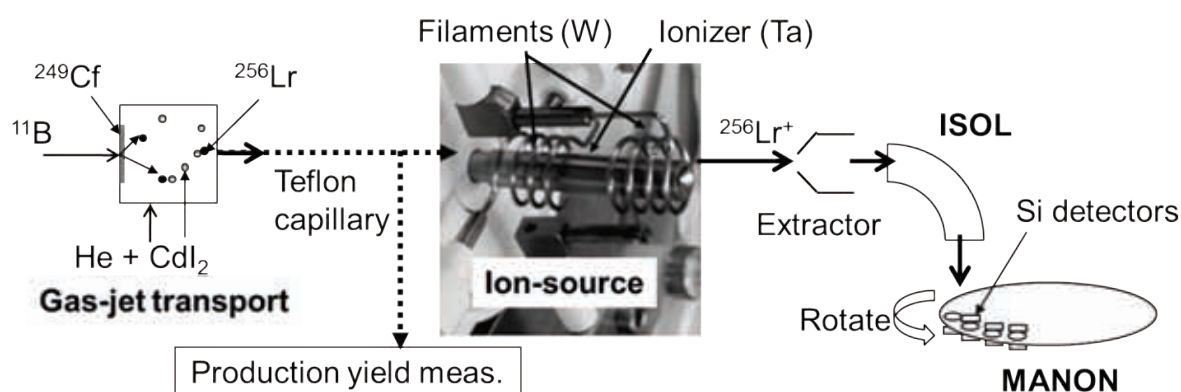


Fig. 1. Schematic view of the experimental setup including a photo of the surface ionizer with two filaments.

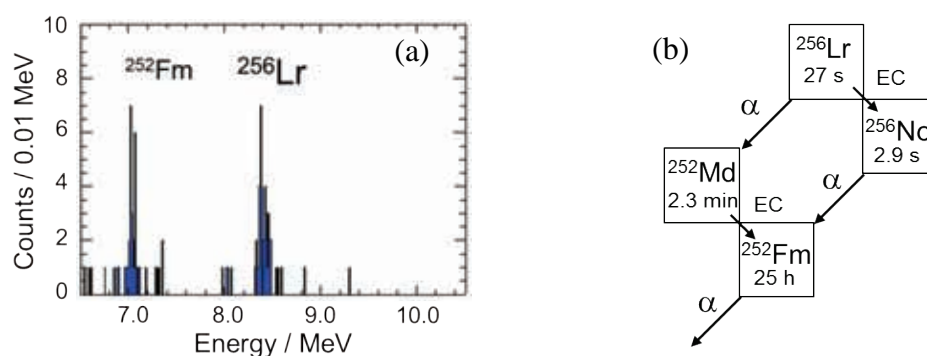


Fig. 2(a). Measured  $\alpha$ -particle spectrum of mass-separated ions with mass number of 256. (b) Decay chain fed from  $^{256}\text{Lr}$ .

## References

- [1] A. Borchovsky et al., Eur. Phys. J., D45 (2007) 115-119.
- [2] N. Sato et al., JAEA-Review 2011-040 (2011) 41-42.
- [3] N. Sato et al., JAEA-Review 2010-056 (2010) 52-53.

## 4.2 Studies on isothermal chromatographic behavior of volatile compounds of Hf isotopes with various half-lives

S. Goto<sup>1</sup>, T. Kojima<sup>1</sup>, T. Tomitsuka<sup>1</sup>, M. Murakami<sup>1</sup>, H. Kudo<sup>1</sup>,  
K. Tsukada<sup>2</sup>, M. Asai<sup>2</sup>, T.K. Sato<sup>2</sup>, A. Toyoshima<sup>2</sup>, K. Ooe<sup>2</sup>, Y. Kanaya<sup>2</sup> and Y. Nagame<sup>2</sup>

In order to clarify chemical properties of superheavy elements, a technique of a gas phase chemical separation has been applied to the chemistry experiments because it allows separating species of interest continuously and rapidly. Adsorption enthalpies of volatile compounds can be determined from their adsorption-desorption processes on a surface of gas chromatograph column. In this study, to confirm a model of an isothermal chromatography under our experimental condition, we investigated gas chromatographic behavior of volatile chloride compounds of Hf isotopes with various half-lives for the study of Rf.

Hafnium isotopes,  $^{165}\text{Hf}$  ( $T_{1/2} = 76$  s),  $^{166}\text{Hf}$  ( $T_{1/2} = 6.8$  min), and  $^{167}\text{Hf}$  ( $T_{1/2} = 2.05$  min), were produced in the  $^{151}\text{Eu}(^{19}\text{F}, \text{xn})$  reaction at the JAEA tandem accelerator facility. To compare with previous results,  $^{85}\text{Zr}$  ( $T_{1/2} = 7.9$  min) were also produced in the  $^{69}\text{Ga}(^{19}\text{F}, \text{xn})$  reaction. The Eu was electrodeposited with the thickness of  $0.1 \text{ mg}\cdot\text{cm}^{-2}$  on  $2.26 \text{ mg}\cdot\text{cm}^{-2}$  Be foil, and the Ga target was prepared with  $0.38 \text{ mg}\cdot\text{cm}^{-2}$  using Ar sputtering on  $2.16 \text{ mg}\cdot\text{cm}^{-2}$  Be foil.

The  $^{19}\text{F}^{7+}$  beam energy was 122 MeV, and the intensity was about 3  $\mu\text{A}$ . Nuclear reaction products were transported to the gas chromatographic apparatus with attaching on a carbon cluster in a He carrier gas flow. The schematic view of the apparatus is shown in Fig. 1. The carbon cluster was produced by the DC pulse discharge between carbon electrodes. The carbon also removes oxygen existing in the system which forms nonvolatile oxychlorides of Zr and Hf. The transported products were collected on quartz wool plugged in a quartz tube

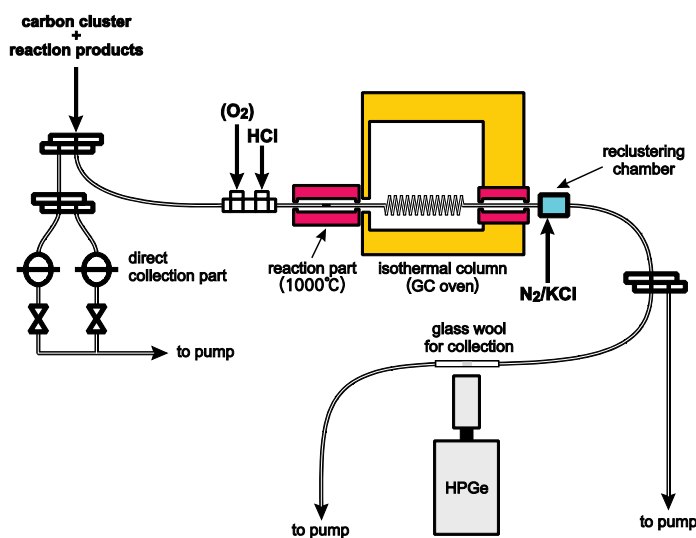


Fig. 1 Schematic view of the experimental setup.

where a reactive HCl gas was added to form volatile chloride compounds. The formed volatile compounds were then fed into an isothermal chromatographic quartz column (~2 m length) directly connected to the tube. The flow rate of He carrier gas was  $0.8 \text{ L min}^{-1}$ , the reaction temperature was  $1000^\circ\text{C}$ , and the pressure at the reaction part was about 150 kPa. The compounds of Zr and Hf through the column were

<sup>1</sup> Niigata University

<sup>2</sup> Japan Atomic Energy Agency (JAEA)

re-transported attaching on a KCl cluster in a  $N_2$  carrier gas flow, and collected on glass wool plugged in a glass tube for  $\gamma$ -rays measurement to examine the yields of these elements which passed through the column. The passed-through yields for Zr and Hf were obtained as a function of the temperature of the isothermal column.

The chromatograms are shown in Fig. 2. At lower than 350 °C, the yields were about 30% for all nuclides. It seems that these yields are due to the carbon cluster leaked from the quartz plug unexpectedly. In the cases of  $^{85}Zr$  and  $^{166}Hf$ , the temperatures to which their yields rise were about 350 °C, and these isothermal chromatographic behaviors were very similar with the previous report [1]. According to the model of the ideal isothermal chromatography, a relative yield is decided by a retention time of a volatile compound. Therefore, the more the half-life of a nuclide is short, the more a chromatogram should appear at higher temperature side. However, the chromatograms of  $^{165}Hf$  and  $^{167}Hf$  are similar with that of  $^{166}Hf$ . This behavior which is not explained with the model described above may be ascribable to a reaction chromatography [2]. In order to investigate in more detail, an analyzing of the results is now in progress.

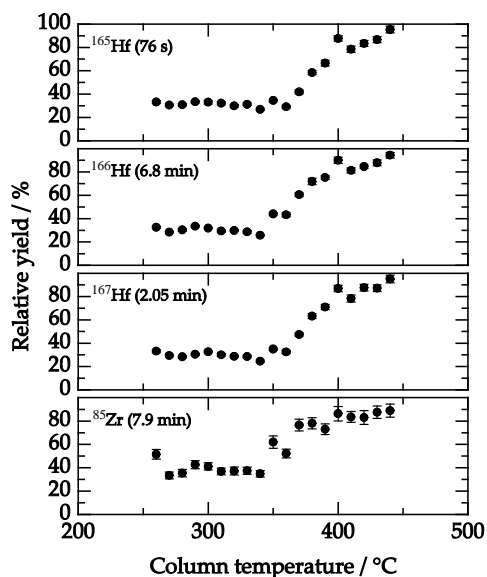


Fig. 2 Isothermal chromatograms of the compound of  $^{85}Zr$  and  $^{165-167}Hf$ .

## References

- [1] T.K. Sato et al., J. Nucl. and Radiochem. Sci., 6 (2005) N1–N3.
- [2] A. Türler et al., J. Alloys Compd., 271–273 (1998) 287–291.

### 4.3 Production and utilization of radioactive astatine isotopes using lithium ion beams

I. Nishinaka<sup>1</sup>, A. Yokoyama<sup>2</sup>, K. Washiyama<sup>2</sup>, R. Amano<sup>2</sup>, N. Yamada<sup>2</sup>, E. Maeda<sup>2</sup>, K. Li<sup>2</sup>,  
N. S. Ishioka<sup>1</sup>, K. Hashimoto<sup>1</sup>, S. Watanabe<sup>1</sup>, A. Toyoshima<sup>1</sup> and H. Makii<sup>1</sup>

An  $\alpha$  radioactive nuclide  $^{211}\text{At}$  with a half-life of 7.2 h is a prospective candidate for utilization in radioimmunotherapy. In general,  $^{211}\text{At}$  is produced through bombardment of a bismuth target with 28 MeV helium ions in the  $^{209}\text{Bi}(\alpha, 2n)^{211}\text{At}$  reaction because of the high yield required for therapeutic purpose [1]. However, the nuclear reactions using lithium ion beams,  $^{6,7}\text{Li}+\text{Pb}$  and  $^{6,7}\text{Li}+^{209}\text{Bi}$ , provide the possible production routes of  $^{211}\text{At}$ . Excitation functions have been extensively measured for the  $^{6,7}\text{Li}+^{209}\text{Bi}$  reactions to study the reaction mechanism involving complete fusion and breakup reaction of weakly bound nuclei  $^{6,7}\text{Li}$  [2-4]. For  $^7\text{Li}+\text{natPb}$ , however, only reports on production of astatine isotopes  $^{207-210}\text{At}$  have been available [5, 6]. In our previous work [6], excitation functions of  $^{208-210}\text{At}$  were measured by  $\gamma$ -ray spectrometry but that of  $^{211}\text{At}$  was not able to be measured due to low probability of  $\gamma$ -emission from the nuclide. In this work, therefore, we have measured excitation functions of  $^{208-211}\text{At}$  in the reaction of 29-57 MeV  $^7\text{Li}+\text{natPb}$  by  $\alpha$ - and  $\gamma$ -ray spectrometry.

Lead targets with thickness of 0.78-1.47 mg/cm<sup>2</sup> were prepared by vacuum evaporation onto a backing sheet of 2.7 or 5.4 mg/cm<sup>2</sup> aluminum. Each target was sandwiched between the backing and a catcher sheet of 2.7 or 5.4 mg/cm<sup>2</sup> aluminum. Irradiation was carried out with  $^7\text{Li}^{3+}$  beams of 50 and 60 MeV from the 20 MV tandem accelerator at JAEA-Tokai. Cross sections of  $^{208-210}\text{At}$  were determined by  $\gamma$ -ray spectrometry. Details of irradiation and  $\gamma$ -ray spectrometry are described in [6]. After  $\gamma$ -ray spectrometry for  $^{208-210}\text{At}$ , a dry-chemistry method was carried out to determine the cross sections of  $^{211}\text{At}$  as follows. The sample used for  $\gamma$ -ray spectrometry which consists of the bismuth target on the backing sheet and the catcher sheet was placed in a test tube with length of 18 cm and outer diameter of 18 mm. After sealing the test tube with DURA SEAL<sup>TM</sup>, a third of the portion from the bottom of the test tube was inserted into a furnace. Astatine was distilled at 650°C for 15-40 min. The test tube was taken out from the furnace and was cooled to room temperature. After opening the test tube and taking out the sample from it, the test tube was rinsed with 1.8 ml of ethanol, water, or diisopropyl ether. A portion of 5-20  $\mu\text{l}$  from this solution including astatine was deposited on a silver sheet with thickness of 0.2 mm and was evaporated to determine the amount of activity of  $^{209-211}\text{At}$  by  $\alpha$ - and  $\gamma$ -ray spectrometry. An  $\alpha$  particle energy spectrum of a deposition on a silver sheet from ethanol solution is shown in Fig. 1. The  $\alpha$ -decay from  $^{211}\text{At}$  with a branching of 41.8% occurs by  $\alpha$ -emission of 5870 keV, while the EC decay from  $^{211}\text{At}$  with a branching of 58.2% leads to  $\alpha$ -emission of 7450 keV from  $^{211}\text{gPo}$  with a short half-life of 516 ms and an  $\alpha$ -branching of 100%. Overall recovery yields of astatine were approximately 65% for ethanol and water; approximately 25% for diisopropyl ether.

The excitation functions of astatine isotopes in the  $^7\text{Li}+\text{natPb}$  ( $^{204}\text{Pb}$  1.4%,  $^{206}\text{Pb}$  24.1%,  $^{207}\text{Pb}$  22.1%, and

<sup>1</sup> Japan Atomic Energy Agency (JAEA)

<sup>2</sup> Kanazawa University

$^{208}\text{Pb}$  52.4%) reaction are shown in Fig. 2. Lines show the cross sections of  $^{208-211}\text{At}$  isotopes calculated by the HIVAP code [7]; A statistical model calculation by the HIVAP was independently carried out with the input parameters which systematically well reproduced a large number of experimental fusion-evaporation cross sections in the similar heavy ion reactions without adjusting the input parameters to fit the present experimental data [8]. It should be noted that the calculation rather well reproduces the present experimental data. Slightly larger deviations of experimental data from the calculation are observed at higher incident energies, indicating the effect of breakup reaction of  $^7\text{Li}$ .

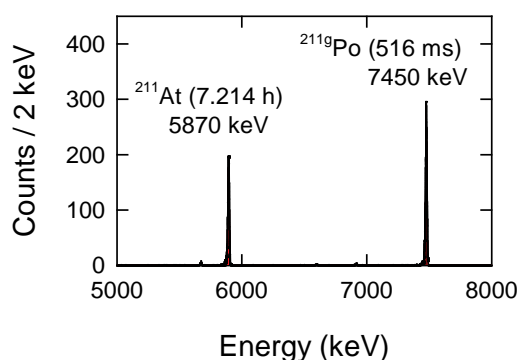


Fig. 1  $\alpha$  particle energy spectrum of a deposition on Ag from ethanol solution, produced in the 43 MeV  $^7\text{Li} + ^{\text{nat}}\text{Pb}$  reaction. The measurement with a Si surface barrier detector was carried out for 27 min. after 19 h from the end of irradiation.

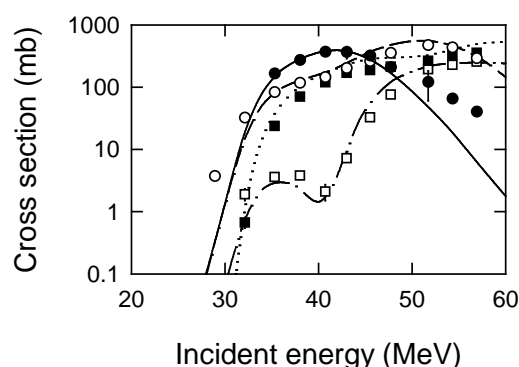


Fig. 2 Excitation functions of At isotopes in the  $^7\text{Li} + ^{\text{nat}}\text{Pb}$  reaction. The experimental and theoretical cross sections are shown by symbols and curves, respectively; solid circles and solid line:  $^{211}\text{At}$ , open circles and dashed line:  $^{210}\text{At}$ , solid squares and dotted line:  $^{209}\text{At}$ , and open squares and dash-dotted line:  $^{208}\text{At}$ .

## References

- [1] S. Lindergren, T. Bäck and H. J. Jensen, Appl. Radiat. Isot., 55 (2001) 157-160; S. Lindergren et al., J. Nucl. Med., 49 (2008) 1537-1545.
- [2] H. Freiesleben et al., Phys. Rev. C, 10 (1974) 245-249.
- [3] M. Dasgupta et al., Phys. Rev. C, 66 (2002) 04602-1-4; M. Dasgupta et al., Phys. Rev. C, 70 (2004) 024606-1-20.
- [4] Yu. E. Penionzhkevich et al., J. Phys. G, 36 (2009) 025104-1-12.
- [5] K. Roy and S. Lahiri, Appl. Radiat. Isot., 55 (2008) 571-576; M. Maiti and S. Lahiri, Phys. Rev. C, 84 (2011) 067601.
- [6] I. Nishinaka et al., JAEA-Review 2011-040 (2011) 50-51.
- [7] W. Reisdorf and M. Schädel, Z. Phys. A, 343 (1992) 47.
- [8] K. Nishio, private communication.

#### 4.4 Production of medical radio isotope, $^{95m}\text{Tc}$ . (II)

Y. Hatsukawa<sup>1</sup>, K. Hashimoto<sup>1</sup>, K. Tsukada<sup>1</sup>, T. Sato<sup>1</sup>, M. Asai<sup>1</sup>, T. Kin<sup>1</sup>,  
A. Toyoshima<sup>1</sup> and Y. Nagai<sup>1</sup>

Technetium-99m is used in radioactive isotope medical tests, for example as a radioactive tracer that medical equipment can detect in the human body. It is well suited to the role because it emits readily detectable 141 keV gamma rays, and its half-life is 6.01 hours (meaning that about 94% of it decays to  $^{99m}\text{Tc}$  in 24 hours). There are at least 31 commonly used radiopharmaceuticals based on  $^{99m}\text{Tc}$  for imaging and functional studies of the brain, myocardium, thyroid, lungs, liver, gallbladder, kidneys, skeleton, blood, and tumors. However, technetium isotopes with longer half-life and higher energy gamma-ray emitting are required for new medical research. Technetium-95m is a candidate for this purpose.

In this study,  $^{95m}\text{Tc}$  which emits some gamma rays around 800 keV was produced by the  $^{95}\text{Mo}(p,n)^{95m}\text{Tc}$  reaction. About 300-700 milligrams of  $^{\text{nat}}\text{MoO}_3$  targets were irradiated with 15 MeV proton beam for 7 hours. Averaged current was 1.2  $\mu\text{A}$ . After a week cooling time, about 700-1000 kBq of  $^{95m}\text{Tc}$  were extracted from the irradiated  $\text{MoO}_3$  target after a chemical separation. The chemical purification process used in this study is described in a former report [1].

Using purified  $^{95m}\text{Tc}$ , two kinds of labeled compounds,  $^{95m}\text{Tc}$ -MDP (**m**ethylene **d**iphosphate) and  $^{95m}\text{Tc}$ -DTPA (**d**iethylen**e**tri**a**mine **p**enta**a**cetic acid), were synthesized. In order to examine quality of the labeled compounds obtained in this study, thin-layer chromatography (TLC) method was carried out. A spot of solution of the labeled compound was placed near a short side of a TLC plate, and the plate stood with the short side down in a solvent. Two kinds of solvents, Methyl ethyl ketone (MEK) and physiological saline, were used. After about 10 min dipping time, the TLC plates were dried and taken autoradiography images using imaging plates for 12 hours. Images of  $^{95m}\text{Tc}$ -MDP and  $^{95m}\text{Tc}$ -DTPA are shown in Fig. 1. In the saline solvent, both spots of  $^{95m}\text{Tc}$ -MDP and  $^{95m}\text{Tc}$ -DTPA are moved to near the front lines. The other hand, at the case of MEK solvent, the both spots stayed at the origin points. These results suggest that the both compounds were labeled well with high radiochemical purity.

#### Reference

[1] Y. Hatsukawa et al., JAEA-Review 2011-040 (2012) 52-53.

---

<sup>1</sup> Japan Atomic Energy Agency (JAEA)

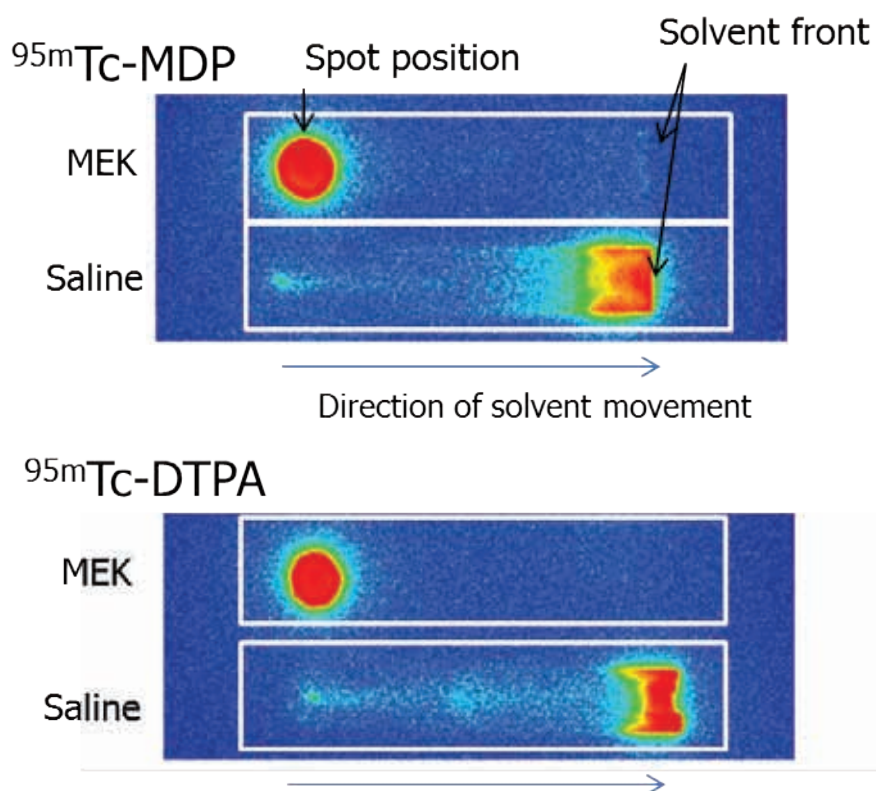


Fig 1. Autoradiography images from  $^{95m}\text{Tc-MDP}$  and  $^{95m}\text{Tc-DTPA}$ . MEK or physiological saline was used as solvents.



#### 4.5 Measurement of radioisotopes on soil in Ibaraki prefecture discharged by the accident of the Fukushima Daiichi Nuclear Power Plant

T.K. Sato<sup>1</sup>, Y. Kaneya<sup>1</sup>, M. Asai<sup>1</sup>, K. Tsukada<sup>1</sup>, A. Toyoshima<sup>1</sup>, N. Sato<sup>1</sup>, K. Ooe<sup>1</sup>, Y. Miyamoto<sup>1</sup>, K. Yasuda<sup>1</sup>, K. Ninomiya<sup>1,2</sup>, M. Matsuda<sup>1</sup>, S. Mitsuoka<sup>1</sup>, H. Ishiyama<sup>3</sup> and Y. Nagame<sup>1</sup>

The accident of the Fukushima Daiichi Nuclear Power Plant discharged a huge amount of radioisotopes, and part of them were deposited on the ground surface in the extensive region of east Japan. To investigate the deposition densities of radioisotopes and their geographical distributions, the Japanese government in collaboration with a few hundreds of researchers in universities and associations performed detailed measurements of radioisotopes deposited on soil over the whole area of Fukushima prefecture [1]. Independent of this work, we carried out measurements of radioisotopes in soil samples collected in the north and east area of Ibaraki prefecture and in the east area of Tochigi prefecture, which not only complemented the above assessment, but also revealed a detailed distribution of short-lived <sup>131</sup>I from Fukushima through Ibaraki prefecture.

Soil samplings were done on May 21-22, 2011 in Ibaraki prefecture, and on June 22, 2011 in Tochigi prefecture. We inserted a plastic cup with an inner diameter of 48 mm on the ground surface, and took soil with a depth of about 5 cm. Three samples were taken at each sampling position, and a total of 246 samples were collected at 82 sampling positions. Radioactivities in the soil samples were measured using four Ge detectors at the JAEA tandem accelerator facility. Figure 1 shows a typical  $\gamma$ -ray spectrum for a soil sample. Gamma rays associated with the  $\beta^-$  decay of <sup>134,137</sup>Cs and <sup>131</sup>I were clearly observed. To measure  $\gamma$ -ray detection efficiencies of Ge detectors for <sup>134,137</sup>Cs and <sup>131</sup>I in soil samples, we made standard soil samples containing <sup>134</sup>Cs, <sup>137</sup>Cs, <sup>175</sup>Hf, and <sup>88</sup>Zr. Solutions containing these isotopes were prepared using commercially available <sup>134</sup>Cs and <sup>137</sup>Cs solutions, and using <sup>175</sup>Hf and <sup>88</sup>Zr produced in the <sup>175</sup>Lu(p,n)<sup>175</sup>Hf and <sup>89</sup>Y(p,2n)<sup>88</sup>Zr reactions with the JAEA tandem accelerator. A small part of the solution was precisely pipetted and admixed with soil to make the standard soil sample. Another small part of the solution was pipetted on a Ta disk and evaporated to dryness to make a point source which was used to determine the radioactivity concentration of the solution. The <sup>134</sup>Cs and <sup>137</sup>Cs radioactivities in soil samples were calculated through a direct comparison of  $\gamma$ -ray count rates between soil samples and the standard ones. That of <sup>131</sup>I was derived from the 364 keV  $\gamma$ -ray count rate and its detection efficiency. The efficiency calibration curve determined by using the <sup>134</sup>Cs, <sup>137</sup>Cs, <sup>175</sup>Hf, and <sup>88</sup>Zr standard soils is shown in Fig. 2, where the efficiencies for the  $\gamma$  rays in the decay of <sup>134</sup>Cs and <sup>175</sup>Hf were corrected for cascade summing.

Figure 3 shows contour maps of deposition densities [Bq/m<sup>2</sup>] of <sup>137</sup>Cs and <sup>131</sup>I. A map of <sup>134</sup>Cs is omitted because it is similar to that of <sup>137</sup>Cs. The high deposition density of <sup>134,137</sup>Cs is found at the border among Fukushima, Ibaraki, and Tochigi prefecture, and at the north part of Tochigi prefecture. On the other hand,

<sup>1</sup> Japan Atomic Energy Agency

<sup>2</sup> Osaka University

<sup>3</sup> KEK

the distribution of  $^{131}\text{I}$  obviously differs from that of  $^{134,137}\text{Cs}$ . The highly contaminated area is found near the Pacific coast around the border of Fukushima and Ibaraki prefecture. The detailed distribution of  $^{131}\text{I}$  in Ibaraki prefecture is also clarified.

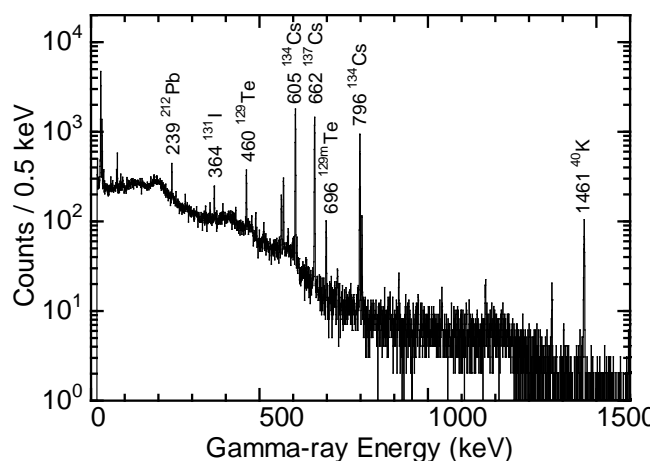


Fig. 1. Typical  $\gamma$ -ray spectrum of soil samples. Gamma rays associated with the  $\beta^-$  decay of  $^{134,137}\text{Cs}$  and  $^{131}\text{I}$  are clearly observed.

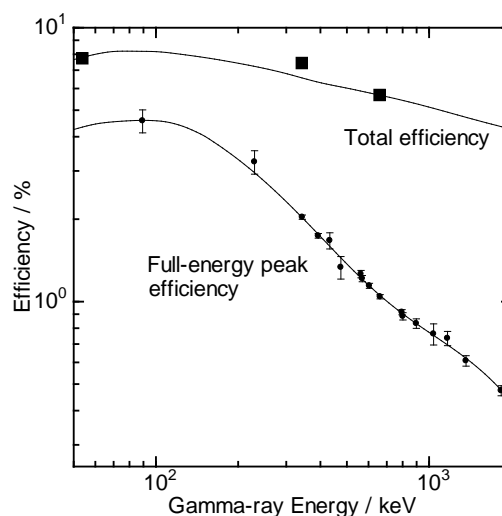


Fig. 2. Full-energy peak efficiency curve and total efficiency curve for soil samples determined by using  $^{134,137}\text{Cs}$ ,  $^{175}\text{Hf}$ , and  $^{88}\text{Zr}$  standard soil samples.

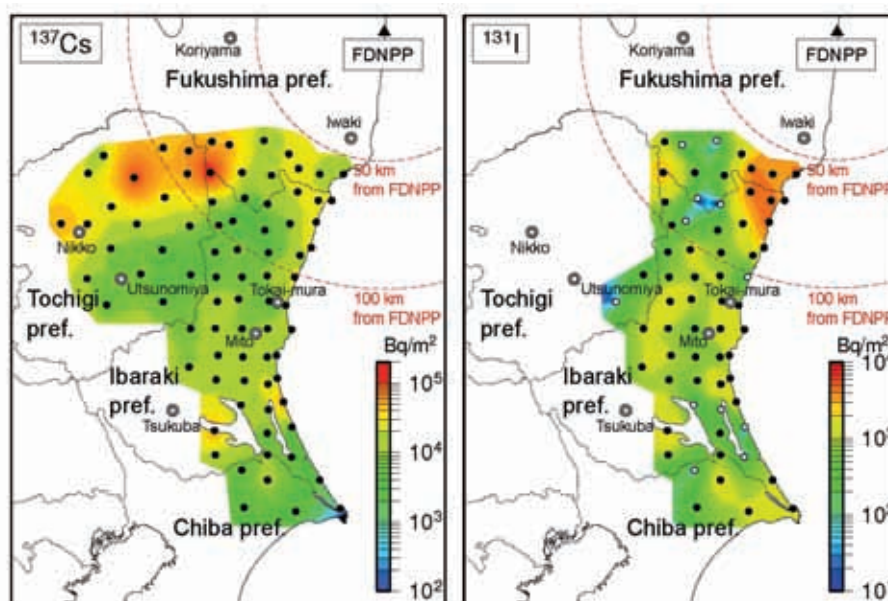


Fig. 3. Contour maps of deposition densities [ $\text{Bq/m}^2$ ] of  $^{137}\text{Cs}$  and  $^{131}\text{I}$ . Disintegration rates are decay-corrected to 0:00 on May 21, 2011. Closed circles indicate the sampling positions. Open circles indicate the sampling positions where  $^{131}\text{I}$  was not observed.

## Reference

[1] [http://radioactivity.mext.go.jp/old/ja/distribution\\_map\\_around\\_FukushimaNPP\(2011\)/](http://radioactivity.mext.go.jp/old/ja/distribution_map_around_FukushimaNPP(2011)/) (in Japanese).

## **CHAPTER 5**

### **Nuclear Theory**

- 5.1 Location of the neutron  $g_{9/2}$  orbit in neutron-rich calcium isotopes
- 5.2 Dynamical approach to heavy-ion induced fission  
using actinide target nuclei at energies around the Coulomb barrier
- 5.3 Phenomenological formula for alpha-decay half-lives

This is a blank page.

## 5.1 Location of the neutron $g_{9/2}$ orbit in neutron-rich calcium isotopes

Y. Utsuno<sup>1</sup>, T. Otsuka<sup>2</sup>, N. Shimizu<sup>2</sup>, T. Mizusaki<sup>3</sup> and M. Honma<sup>4</sup>

The evolution of the shell structure in exotic nuclei (i.e., nuclei far from stability) is one of the current interests in this field. Although conventional mean-field models give rather gradual evolution of the single-particle shell gaps, some experimental evidences have appeared which indicate that more drastic change of the shell structure occurs than the ones that the conventional mean-field models predict [1]. Recently, it has been demonstrated that an unusual evolution of the  $ls$  splitting is caused by the tensor force [2] that had been missing in the conventional mean-field models, which also accounts for the experimental result of Ref. [1]. Following the tensor-force driven shell evolution, a large neutron  $ls$  splitting at a proton  $LS$  closed configuration decreases toward a  $jj$  closed configuration with the proton number. In the case of  $Z=20-28$  region, the neutron  $ls$  splitting should be the largest at calcium isotopes. In fact, it is well known that the  $0f_{5/2}$  orbit is located very high at  $^{49}\text{Ca}$  and comes close to  $1p_{3/2}$  at  $^{57}\text{Ni}$ . Although it is also predicted that  $0g_{9/2}$  should be close to the  $pf$  orbits in calcium isotopes, there is no direct information on the location of  $0g_{9/2}$  as a nearly pure single-particle state. Note that the  $0g_{9/2}$  orbit plays a dominant role in causing a new island of deformation region around chromium isotopes with  $N\sim 40$ .

The aim of the present study is to unambiguously extract the location of the  $0g_{9/2}$  orbit in calcium isotopes from comparison between theory and experiment. Since states strongly affected by  $0g_{9/2}$  are expected to appear as strongly correlated states, a theoretical model in which the correlation is appropriately treated is required. We use the shell model for this purpose.

In order to describe unnatural parity states, a full  $1\hbar\omega$  shell-model calculation is performed in the  $sd$ - $pf$ - $sdg$  single-particle space. Namely, the unnatural parity state is described as nucleon excitation either from the  $sd$  shell to the  $pf$  shell or from the  $pf$  shell to the  $sdg$  shell. The effective interaction used here is a natural extension of the one used in the  $sd$ - $pf$  shell calculation [3]. The two-body matrix elements of the  $sd$ - $pf$  shell part are the same as that of Ref. [3] and the remaining matrix elements are calculated with the function form given in Ref. [3]. The single-particle energies of the  $sd$  and  $pf$  orbits are also the same as Ref. [3]. The shell gap between the  $pf$  shell and the  $sdg$  shell is the only free parameter in this study. This energy gap is determined so that the  $9/2^+_1$  state of  $^{51}\text{Ti}$  can be exactly reproduced because this state is known to have a large fraction of the neutron  $0g_{9/2}$  single-particle state.

Using the effective interaction thus fixed, we calculate the energy levels of neutron-rich calcium isotopes systematically, and examine the states which the  $0g_{9/2}$  orbit plays a decisive role. We focus on the systematics of the  $3^-_1$  state. In Fig. 1 (a), the excitation energies of the  $3^-_1$  states are compared between

<sup>1</sup> Japan Atomic Energy Agency (JAEA)

<sup>2</sup> University of Tokyo

<sup>3</sup> Senshu University

<sup>4</sup> University of Aizu

theory and experiment. In order to clarify the importance of the contribution of the  $0g_{9/2}$  orbit, we carry out shell-model calculations without the nucleon excitation from the  $pf$  shell to the  $sdg$  shell and also calculations without the excitation of a nucleon from the  $sd$  shell to the  $pf$  shell. Probabilities of the nucleon excitation to the  $sdg$  shell in the calculated  $3^-_1$  states are also shown in Fig. 1 (b).

It is clearly seen that while the  $3^-_1$  state is predominantly described as a proton excitation from the  $sd$  shell to the  $pf$  shell up to  $N=28$ , the neutron excitation to the  $sdg$  shell plays a crucial role beyond  $N=28$  in locating the  $3^-_1$  state at the correct excitation energy. This is consistent with the result of Ref. [4] displaying the  $3^-_1$  state located much higher than experimental position in the  $sd$ - $pf$  shell calculation without the contribution of the  $0g_{9/2}$  orbit. The  $0g_{9/2}$  orbit in neutron-rich calcium isotopes are thus determined to lie only  $\sim 2$  MeV higher than the  $0f_{5/2}$  orbit. This result confirms strong change of the  $ls$  splitting due to the tensor force.

## References

- [1] J. P. Schiffer et al., Phys. Rev. Lett., 92 (2004) 162501-1-4.
- [2] T. Otsuka et al., Phys. Rev. Lett., 95 (2005) 232502-1-4.
- [3] Y. Utsuno et al., Phys. Rev. C, 86 (2012) 051301(R)-1-6.
- [4] A. Gade et al., Phys. Rev. C, 74 (2006) 021302(R)-1-4.

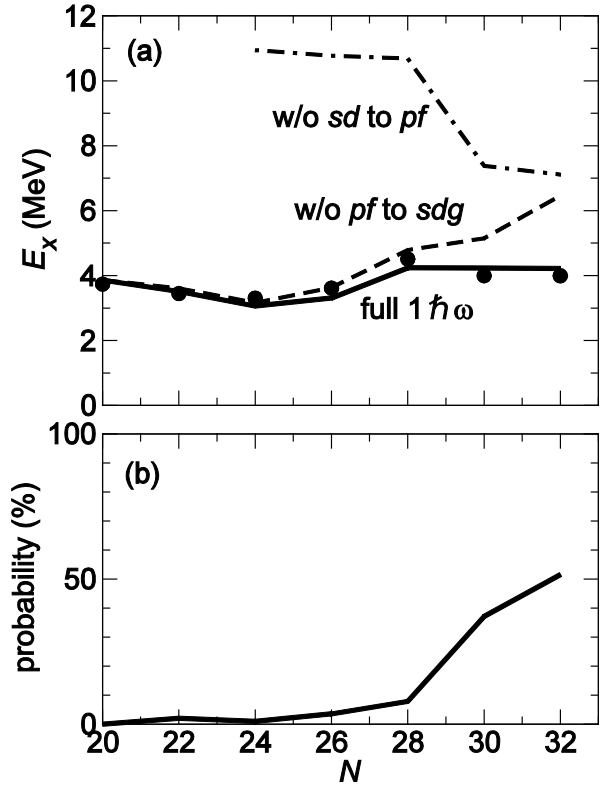


**Fig. 1** (a) Excitation energies of the  $3^-_1$  states compared between theory (lines) and experiment (symbols). The solid line denotes the full  $1\hbar\omega$  calculation, and the dashed and dot-dashed lines stand for calculations without the excitation from the  $pf$  to  $sdg$  shell and without the excitation from the  $sd$  to  $pf$  shell, respectively. (b) Probabilities of the nucleon excitation to the  $sdg$  shell in the calculated  $3^-_1$  states.

## 5.2 Dynamical approach to heavy-ion induced fission using actinide target nuclei at energies around the Coulomb barrier

Y. Aritomo<sup>1</sup>, K. Hagino<sup>2</sup>, S. Chiba<sup>1</sup> and K. Nishio<sup>1</sup>

The synthesis of superheavy elements has been carried out using heavy-ion fusion reactions between stable nuclei. In order to describe heavy-ion fusion reactions around the Coulomb barrier with an actinide target nucleus, we developed a new dynamical model, in which the effects of static nuclear deformation of a target nucleus are taken into account by considering all the orientation angles of the symmetry axis of the target nucleus [1]. The orientation effects are included both in the barrier penetration process and in the evolution of the nuclear shape. The former process is described with the coupled-channels model (CC) [2]. After the nuclear contact point, we switch to the dynamical calculation starting at the touching point assuming a nose-to-nose configuration. In the dynamical calculation, we employ the fluctuation-dissipation model with a Langevin equation. We calculate the trajectories on the time-dependent unified potential energy surface. By analyzing the trajectories, different types of fission can be separated, that is, fusion-fission (FF) and quasi-fission process (QF) [1]. With this model, the calculation could be extended to energies below the Coulomb barrier for the first time.

Recently the mass distribution of fission fragments (MDFF) and the fission cross sections ( $\sigma_{\text{fiss}}$ ) for the  $^{36,34}\text{S}, ^{30}\text{Si} + ^{238}\text{U}$  reactions were measured by the JAEA group [3]. Using this model, we analyze the experimental data for MDFF in the reaction of  $^{36}\text{S} + ^{238}\text{U}$  at several incident energies around the Coulomb barrier. The dashed-dot curve in Fig.1(a) shows the calculated capture cross sections based on the coupled-channels model for the reaction  $^{36}\text{S} + ^{238}\text{U}$  as a function of the incident energy. The experimental data are taken from Ref.[3]. One can see that this calculation reproduces the measured cross sections down to the lowest incident energy below the Bass barrier ( $V_{\text{Bass}} = 158.8$  MeV). The solid curve in Fig.1(a) shows the fusion cross section  $\sigma_{\text{fus}}$  obtained by the new model with CC and the Langevin equation. The dashed line shown in Fig. 1(a) denotes the cross section  $\sigma_{A/2 \pm 20}$ , which is derived from the yield of the fission fragments whose mass number is located within  $\pm 20$  around the symmetric fission  $A_{\text{CN}/2}$ . Notice that the fusion cross sections  $\sigma_{\text{fus}}$  are significantly smaller than  $\sigma_{A/2 \pm 20}$ . This indicates that the mass symmetric fission does not necessarily originate from the compound-nucleus state. With the new approach, by considering the nuclear shapes at the contact configuration for each orientation, we can obtain the cross sections also below the Bass barrier region.

The results for the MDFF for the reaction of  $^{36}\text{S} + ^{238}\text{U}$  are compared with the experimental data [3] in Fig.1 (b) at seven incident energies from  $E_{\text{cm}} = 148.0$  ( $E^* = 31.5$ ) MeV to  $E_{\text{cm}} = 176.0$  ( $E^* = 61.5$ ) MeV (see the histograms). At high incident energies, the mass distribution has a Gaussian-like shape centered at the symmetric mass division, whereas the mass-asymmetric fission fragments dominate at low incident

<sup>1</sup> Japan Atomic Energy Agency (JAEA)

<sup>2</sup> Tohoku University

energies. The mass-asymmetric fission produces nuclei in the vicinity of the doubly-closed shell nuclei,  $^{208}\text{Pb}$  and  $^{78}\text{Ni}$ . The trend of the experimental data, i.e., the incident energy dependence of MDFF, is well reproduced by the calculation. The mass-asymmetry with  $A_H=200$  at sub-barrier energies is also well reproduced. In Fig. 1(b) we also plot the fusion-fission events by the filled histograms. Apparently, the compound-nucleus fission has a mass-symmetric shape, and the observed mass-asymmetric fission dominated at the low incident energies is classified as QF. The strong energy dependence of the MDFF can be understood in terms of the orientation effect on the fusion and QF. The collision on the polar side has a large probability to disintegrate as QF, whereas the collision on the equatorial side has a larger fusion probability. The calculation also suggests that the measured mass-symmetric fission fragment has another origin than the compound nucleus fission. Such an event is defined as a deep quasi-fission process (DQF).

The reproduction of the experimental MDFF in this model can be the ground to support the calculated fusion probability. Furthermore, the generalized formula proposed in this model has a potential to simulate any kind of heavy-ion induced reactions in the approaching phase, such as a nucleon-transfer reaction, and to predict cross sections for the production of new nuclei.

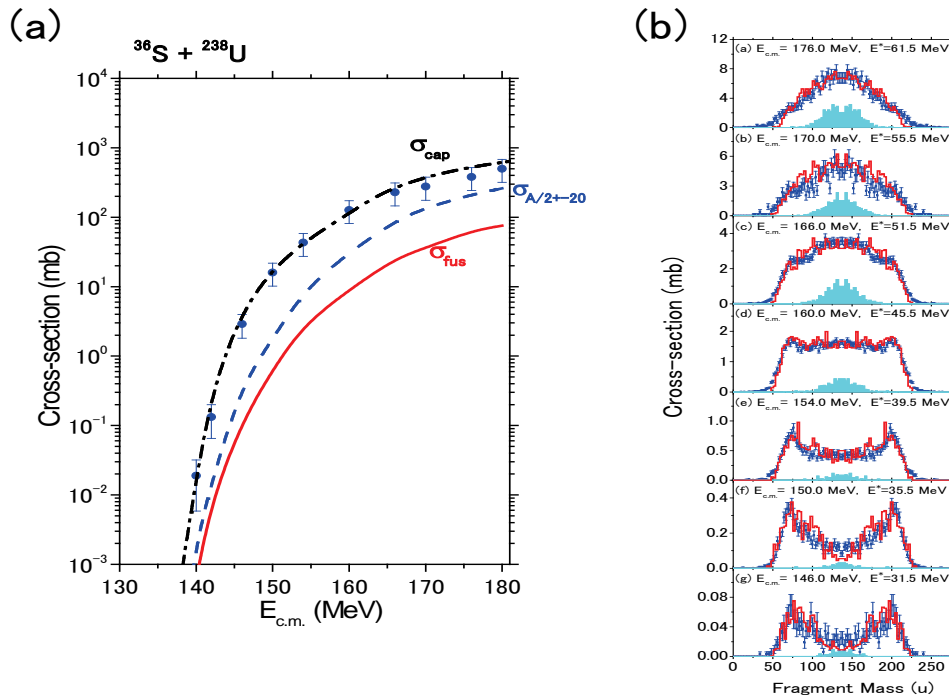


Fig. 1 (a) Excitation functions of  $\sigma_{cap}$ ,  $\sigma_{A/2\pm 20}$  and  $\sigma_{fus}$  for the  $^{36}\text{S} + ^{238}\text{U}$  reaction. The experimental data of  $\sigma_{fiss}$  are denoted by the circles [3]. (b) Mass distributions of fission fragments. The experimental data and the calculated results are denoted by the circles [3] and the histograms, respectively. The shaded areas show the calculated fusion-fission events.

## References

- [1] Y. Aritomo et al., Phys. Rev., C85 (2012) 044614.
- [2] K. Hagino, N. Rowley and A.T. Kruppa, Comput. Phys. Comm., 123 (1999) 143.
- [3] K. Nishio et al., Phys. Rev., C77 (2008) 064607; Phys. Rev., C82 (2010) 024611; Phys. Rev., C82 (2010) 044604.



### 5.3 Phenomenological formula for alpha-decay half-lives

H. Koura<sup>1</sup>

A phenomenological formula is presented for the partial half-life from the Q value for  $\alpha$  decay. It is constructed in a conventional way by considering the penetrability of a charged particle in a spherical Coulomb potential. We derive a phenomenological formula for the Gamow penetration factor based on fixed physical constants. We employ the Coulomb potential for a point charge for the penetration potential. However, this may be unsuitable because actual nuclear radii are finite and the nuclear potential reduces the total potential. To correct for this, we perform a Taylor expansion of the potential and discard higher-order terms of the expansion. The magnitude of these higher-order terms is determined by minimizing the RMS deviation from the experimental data. The partial half-life for charged particle emission is then expressed by

$$\log_{10} T_{\alpha}(s) = \frac{2}{\hbar} \sqrt{2m_{\alpha} \frac{A-4}{A} Q_{\alpha}} \cdot b \left[ \frac{\pi}{2} - 2\sqrt{\frac{R}{b}} + \frac{1}{3} \left( \frac{R}{b} \right)^{3/2} \dots \right] \log_{10} e - \log_{10} N - \log_{10} (\log_{10} e), \quad (1)$$

where  $R=r_0 A_D^{1/3} + d_0$  is the radius from the inner region where the penetration begins and  $b = Z_{\alpha} Z_D e^2 / (4\pi\epsilon_0 Q_{\alpha})$  is the radius where the penetration ends. Here, the centrifugal potential and even-odd hindrance factor appeared in the original paper [1] are removed in this report. Table 1 shows RMS deviations for selected higher-order terms. They converge at about the fourth-order term and above. The numerical integration is below the cut-off when third- and higher-order terms are included. Based on the convergence and the number of parameters, we accepted terms up to the fourth order. We obtain the following expression that contain numerical values derived from physical constants:

$$\begin{aligned} \log_{10} T_{\alpha}(s) = & 1.7195 \sqrt{\frac{A-4}{A}} Z_D / \sqrt{Q_{\alpha}(\text{MeV})} - 1.2901 \sqrt{\frac{A-4}{A}} \sqrt{R Z_D} + 0.07466 \sqrt{\frac{A-4}{A}} R^{3/2} / Z_D^{1/2} Q_{\alpha}(\text{MeV}) \\ & + 0.005499 \sqrt{\frac{A-4}{A}} R^{5/2} / Z_D^{3/2} (Q_{\alpha}(\text{MeV}))^{3/2} - \log_{10} N - 0.159175, \end{aligned} \quad (2)$$

where  $d_0=2.0$  (fm) and  $N=-21.4577$ , as shown in Table 1. These two values of adjustable parameters are well consistent with physical quantities:  $d_0$  is consistent with the size of an  $\alpha$  particle, and  $10^{-N}$  gives a reasonable order of magnitude of the product of the collision frequency of an  $\alpha$  particle and the formation probability,  $\approx 10^{20}$ , in contrast with those of conventional models such as the Viola-Seaborg formula which gives  $\approx 10^{41}$  [2]. The root-mean-square deviation from experimental partial half-lives for 153 even-even nuclei is 0.344 (in  $\log_{10}$ ), which corresponds to 2.2 times or 1/2.2. Figure 1 shows Q values, partial half-lives, and differences between calculation and experimental results for even-even nuclei.

<sup>1</sup> Japan Atomic Energy Agency (JAEA)

Recent experiments have succeeded in synthesizing superheavy nuclei. Of the decay modes that have been measured, alpha decay data provides the most information about the properties of nuclei, which is especially useful when identifying a nuclide. Figure 2 shows half-lives of alpha decay chains of selected superheavy nuclei. The half-lives we obtained are two or three times larger than those given by the Viola-Seaborg formula in this mass region. However, these data have a low statistical significance and these half-lives may not be partial half-lives because the branching ratio is mainly not obtained experimentally; our results are close to experimentally measured half-lives.

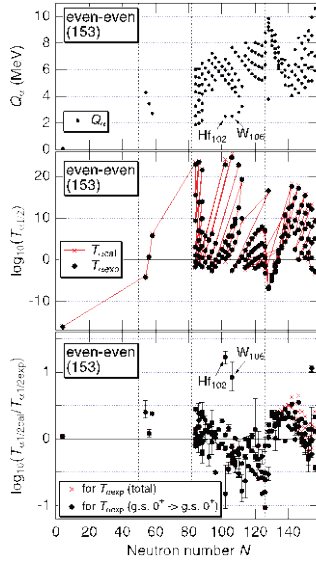


Fig. 1 Decay  $Q$  values,  $Q$ , partial half-lives,  $T_{1/2}$  (in  $\log_{10}$ ), and differences of half-lives obtained using Eq. (2) and experimental data for even-even nuclei.

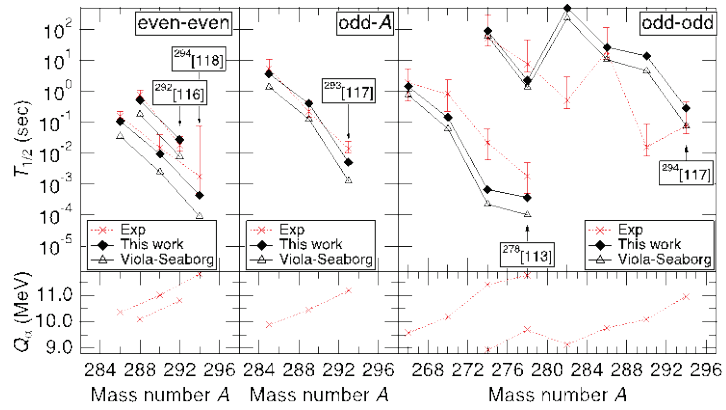


Fig. 2 Alpha decay chains for selected nuclei in the superheavy mass region.

Table 1. RMS deviation from experimental even-even nuclei when higher-order terms in the phenomenological expression are ignored. For example, '2' in the number of term column indicates that the first and the second terms up to  $-2\sqrt{R/b}$  in Equation (1) are taken. Two parameters in this table are adjusted to minimize the RMS deviation from the experimental half-lives of even-even nuclei from the  $0^+$  ground state to the  $0^+$  ground-state decay.

number of terms	1	2	3	4	5	6	...	numerical integrals
$d_0$ (fm)	—	0.5	2.0	2.0	2.0	2.0	...	4.7
$-\log_{10}(N) =$ $-\log_{10}(N_{\text{coll}} \cdot P_{\text{form}})$	-53.2984	-23.3915	-21.4186	-21.4577	-21.4581	-21.4582	...	-19.9792
RMS dev.	3.7097	0.4824	0.3475	0.3437	0.3436	0.3436	...	0.37367

## References

- [1] H. Koura, J. Nucl. Sci. Technol., 49, (2012) 816.
- [2] A. Parkhomenko and A. Sobiczewski, Acta Physica Polonica, B36, (2005) 3095.

## **CHAPTER 6**

### **Atomic Physics and Solid State Physics**

- 6.1 Charge state distribution of carbon ions after penetration of C-foil targets (II)
- 6.2 Effective charge of high-energy heavy ions in  $\text{WO}_3$  and W

This is a blank page.

## 6.1 Charge state distribution of carbon ions after penetration of C-foil targets (II)

M. Imai<sup>1</sup>, M. Sataka<sup>2</sup>, K. Kawatsura<sup>3,4</sup>, K. Takahiro<sup>5</sup>,  
K. Komaki<sup>6</sup>, K. Nishio<sup>2</sup> and H. Shibata<sup>1</sup>

Charge state is one of the most important aspects for ion interactions with matter, and affects various processes, such as electron capture, ionization, and excitation of projectile and target electrons, as well as consequent phenomena such as energy deposition into the target, *i.e.*, stopping of projectiles. Projectile charge state and its evolution are therefore essential to the study of the penetration of swift ions in matter and the data of charge-state distributions for various collision systems after exiting solid targets have been supplied [1], although the charge-state distribution changes somewhat upon exiting the target foil. As has been presented in the previous annual reports [2, 3], we have measured the exit charge state distributions for penetrations of  $S^{6+} - S^{16+}$  ions through C-foil targets of  $0.9 - 200 \mu\text{g}/\text{cm}^2$  in thickness and performed calculations by an ETACHA code [4] to succeed in reproducing the experimental results, although ETACHA has been designed for higher energy region ( $>10 \text{ MeV/u}$ ) [5]. In this report, results of our extensive measurements for carbon projectiles, between  $C^{2+}$  and  $C^{6+}$ , which are essential to precise estimation of deposited energy for heavy-ion cancer therapy, are presented with ETACHA calculations.

The experiments were performed at the LIR1–3 beam line of the 20UR Tandem Accelerator Facility. A beam of  $2.0 \text{ MeV/u}$  ( $24 \text{ MeV}$ )  $C^{2+}$  ion was provided from the Tandem Accelerator within an energy accuracy of  $0.1\%$ , and post-stripper C-foil of  $\sim 20 \mu\text{g}/\text{cm}^2$  was used to produce higher charge states. The  $C^{q+}$  ( $q = 2-6$ ) ion beam was directed into a self-support carbon foil targets of  $0.9 - 10$  and  $54 - 200 \mu\text{g}/\text{cm}^2$  in thickness for non-equilibrium and equilibrium charge distribution measurements, respectively. The charge states after foil penetration were measured using the heavy ion magnetic spectrometer ENMA and a position-sensitive gas chamber detector. The vacuum condition inside the collision chamber and the spectrometer were maintained below  $10^{-4}$  and  $10^{-6} \text{ Pa}$ , respectively, to practically eliminate background charge-exchange collisions with residual gas, which was confirmed by measurements with no foil targets.

Measured charge state evolution for  $2.0 \text{ MeV/u}$   $C^{2+} - C^{6+}$  ion incidences after penetration through C-foil targets are plotted in Fig. 1 with calculations by the ETACHA code. The measured equilibrium mean charge state and distribution width were  $5.58$  and  $0.57$ , respectively, whereas ETACHA predicts a bit higher equilibrium mean charge  $5.71$  and a bit narrow distribution width  $0.51$ . For the projectiles with charge states lower than the equilibrium mean charge, *i.e.*, for  $C^{2-5+}$  projectile ions, all the measured charge fractions except for  $C^{6+}$  showed similar dependence on target thickness that the fractions increase to show maxima in the non-equilibrium region and turn to decrease to the equilibrium values. This trend can be explained by a difference of collision cross sections or collision rates of consecutive single-charge transfers as for the sulfur projectile ions [5] and has been reproduced by the ETACHA code as seen in the figure.

---

<sup>1</sup> Kyoto University

<sup>2</sup> Japan Atomic Energy Agency (JAEA)

<sup>3</sup> Kansai Gaidai University

<sup>4</sup> Theoretical Radiation Research Laboratory

<sup>5</sup> Kyoto Institute of Technology

<sup>6</sup> RIKEN

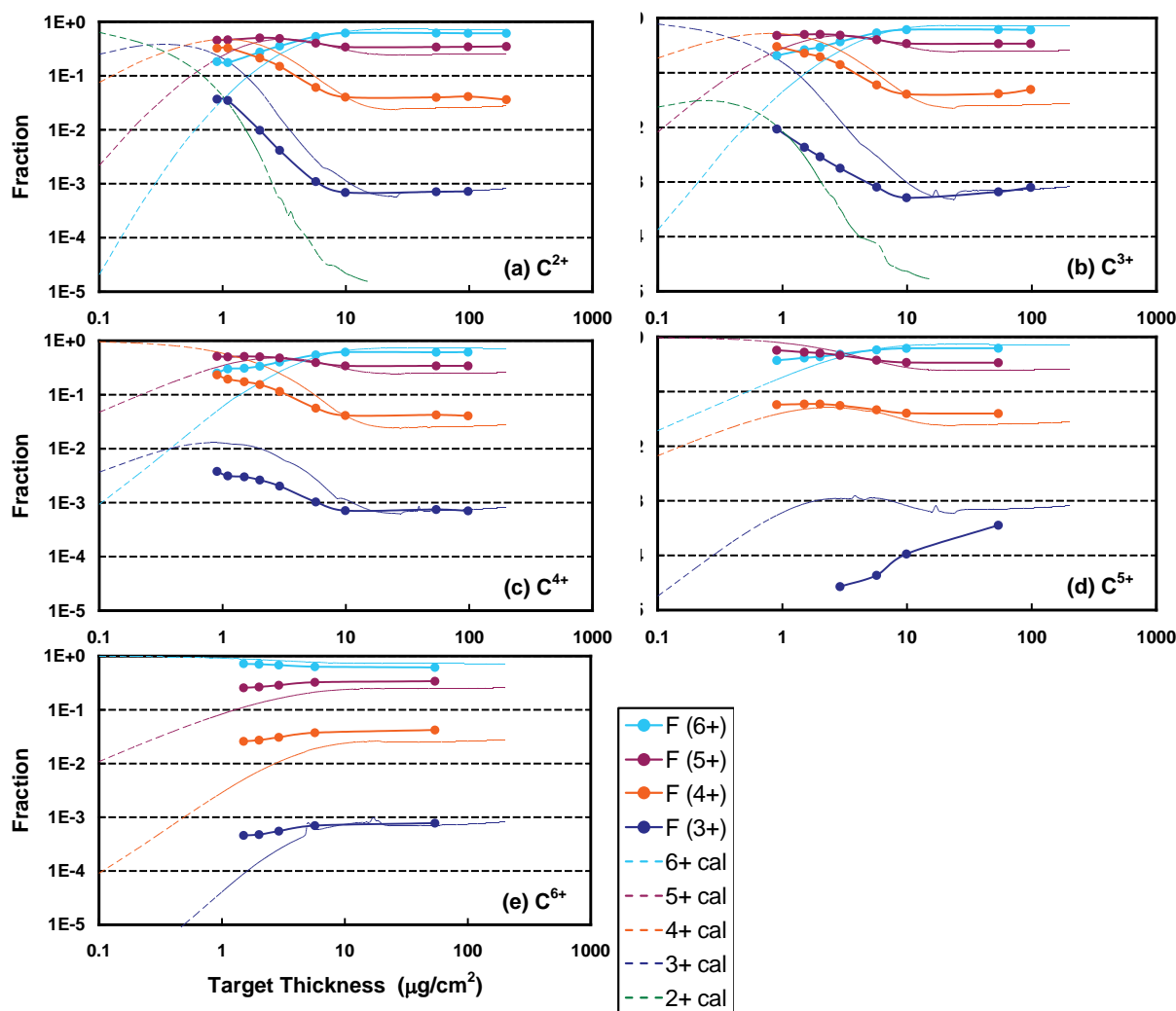


Fig. 1 Charge state evolution for 2.0 MeV/u  $C^{2+} - C^{6+}$  ion incidences after penetration through C-foil targets. Full squares with solid eye-guides are experimental results, whereas dashed curves denote calculation by an ETACHA code.

## References

- [1] A. B. Wittkower and H. D. Betz, At. Data Nucl. Data Tables 5 (1973) 113–166; K. Shima et al., *ibid.* 51 (1992) 173–241; K. Shima et al., Nucl. Instrum. Methods Phys. Res., B33 (1988) 212–215.
- [2] M. Imai et al., JAEA-Review 2007-046 (2008) 87–88; 2008-054 (2008) 89–90; 2009-036 (2009) 91–92; 2010-056 (2010) 89–90.
- [3] M. Imai, JAEA-Review 2009-006 (2009) 168–180.
- [4] J. P. Rozet et al., J. Phys. B22 (1989) 33–48; Nucl. Instrum. Methods Phys. Res., B107 (1996) 67–70.
- [5] M. Imai et al., Nucl. Instrum. Methods Phys. Res., B230 (2005) 63–67; *ibid.* B256 (2007) 11–15; *ibid.* B267 (2009) 2675–2679.

## 6.2 Effective charge of high-energy heavy ions in WO<sub>3</sub> and W

N. Matsunami<sup>1</sup>, M. Sataka<sup>2</sup> and S. Okayasu<sup>2</sup>

The electronic stopping power ( $S_e$ ) and effective charge are important for understanding material modifications by high-energy heavy ions. We have observed that the electronic sputtering yields of WO<sub>3</sub> and Cu<sub>3</sub>N films depend on the incident charge of heavy ions [1, 2]. There are two issues; the equilibrium charge state and evolution of the charge along the ion path. No data of charge state are available, except for carbon films [3, 4]. In this study, Rutherford backscattering spectrum (RBS) of WO<sub>3</sub> and W films have been measured for 90 MeV Ni<sup>+9</sup> and 60 MeV Ar<sup>+7</sup> ions and the effective charge ( $Q_{ef}$ ) of these ions has been evaluated, assuming that  $S_e$  is proportional to the square of the charge.

WO<sub>3</sub> and W films were prepared by a method described in [1]. Film thickness was evaluated from the full-width of RBS spectra using the surface approximation (estimated error < a few %) with the electronic stopping power [5] (nuclear stopping is negligibly small) and the density of  $1.87 \times 10^{22}$  and  $6.3 \times 10^{22}$  W cm<sup>-3</sup> for WO<sub>3</sub> and W. The energy resolution was obtained to be 810 and 480 keV for 90 MeV Ni and 60 MeV Ar ions by using thin Au film (~ 3 nm) on Si sample. The corresponding depth resolution for WO<sub>3</sub> is 54 and 40 nm.

RBS spectra of WO<sub>3</sub> are shown in Figs. 1 and 2. Reduction of the film thickness was observed and the sputtering yield is evaluated to be 40 and 23 for 90 MeV Ni<sup>+9</sup> and 60 MeV Ar<sup>+7</sup>, in reasonable agreement with 69 and 31 derived from 1.8 MeV He<sup>+</sup> RBS before and after the heavy ion impact. However, these sputtering yields are much smaller than those in [1]. The ion fluence in this measurement is  $\sim 10^{15}$  cm<sup>-2</sup>, far larger than  $\sim 10^{12}$  cm<sup>-2</sup> in [1] and this could be a reason of the discrepancy. The film thickness corrected for the sputtering are summarized in Table 1. Firstly, one sees that the film thickness derived from heavy-ion RBS well agrees with that from He<sup>+</sup>-ion RBS, confirming validity of the electronic stopping power.

The effective charge ( $Q_{ef}$ ) of heavy ions is evaluated using  $S_{HI} = Q_{ef}^2 S_p$  at the same energy per nucleon,  $S_{HI}$  and  $S_p$  being the electronic stopping powers of heavy ions and protons. Here, the effective charge of protons equals to 1 (high energy region). Furthermore, it is assumed that the effective charge reaches equilibrium at the depth much smaller than the film thickness. The obtained effective charge is given in Table 1. The effective charge seems to be independent of target, since the oxygen contribution to  $S_{HI}$  is comparable with that of W. As given in Table 2,  $Q_{ef}$  in C appears to be the same as that in W and WO<sub>3</sub>. This can be understood that the ion velocity is larger by an order of magnitude than the Fermi velocity of electrons in solid target [5], resulting in target independence.  $Q_{ef}$  is compared with the mean charge ( $Q_{mq}$ ) in C at equilibrium [3]. It is found that  $Q_{ef}$  is somewhat smaller (more remarkable for lower energy and heavier ion) than the mean charge. Validity that  $Q_{ef} = 1$  for proton with lower energy and  $Q^2$ -dependence of the electronic stopping are to be examined, noticing that  $Q_{2nd}$  (square root of the second moments of the charged fraction [3]) is evaluated to be the same as  $Q_{mq}$ . Further studies are under consideration, i.e., RBS with optimized scattering geometry, e. g., smaller scattering angle to minimize the energy loss of the outward path length, and thinner films for evolution of the effective charge.

<sup>1</sup> Division of Energy Science, EcoTopia Science Institute, Nagoya University

<sup>2</sup> Japan Atomic Energy Agency (JAEA)

Table 1 A summary of RBS for incident energy (E) at normal incidence and the scattering angle ( $\theta_s$ ).  $S_1$  and  $S_2$  are the electronic stopping powers of inward and outward path,  $kE$  the energy of the scattered ions at the sample surface (  $k$  the kinematic factor),  $L$  the thickness of the films and  $L$  derived using 1.8 MeV  $\text{He}^+$  ions is given in the parenthesis.  $Q_{\text{ef1}}$  and  $Q_{\text{ef2}}$  are the effective charge for E and  $kE$ .

Ions	E (MeV)	Sample	$\theta_s$ (deg.)	$S_1$ (keV/nm)	$S_2$ (keV/nm)	$kE$ (MeV)	L (nm)	$Q_{\text{ef1}}$	$Q_{\text{ef2}}$
$^{58}\text{Ni}^{+9}$	90	$\text{WO}_3/\text{MgO}$	150	12.8	9.685	26.53	410 (415)	15.55	9.61
$^{58}\text{Ni}^{+9}$	90	W/Al	150	24.0	16.58	26.53	128 (130)	15.55	9.63
$^{40}\text{Ar}^{+7}$	60	W $\text{O}_3/\text{MgO}$	165	7.61	7.39	25.15	405 (396)	11.86	9.12
$^{40}\text{Ar}^{+7}$	60	W /MgO	165	14.2	13.0	25.15	101 (100)	11.86	9.13

Table 2 Effective charge ( $Q_{\text{ef}}$ ) and equilibrium mean charge ( $Q_{\text{mq}}$ ) in C for the ions with the same energy per nucleon as in Table 1, taken after [3].

Ions	E(MeV)	E/u(MeV/u)	$Q_{\text{ef}}$	$Q_{\text{mq}}$	$Q_{\text{mq}} / Q_{\text{ef}}$
$^{58}\text{Ni}$	90	1.552	15.55	19.4	1.25
$^{58}\text{Ni}$	26.53	0.4572	9.60	14.1	1.47
$^{40}\text{Ar}$	60	1.5	11.85	13	1.1
$^{40}\text{Ar}$	25.15	0.629	9.11	10.5	1.15

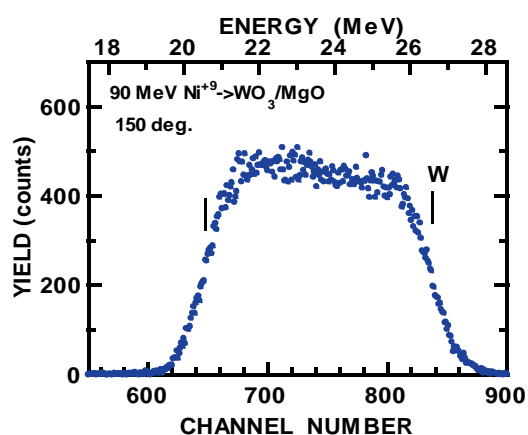


Fig. 1 RBS spectrum of 90 MeV  $\text{Ni}^{+9}$  ions for  $\text{WO}_3$  on MgO. Leading and trailing edges of the spectrum are indicated by vertical lines.

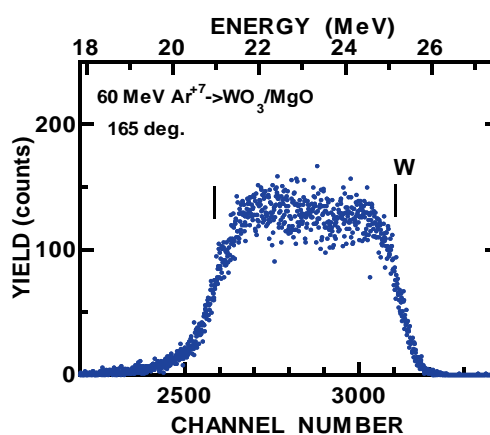


Fig. 2 RBS spectrum of 60 MeV  $\text{Ar}^{+7}$  ions for  $\text{WO}_3$  on MgO. Scattering angle is 165 deg.

## References

- [1] N. Matsunami et al., Nucl. Instrum. Methods Phys. Res., B268(2010)3167.
- [2] N. Matsunami et al., JAEA-Tokai Tandem Report 2008 p97.
- [3] K. Shima et al., Atom. Data Nucl. Data Tables 51(1992)173.
- [4] M. Imai et al., Nucl. Instrum. Methods Phys. Res., B267(2009)2675.
- [5] J.F. Ziegler, J.P. Biersack and U. Littmark, The Stopping and Range of Ions in Solids, Pergamonn Press, New York (1985).



## CHAPTER 7

### Radiation Effects in Materials

- 7.1 Dependence of ion-track size on the electronic stopping power in ion-irradiated  $\text{UO}_2$
- 7.2 Preliminary evaluation of high energy ion irradiation effects  
on electrical resistivity of ceramics
- 7.3 Shape and property control of metal nanoparticles by swift heavy ion irradiation
- 7.4 Swift heavy ion irradiation effect on structural and magnetic properties  
for epitaxial  $\text{Ba}(\text{Fe}_{0.5}\text{Mn}_{0.5})\text{O}_{3-\delta}$  thin films
- 7.5 Nano-fabrication on Ag-Zeolite using high energy heavy ion radiation
- 7.6 Application of high-aspect-ratio nanoholes  
formed by etching of latent tracks for sensors
- 7.7 Influence of multiple angled columnar defects  
on flux pinning properties in YBCO thin films

This is a blank page.

## 7.1 Dependence of ion-track size on the electronic stopping power in ion-irradiated $\text{UO}_2$

N. Ishikawa<sup>1</sup>, T. Sonoda<sup>2</sup>, T. Sawabe<sup>2</sup> and M. Sataka<sup>1</sup>

Uranium dioxide ( $\text{UO}_2$ ) fuels in light water reactors are subjected to various high-energy particles. Not only neutrons but also high-energy fission fragments play an important role in radiation damage process. Since fission fragments have high kinetic energy of about 70~100-MeV, they create radiation damages in  $\text{UO}_2$  oxide fuels. Since the radiation damage due to such high-energy heavy particles is dominantly created via high-density electronic energy deposition, the damage creation process is complicated. In order to understand the process, it is useful to utilize high-energy ion accelerator by which the energy deposition density and ion-fluence can be varied in precisely controlled manner.

One of the intriguing characteristics of the radiation damages due to high-energy ion irradiation in  $\text{UO}_2$  is the formation of continuous ion tracks along the ion-paths. If the electronic stopping power ( $S_e$ ) is sufficiently high, the ion-track in nanometer size is created [1-2]. It should be noted here that the ion-tracks created for ion-irradiated  $\text{UO}_2$  are not amorphized [1], and it is expected that the  $S_e$ -dependence of the ion-track size for amorphized ion-tracks as in ion-irradiated  $\text{Y}_3\text{Fe}_5\text{O}_{12}$  [3] and that for non-amorphized ones as in ion-irradiated  $\text{UO}_2$  may be different. The thermal spike models proposed by Szenes [4] and Toulemonde [5] can account for the  $S_e$ -dependence of ion-track size for amorphized ion-tracks, but it is not obvious that those models are automatically applicable for non-amorphized ion-track size. In the present study, various high-energy ions were irradiated to natural  $\text{UO}_2$ , and the obtained data of  $S_e$ -dependence of ion-track size is compared with the ion-track size predicted based on the thermal spike model in order to examine the formation process of non-amorphized ion-tracks.

The  $\text{UO}_2$  specimens for transmission electron microscope (TEM) were microsampled using the focused ion beam (FIB) technique. The irradiating ions were 310-MeV  $\text{Au}^{27+}$ , 150-MeV  $\text{Au}^{27+}$ , 210-MeV  $\text{Xe}^{29+}$ , 210-MeV  $\text{Xe}^{16+}$ , 150-MeV  $\text{Xe}^{27+}$ , 100-MeV  $\text{Xe}^{25+}$ , and 100-MeV  $\text{Zr}^{10+}$ . By these ions,  $S_e$  can be varied from 19.7 to 42.5 keV/nm. These ions were irradiated at room temperature. The ion-tracks created in irradiated specimens were observed by TEM. The electronic stopping power necessary for the analysis is calculated by SRIM 2008-code.

The examples of the observed ion-tracks are shown in Fig.1, where we find that the ion-tracks created by 100-MeV Xe are smaller than those created by 310-MeV Au. The dependence of ion-track size on  $S_e$  is shown in Fig.2. The ion-track size monotonically increases as increasing  $S_e$ . The velocity effect is usually observed for amorphized ion-tracks of various materials [3], while it is not observed in ion-irradiated  $\text{UO}_2$  as the present result shows. The absence of the velocity effect may be a unique characteristic of

<sup>1</sup> Japan Atomic Energy Agency (JAEA)

<sup>2</sup> Central Research Institute of Electric Power Industry (CRIEPI)

non-amorphized ion-tracks of  $\text{UO}_2$ .

The important finding is that there is a discrepancy between experimental data and theoretical prediction. All of the observed ion-track size data are smaller than the predicted values. The reason for this discrepancy is not clear at this moment, but it may be related to the difference between amorphized and non-amorphized ion-tracks. One of the possible explanations is that the non-amorphized ion-track may be melted in the early stage of local heating, but the liquid phase just recovers its crystal structure during the cooling stage. This assumes that the melted zone is not quenched as a whole during cooling process but is partially recrystallized, so that only the central part of the ion-track is observed as a consequence. In order to test this hypothesis it should be investigated in detail whether the recrystallized region, if any, has left any trace of crystal structure change around the observed ion-tracks.

Part of the present work was supported by KAKENHI (21360474).

### References

- [1] H.J. Matzke, P.G. Lucuta and T. Wiss, Nucl. Instrum. Methods Phys. Res., B166-167 (2000) 920.
- [2] T. Sonoda et al., Nucl. Instrum. Methods Phys. Res., B 268, (2010) 3277.
- [3] A. Meftah et al., Phys. Rev. B 48 (1993) 920.
- [4] G. Szenes, Phys. Rev. B 51 (1995) 8026.
- [5] M. Toulemonde et al., Matematisk-fysiske Meddelelser 52 (2006) 263.

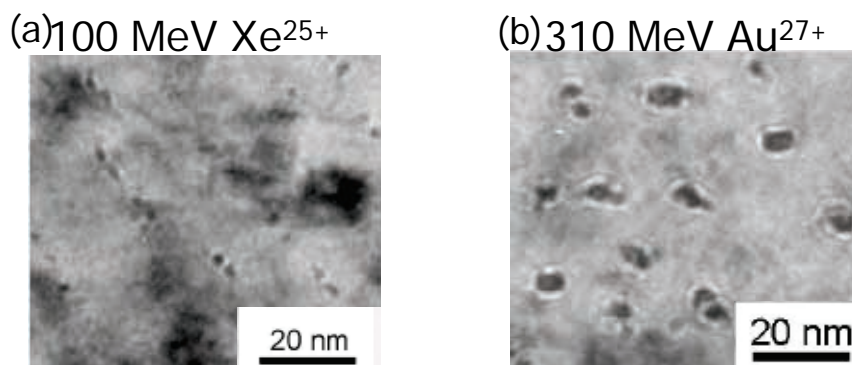


Fig. 1 Bright field images of ion tracks in  $\text{UO}_2$  irradiated with (a) 100-MeV Xe ions and with (b) 310-MeV Au

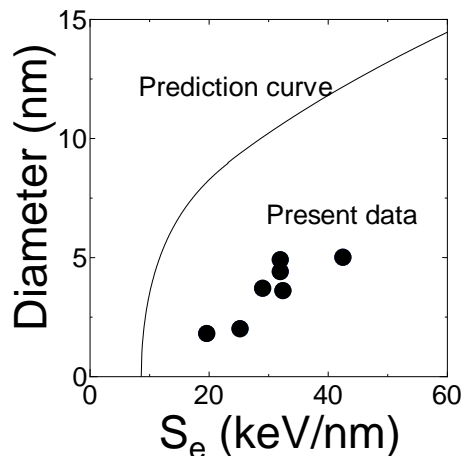


Fig. 2  $S_e$ -dependence of diameter of ion-tracks in ion-irradiated  $\text{UO}_2$ . The curve predicted based on the thermal spike model is also shown.

## 7.2 Preliminary Evaluation of High Energy Ion Irradiation Effects on Electrical Resistivity of ceramics

N. Okubo<sup>1</sup>, N. Ishikawa<sup>1</sup>, M. Sataka<sup>1</sup> and S. Jitsukawa<sup>1</sup>

Functional ceramics including  $\text{Al}_2\text{O}_3$  and  $\text{SiC}$  are attractive materials for a fusion demonstration power reactor (DEMO). Toward DEMO applications, changes of the electrical conductivity of the ceramics under irradiation must be serious problems, as well as other possible detrimental effects on the microstructure of the ceramic materials due to displacement damage, since these properties are affected by irradiation, depending on temperature and dose rate. Electrical resistivity measurements have been conducted using some irradiation sources such as a fusion neutron source (FNS) and a research reactor (JRR-3) [1, 2]. Measurements with fission neutron irradiation have been also conducted [3–5]. However, the damage levels and the primary knock-on atom (PKA) energy available for FNS and JRR-3 are limited and insufficient for the DEMO design. In this report, to understand the effects of high energy PKAs introduced by high-energy fusion neutron irradiation with a peak at 14.1 MeV, the electrical conductivity change by high energy ion irradiation is preliminarily evaluated.

The specimen configuration and the electric circuit for electrical conductivity measurement during high energy ion irradiation are shown in Fig. 1. Irradiation of 160 MeV Xe ions was conducted at the central part of thin specimen. To suppress the effect of leak current at the specimen surface sensitive to surface electron migration and carbon contamination during irradiation, the specimen with a guard ring is often applied to measure the electrical conductivity of ceramics. Irradiation area was selected by specimen mask to cover only the center electrode and monitored by both currents of center and guard ring. The thickness of the specimen was under 0.1 mm. Irradiation with high-energy Xe ions has been already verified to produce surface amorphous layer, which was caused by accumulation of ion tracks around surface region in single crystal  $\text{Al}_2\text{O}_3$  by intense electron excitation; therefore, 160 MeV Xe ions were preliminary used for  $\text{Al}_2\text{O}_3$  and also  $\text{SiC}$ .

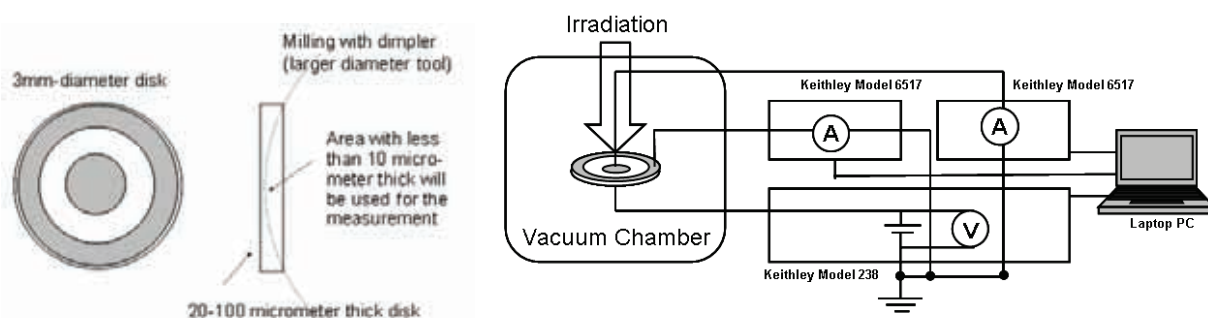


Fig. 1 Specimen configuration and electric circuit for measurements under ion irradiation

<sup>1</sup> Japan Atomic Energy Agency(JAEA)

Figure 2 shows correlation between the measured currents and the applied voltages (current-voltage characteristics) for SiC before and after irradiation at room temperature. Before irradiation, the correlation was confirmed to be ohmic by using new specimen holder and dimpled specimen. The total ion irradiation dose was about  $2 \times 10^{14}$  ions/cm<sup>2</sup>.

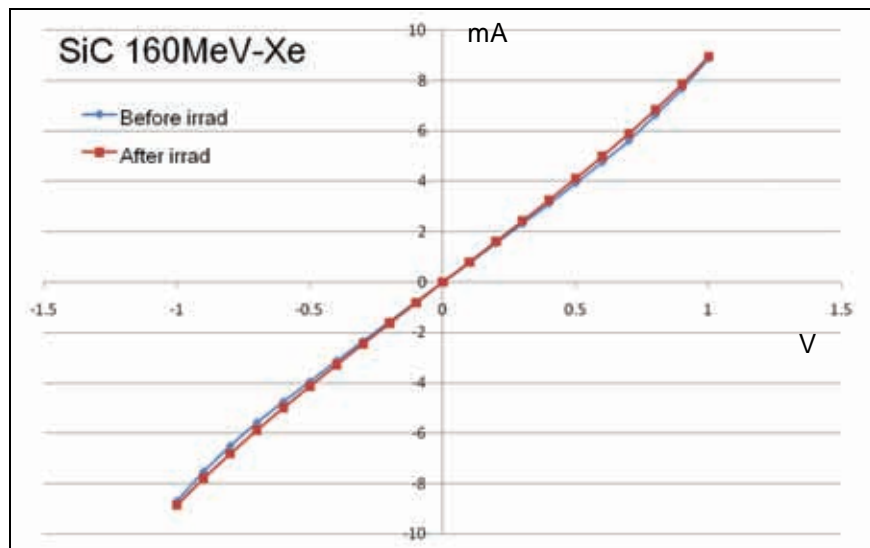


Fig.2 Correlation between the measured current and the applied voltage for SiC before, and after ion irradiation at room temperature.

The next step is to measure the electrical conductivity by using the specimen enough thinned by both dimple grinding and ion milling. Then, the electrical conductivity affected by high-energy PKA is expected to be obtained by in-situ measurement during irradiation. Irradiation with ion energies ranging one to ten times as high as that of the maximum PKA energy produced by fusion neutron irradiation will be conducted focusing on the significance of irradiation-induced microstructural change by intense electron excitation of the materials. The microstructural evaluation of irradiated specimen will be conducted next year.

## References

- [1] K. Noda et al., Fusion Eng. Des. 29 (1995) 448.
- [2] T. Tanifuji et al., J. Nucl. Mater. 253 (1998) 156.
- [3] T. Shikama et al., Ceramics in Nuclear and Alternative Energy Applications, The American Ceramics Society, (2006) 145-156.
- [4] T. Shikama, B. Tsuchiya and E.R. Hodgson, J. Nucl. Mater. 367-370 (2007) 995.
- [5] B. Tsuchiya et al., J. Nucl. Mater. 367-370 (2007) 1073.

### 7.3 Shape and property control of metal nanoparticles by swift heavy ion irradiation

H. Amekura<sup>1</sup>, N. Okubo<sup>2</sup> and N. Ishikawa<sup>2</sup>

When spherical metal nanoparticles (NPs) embedded in silica glass ( $\text{SiO}_2$ ) are irradiated by swift heavy ions (SHI), elongation of the NPs, i.e., the deformation from spheres to rods along the ion beam direction, is induced [1]. While the elongation mechanism is still under debate, one of the well-mentioned ones is the interplay of in-plane stress due to the ion hammering effect and transient melting of NPs due to the thermal spike effect.

If the melting of NPs is essential, i.e., if the elongation is mainly induced during the molten phase, larger elongation could be expected for NPs with a lower melting point (MP). To evaluate this proposition, we have compared under the same irradiation conditions the elongation behaviors of Zn NPs (MP = 420°C) [2] and of V NPs (MP = 1890°C) [3], which have largely different MPs each other. Surprisingly both the NPs showed almost the same elongation efficiency irrespective of the large MP difference, suggesting reconsideration of the elongation model.

Spherical Zn and V NPs were fabricated in different pieces of silica glass by implantation of Zn and V ions of the same energy of 60 keV. Because of the same acceleration energy and nearly the same ion masses between Zn and V ions, both the ions were implanted within almost the same depth region. Both the NPs were formed without post-implantation annealing. It was reported that the elongation behaviors depend on the initial size of NPs. Cross-sectional transmission electron microscopy (XTEM) showed that Zn and V NPs had the mean sizes of  $10.3 \pm 2.3$  nm and  $9.0 \pm 2.9$  nm in as-implanted state, respectively, which can be regarded as nearly the same size. Both the NPs were irradiated with 200 MeV

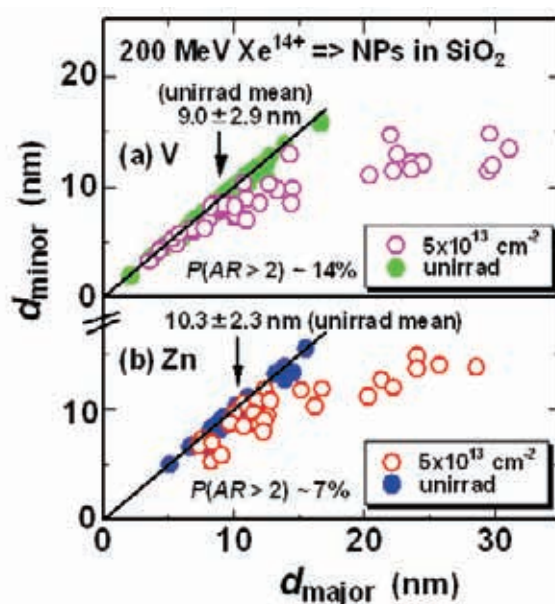


**Fig. 1.** Relationships between the major and minor dimensions ( $d_{\text{major}}$  and  $d_{\text{minor}}$ ) of (a) V NPs and (b) Zn NPs, in unirradiated state (closed circles) and after irradiation with 200 MeV  $\text{Xe}^{14+}$  ions to a fluence of  $5.0 \times 10^{13}$   $\text{Xe}/\text{cm}^2$  (open circles). The solid lines with a slope of unity indicate the relationship of spheres; i.e.,  $d_{\text{major}} = d_{\text{minor}}$ . The arrows indicate the mean diameters of the NPs in the unirradiated state.

<sup>1</sup> National Institute for Materials Science (NIMS)

<sup>2</sup> Japan Atomic Energy Agency (JAEA)

Xe<sup>14+</sup> ions up to a fluence of  $5.0 \times 10^{13}$  ions/cm<sup>2</sup>. The elongation behaviors of the NPs were evaluated by XTEM at an acceleration voltage of 200 kV.

The major and minor dimensions ( $d_{\text{major}}$  and  $d_{\text{minor}}$ ) of both the NPs before and after irradiation of  $5.0 \times 10^{13}$  Xe/cm<sup>2</sup> were plotted in Fig. 1. Before the irradiation, both Zn and V NPs were approximately spherical in shape, as seen by the distribution of the data points on the diagonal lines indicating the relationship  $d_{\text{major}} = d_{\text{minor}}$ . After the irradiation, larger NPs deviated from this relationship, becoming elongated, while the smaller NPs maintained the existing relationship, remaining approximately spherical in shape. This behavior, i.e., the existence of a minimum size threshold for elongation, was firstly speculated by D'Orleans et al. [1] but clearly established by Ridgway's group [4]. The NPs larger than the threshold size expand their major dimensions with increasing fluence, and consequently the minor dimensions decrease due to a restriction of the volume conservation. However, the minor dimensions cannot become smaller than the threshold value [4, 5], while the reason has not been clarified. Consequently, the minor dimensions  $d_{\text{minor}}$  of the NPs larger than the threshold size finally saturate around the threshold value. In the plot of  $d_{\text{major}}$  vs  $d_{\text{minor}}$ , the slope of the data line higher than the threshold size gradually decreased with the fluence, and finally becomes zero. It should be noted again that NPs smaller than the threshold size keep the diagonal relationship  $d_{\text{major}} = d_{\text{minor}}$ , even after the irradiation of  $5.0 \times 10^{13}$  ions/cm<sup>2</sup>.

In both the cases of V and Zn NPs at the fluence of  $5.0 \times 10^{13}$  Xe/cm<sup>2</sup>, almost the same slopes remain larger than the threshold size as shown in Fig. 1, indicating that both the NPs have not come to the saturated state. Since both types of the NPs show almost the same ( $d_{\text{major}}$  vs  $d_{\text{minor}}$ ) distribution and since they have not reached the saturation state, we conclude that V NPs show roughly comparable elongation to that of Zn NPs. This is surprising because the melting points of both the NPs are largely different (420°C for Zn and 1890°C for V).

## References

- [1] C. D'Orléans et al., Phys. Rev. B **67** (2003) 220101.
- [2] H. Amekura et al., Phys. Rev. B **83** (2011) 205401.
- [3] H. Amekura et al., Nucl. Instrum. Methods Phys. Res. B **269** (2011) 2730-2733.
- [4] R. Giulian et al., Phys. Rev. B **78** (2008) 125413.
- [5] G. Rizza et al., Nanotechnology **22** (2011) 175305.



## 7.4 Swift heavy ion irradiation effect on structural and magnetic properties for epitaxial Ba(Fe<sub>0.5</sub>Mn<sub>0.5</sub>)O<sub>3-δ</sub> thin films

R. Shinoda<sup>1</sup>, T. Matsui<sup>1</sup>, N. Ishikawa<sup>2</sup> and A. Iwase<sup>1</sup>

We have revealed so far that single crystalline Ba(Fe<sub>0.5</sub>Mn<sub>0.5</sub>)O<sub>3-δ</sub>(BFMO) thin films, which are synthesized on (001)SrTiO<sub>3</sub>(STO) are ferromagnetic insulators at room temperature [1]. It has also been reported that the amount of oxygen deficiencies of the BFMO thin films plays a dominant role in determining these natures of the films. On the other hand, we have shown that the 200 MeV Xe<sup>14+</sup> ion irradiation effectively displaces oxygen atoms and produces their Frenkel pairs (O vacancies and interstitials) in CeO<sub>2</sub> through the high density electronic excitation [2]. Such selective displacements of oxygen atoms can be explained as due to the thermal spike phenomenon which is correlated with the swift heavy ion induced electron excitation process [3]. Consequently, the swift heavy ion irradiation possibly becomes a potential method for the quantitative control of the oxygen vacancies in oxides.

BFMO thin films with a thickness of 60 nm were synthesized on (001)STO by a pulsed laser deposition method. For reference, the sample without introducing oxygen gas in the deposition process is also synthesized (named as 0 mTorr film, hereafter). The lattice constant was estimated by means of the x-ray diffraction. The magnetic properties were investigated by using a SQUID magnetometer. Then, four samples were irradiated with 200 MeV Xe<sup>14+</sup> ions by using a high energy ion accelerator at JAEA-Tokai. The Xe<sup>14+</sup> ions completely passed through the samples, because the 200 MeV Xe<sup>14+</sup> ion range (12.62 μm) is much larger than the BFMO films thickness (60 nm). The irradiation was performed at room temperature and the ion fluences were 1x10<sup>10</sup>, 3x10<sup>10</sup>, 1x10<sup>11</sup> and 3x10<sup>11</sup> /cm<sup>2</sup> for the four samples.

The BFMO film samples are named as sample 1 to sample 4. The values of lattice constant,  $c$ , before and after the irradiation for the four samples are shown in Fig. 1. The  $c$  increases due to the ion irradiation. The values of saturation magnetization,  $M_s$ , are shown in Fig. 2 for the irradiated four samples. The value of  $M_s$  significantly decreases by the ion irradiation. What is interesting here is that the degree of the data variability for the  $c$  and the  $M_s$  after the irradiation is definitely smaller than that before irradiation. Especially, the value of  $M_s$  seems to converge on the value for the 0 mTorr sample by the ion irradiation, irrespective of the initial  $M_s$  value. The behavior of the  $c$  and the  $M_s$  by the ion irradiation can qualitatively be explained if oxygen deficiencies are induced by the ion irradiation. Our previous work [1] has shown that the oxygen deficiency causes the change in the valence state of Fe and Mn, and the decrease in the  $M_s$ . Specifically speaking, with the increase in oxygen deficiency, the amount of Fe<sup>3+</sup> and Mn<sup>4+</sup> decreases and then the total amount of Fe<sup>3+</sup>(d<sup>5</sup>)-O<sup>2-</sup>-Mn<sup>4+</sup>(d<sup>3</sup>) ferromagnetic super-exchange coupling decreases. On the other hand, the lattice constants become larger than those for the unirradiated samples, which are consistent with the knowledge for oxide materials that the lattice generally expands with increasing the amount of the

<sup>1</sup> Osaka Prefecture University

<sup>2</sup> Japan Atomic Energy Agency (JAEA-Tokai)

oxygen deficiency. Therefore, the changes in the  $M_s$  and  $c$  due to the irradiation are ascribed to the increase in oxygen deficiencies. Here, it should be worth calculating the deposit energy density through the swift heavy ion irradiation process. When the 200 MeV  $\text{Xe}^{14+}$  ions pass through the BFMO films, the calculation by SRIM2008 code shows that the electronic stopping power,  $S_e$ , and the nuclear stopping power,  $S_n$ , are  $43.1 \text{ MeV}/(\text{mg}/\text{cm}^2)$  and  $0.166 \text{ MeV}/(\text{mg}/\text{cm}^2)$ , respectively. Therefore, for the irradiation with 200 MeV  $\text{Xe}^{14+}$  ions, the energy deposition into the sample through the electronic excitation is a dominant process. The present result can temporarily be explained that the thermal spike causes the oxygen deficiency.

Figure 3 shows the relationship between  $c$  and  $M_s$  for the samples in the present experiment as well as the samples oxygen deficiency of which is controlled by the partial oxygen pressure during the thermal treatment [1]. As can be seen in the figure, an obvious correlation can be seen between the two parameters. The correlation is about the same both for the present samples and for those thermally treated in oxygen gas with various partial pressures. This result suggests again that the ion irradiation induces the oxygen deficiencies in the samples.

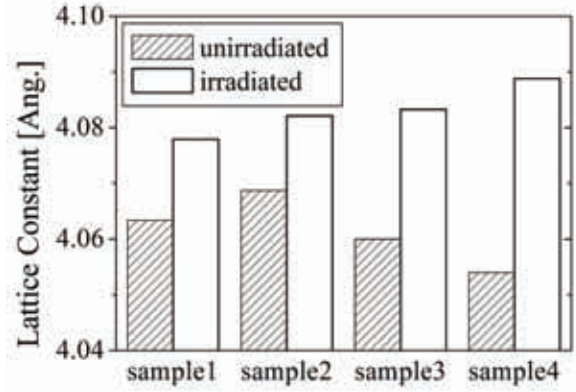


Fig. 1  $c$  for the irradiated four samples before and after irradiation.

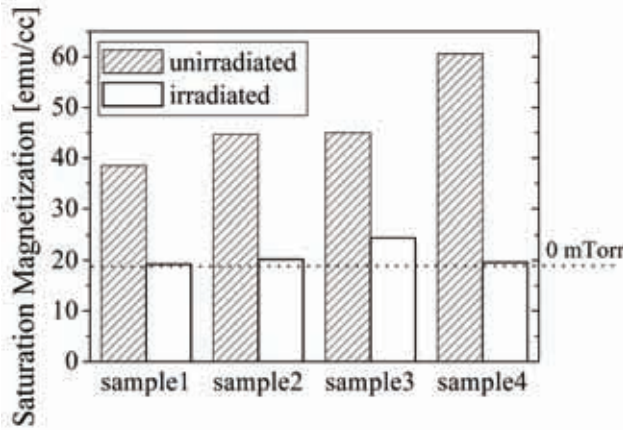


Fig. 2  $M_s$  for the irradiated four samples before and after irradiation.

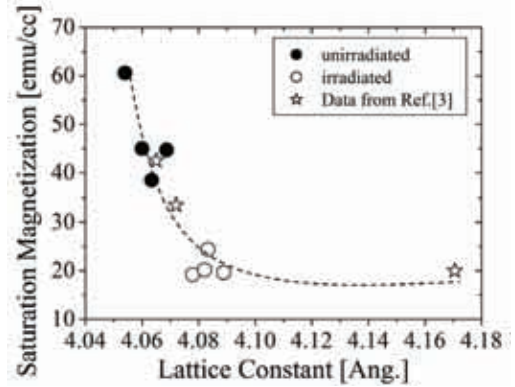


Fig. 3 Relationship between lattice constant,  $c$ , and saturation magnetization,  $M_s$ .

## References

- [1] K. Katsube et al., J. Appl. Phys. 105, 07D904 (2009).
- [2] H. Ohno et al., Nucl. Instrum. Methods Phys. Res., B266 (2008) 3013-3017.
- [3] A. Iwase et al., Nucl. Instrum. Methods Phys. Res., B146 (1998) 557-564.

## 7.5 Nano-fabrication on Ag-Zeolite using high energy heavy ion radiation

S. Okayasu<sup>1</sup> and Y. Sasaki<sup>2</sup>

High energy electron irradiations (200keV or higher) on zeolites containing silver ions (Ag-zeolites) cause the structural changes. The crystal structure becomes amorphous, and thus an ordered clusters of silver atoms are found in the amorphous regions [1]. This phenomena can be considered that an electric charge transfer from the structure to an absorbed Ag<sup>+</sup> ion due to the destruction of the crystal by the irradiation. In combination of the phenomena and high energy heavy ion irradiation techniques, we expected formations of silver clusters aligned along the ion tracks as a new technique of nano cluster fabrication. By analyzing high resolution TEM images of the microstructures of Ag-zeolites irradiated 200MeV-Au ions ( $1 \times 10^{12}$  ions/cm<sup>2</sup>), we verified the formations of ordered tracks of silver clusters (fig.1). We are now investigating the dependence of electric stopping power  $Se$  for the track formations.

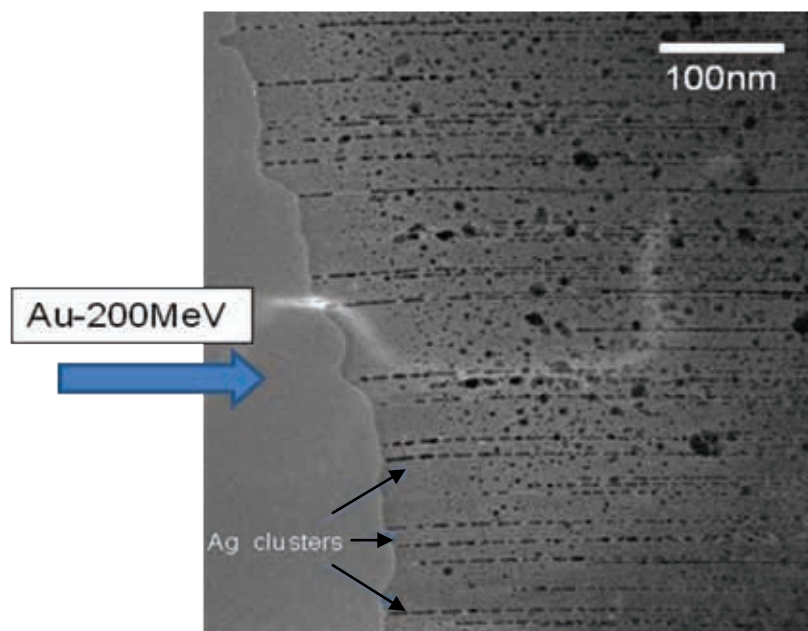


Fig.1 Aligned silver clusters formed along 200MeV-Au ion irradiation tracks.

Round shadows in this figure are considered as precipitated phases during the TEM observations.

Crystal structures of zeolites are considered to be stable. However, irradiations may cause instability of the crystal structures. The stability of the crystal structure of zeolites against irradiations will be investigated in addition to the research for formation mechanism of the clusters in the future.

### References

[1] Y. Sasaki and T. Suzuki, Mater. Trans., 50 (2009) 1050.

<sup>1</sup> Japan Atomic Energy Agency (JAEA)

<sup>2</sup> Japan Fine Ceramics Center (JFCC)

## 7.6 Application of high-aspect-ratio nanoholes formed by etching of latent tracks for sensors

M. Fujimaki<sup>1</sup>, M. Sataka<sup>2</sup> and M. Matsuda<sup>2</sup>

Highly-sensitive molecular detection sensors are required in various fields of application. We have developed an evanescent-field-coupled waveguide-mode (EFC-WM) sensor [1] and a monolithic sensing plate consisting of a SiO<sub>2</sub> glass substrate and a thin single crystalline Si layer, whose surface is thermally oxidized to form a SiO<sub>2</sub> glass waveguide for the EFC-WM sensor [2]. Figures 1(a) and 1(b) are a schematic showing of the setup of the sensor and a photograph of a prototype of the sensor, respectively. The sensing plate illuminated under the Kretschmann configuration operates as a sensor that is capable of detecting modifications in the dielectric environment near the waveguide surface with superior sensitivity by measuring change in reflectivity [1].

We have reported that the sensitivity of the EFC-WM sensor can be enhanced by perforating the waveguide layer [2]. For the perforation, selective etching of latent tracks formed in the waveguide layer by swift heavy ion irradiation is used. In the present research, to realize the mass-production of the perforated sensing plate, we tried to establish an ion irradiation process that can irradiate heavy ions in large area uniformly.

The beam line that we used was the line L2 of the 20 MV tandem accelerator at JAEA-Tokai. The ions used were 200 MeV Xe ions. The ion beam was made to be wide in the X direction by scanning it using an electromagnet (IDX Corporation) and by irradiating it to a sample through an Al foil diffuser having a thickness of 0.8  $\mu\text{m}$ . As for the sample to be irradiated, the monolithic sensing plate that had a layered structure of 84-nm Si and 480-nm SiO<sub>2</sub> on a 1.2-mm-thick SiO<sub>2</sub> substrate was used. The size of the sensing plate was 25  $\times$  25 mm and two plates were placed on a sample holder side by side as shown in Fig. 2(a). The irradiated plates were then perforated by soaking them in a 4.8% aqueous solution of HF for 2 min. The resulting nano holes were observed by scanning electron microscopy (SEM; Hitachi High-Technologies, S4800).

Figure 2(b) shows SEM images of the perforated waveguides at positions marked by dots in Fig. 2(a). In each sample, positions a, b and c are 2 mm from the left side, the center, and 2 mm from the right side of the plate, respectively. The densities of the nano holes formed in the waveguides, which correspond to the fluence of the ions, are summarized in Table 1. The result indicates that a wide irradiation with a width of 50 mm was achieved. By taking the duct diameter into account, the width of 50 mm was almost the maximum that we expected. However, the uniformity of the irradiation was poor, where the fluence at the position of Sample 1-a was 7 times smaller than that of Sample 2-b. This is due to the narrow scanning

<sup>1</sup> National Institute of Advanced Industrial Science and Technology (AIST)

<sup>2</sup> Japan Atomic Energy Agency (JAEA)

width by the electromagnet and the short distance between the electromagnet and the target. In order to obtain much uniform irradiation, we will install a high power electromagnet in a future. In the present research, since the scanning width was small, we used the Al foil diffuser to obtain a wide ion beam. However, to reduce ununiformity due to an overlap of a scanned beam, it might be desirable that a narrow beam is scanned widely. Accordingly, we will try irradiation without the diffuser.

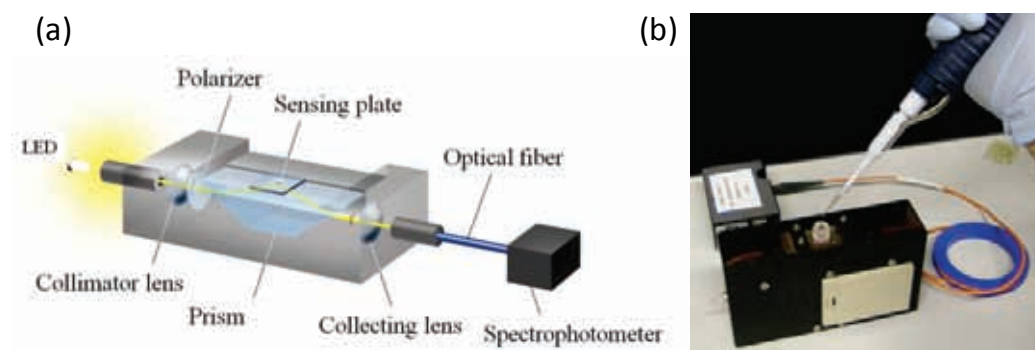


Fig. 1 Schematic showing the setup of the sensor (a) and photograph of the prototype of the sensor (b).

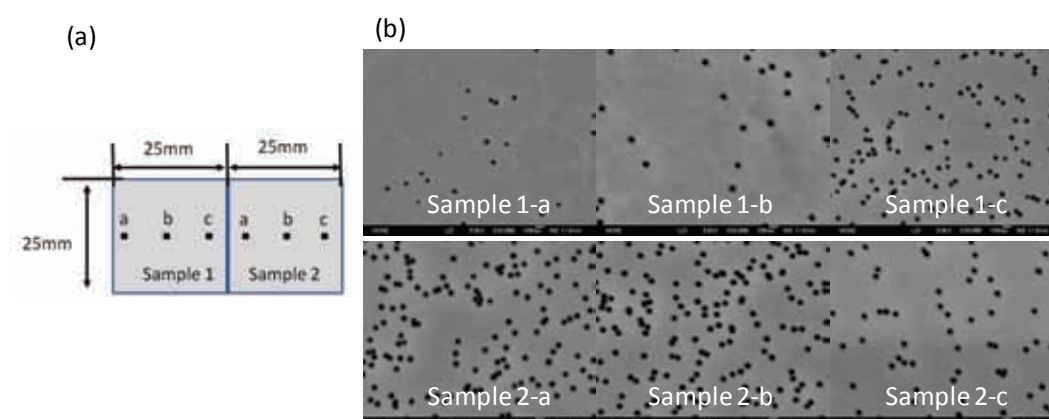


Fig. 2 (a) Alignment of the sample plates on the sample holder. The dots a, b and c indicate the positions where the SEM images were obtained. (b) SEM images obtained on Sample 1 and Sample 2.

Table 1. Densities of the nano holes formed in the waveguide layers.

Positions	1-a	1-b	1-c	2-a	2-b	2-c
holes/ $\mu\text{m}^2$	4.4	5.3	27.4	30.5	32.0	12.6

## References

- [1] M. Fujimaki et al., Microelectron. Eng. 84 (2007) 1685.
- [2] M. Fujimaki et al., Opt. Express 16 (2008) 6408.

## 7.7 Influence of multiple angled columnar defects on flux pinning properties in YBCO thin films

T. Sueyoshi<sup>1</sup>, T. Nishimura<sup>1</sup>, T. Fujiyoshi<sup>1</sup>, F. Mitsugi<sup>1</sup>, T. Ikegami<sup>1</sup> and N. Ishikawa<sup>2</sup>

For the development of second generation “coated conductors” using REBa<sub>2</sub>Cu<sub>3</sub>O<sub>y</sub> (REBCO, RE: Rare Earth element) films, further improvement of the in-field critical current density  $J_c$  has been indispensable to the operation with lower electric power losses. Line-like crystalline defects (LDs) such as columnar defects (CDs) formed by the heavy-ion irradiation are most effective to immobilize flux lines in REBCO even at a high temperature. In addition, the LDs are effective not only for the large enhancement of the in-field  $J_c$  but also for the reduction of the anisotropy of  $J_c$  which is one of the serious problems of the applications of superconductors [1]. In order to further improve the flux pinning using the LDs, it is significantly important to discern what configuration of LDs is the most effective for the flux pinning in REBCO. In addition, it is necessary to elucidate the influence of the dispersion in the LD directions on the angular dependence of  $J_c$  for the purpose of the reduction of the anisotropy of  $J_c$ . In this work, we study the influence of multiple angled CDs on flux pinning properties, where three controlled splay configurations of CDs were installed by heavy-ion irradiation in YBCO thin films: a parallel configuration of CDs, two bimodal splay configurations, and a trimodal one. In particular, it is expected that the introduction of CDs along the mid-direction of crossed CDs contributes to assist the splay effect and the more reduction of the anisotropy of  $J_c$  for the trimodal splay configurations.

The samples investigated in this work were *c*-axis oriented YBCO thin films by pulsed laser deposition (PLD) technique on SrTiO<sub>3</sub> substrates. The CDs were produced by irradiating the samples at room temperature with 200 MeV Xe ions at the tandem accelerator of JAEA in Tokai, Japan. To install the multiple angled CDs, the incident ion beam was always directed perpendicular to the bridge of sample and was tilted off the *c*-axis by  $\theta$ : all CDs are parallel to the *c*-axis (parallel CD configuration); crossed CDs inclined at  $\pm 10^\circ$  or  $\pm 45^\circ$  relative to the *c*-axis (bimodal splay configuration); crossed CDs at  $0^\circ$  or  $\pm 45^\circ$  relative to the *c*-axis (trimodal splay configuration). In all cases, the total area density of CDs corresponds to  $B_\phi = 3$  T. For the bimodal or trimodal splay configuration, the density of CDs in each direction is divided equally. Table 1 lists the specifications of the samples in this study. The transport properties were measured using a four-probe method. The transport current was applied in the direction perpendicular to the magnetic field, the *c*-axis, and CDs at all times. The value of  $J_c$  was defined by a criterion of electrical field, 1  $\mu$ V/cm.

Figure 1 shows the angular dependences of  $J_c$  and  $n$ -value for  $B = 1$  T. The  $n$ -values are extracted from linear fits to empirical relation  $E \sim J^n$  in the range of  $10^{-4} \sim 10^{-3}$  V/m. The  $n$ -value is known to be equal to  $U_0 / k_B T$ , where  $U_0$  is the pinning potential energy [2]. Of three controlled splay configurations of CDs, the

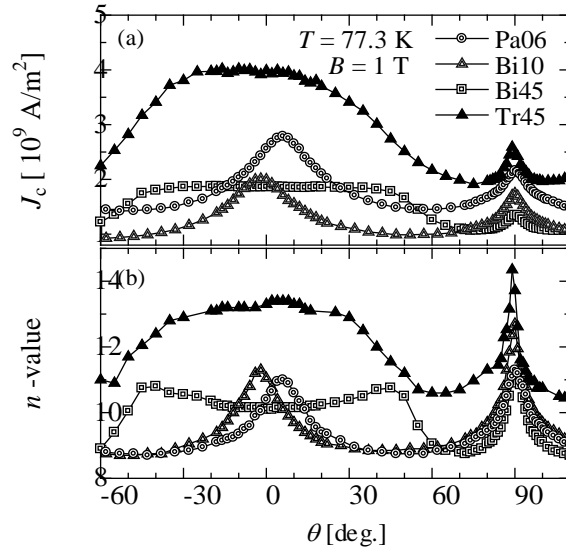
<sup>1</sup> Kumamoto University

<sup>2</sup> Japan Atomic Energy Agency (JAEA)

Table 1. Sample in this work.

Sample	Configuration of CDs	$\theta_i$	$B_\phi$ [T]	$T_{c0}$ [K]
Pa06	parallel	$6^\circ$	3	87.90
Bi10	bimodal	$\pm 10^\circ$	3	87.92
Bi45	bimodal	$\pm 45^\circ$	3	87.60
Tr45	trimodal	$0^\circ, \pm 45^\circ$	3	88.03

trimodal one is particularly interesting because both  $J_c$  and  $n$ -value of Tr45 exhibit a single broad peak in contrast with Bi45 and the excellent performance over the entire angular range at  $B = 1$  T. For the trimodal configuration, there are more choices to effectively pin the flux lines in any direction of applied magnetic field: one parallel family of CDs aligned around the direction of applied magnetic field not only captures flux lines over a considerable portion of its length, but also contributes to suppress the kink sliding along CDs inclined at large angles to applied magnetic field; the other two CD families inclining at large angles, on the other hand, would act as assistant PCs to inhibit the expansion of double kinks. Therefore, it seems that each of three parallel families of CDs plays a different role in the flux pinning, i.e. one parallel family of CDs aligned around the direction of applied magnetic field directly pin the flux lines, while the other two families of CDs act as the assist PCs. This might be also a kind of the combination effects of hybrid artificial PCs [3, 4] rather than a simple sum of pinning forces of the three parallel CD families.

Fig. 1 Angular dependences of (a)  $J_c$  and (b)  $n$ -value at 77.3 K for  $B = 1$  T.

## References

- [1] L. Civale et al., Phys. Rev. Lett. 67 (1991) 648.
- [2] E. Zeldov et al., Appl. Phys. Lett. 56 (1990) 680.
- [3] J. Hua et al., Phys. Rev. B 82 (2010) 024505.
- [4] M. Miura et al., Phys. Rev. B 83 (2011) 184519.

This is a blank page.



## **CHAPTER 8**

### **Publication in Journal and Proceedings, and Contribution to Scientific Meetings**

- 8.1 Accelerator Operation and Development
- 8.2 Nuclear Structure
- 8.3 Nuclear Reaction
- 8.4 Nuclear Chemistry
- 8.5 Nuclear Theory
- 8.6 Atomic Physics and Solid-state Physics
- 8.7 Radiation Effects in Materials

This is a blank page.

## 8.1 Accelerator Operation and Development

### Journal/Proceedings

M. Matsuda, A. Osa, S. Abe, N. Ishizaki, H. Tayama, T. Nakanoya, H. Kabumoto, M. Nakamura, K. Kutsukake, Y. Otokawa, T. Asozu, Y. Tsukihashi, S. Hanashima and T. Ishii

*The earthquake-damage of the JAEA-Tokai tandem accelerator*

Proc. of the 24th Meeting for Tandem Accelerators and their Associated Technologies, Nara, Nara women's univ. (July. 1- 2, 2011) 51-54.

M. Matsuda, T. Nakanoya, S. Hanashima and S. Takeuchi

*Development of intense high-energy noble gas ion beams from in-terminal ion injector of tandem accelerator using an ECR ion source*

Nucl. Instrum. Methods Phys. Res., A654(2011)45.

T. Nakanoya, A. Osa, S. Abe, N. Ishizaki, H. Tayama, M. Matsuda, H. Kabumoto, M. Nakamura, K. Kutsukake, Y. Otokawa, T. Asozu, Y. Tsukihashi, S. Hanashima and T. Ishii

*Present status of JAEA-Tokai tandem accelerator facility*

Proc. 24th Meeting for Tandem Accelerator and their Associated Technologies, Nara, Nara Women's Univ.(July.1-2,2011)89-92.

M. Okada, K. Niki, Y. Hirayama, N. Imai, H. Ishiyama, S.C. Jeong, I. Katayama, H. Miyatake, M. Oyaizu, Y.X. Watanabe, S. Arai, H. Makii and Y. Wakabayashi

*Low-background prebunching system for heavy-ion beams at the Tokai radioactive ion accelerator complex*

Phys. Rev. ST Accel. Beams 15 (2012) 030101.

### Meetings

M. Matsuda, A. Osa, S. Abe, N. Ishizaki, H. Tayama, T. Nakanoya, H. Kabumoto, M. Nakamura, K. Kutsukake, Y. Otokawa, T. Asozu, Y. Tsukihashi, S. Hanashima and T. Ishii

*The Earthquake-damage of the JAEA-Tokai Tandem Accelerator*

24th Meeting for Tandem Accelerator and their Associated Technologies, Nara, Nara Women's Univ.(July. 1-2,2011).

T. Nakanoya, A. Osa, S. Abe, N. Ishizaki, H. Tayama, M. Matsuda, H. Kabumoto, M. Nakamura, K. Kutsukake, Y. Otokawa, T. Asozu, Y. Tsukihashi, S. Hanashima and T. Ishii

*Present status of JAEA-Tokai tandem accelerator facility*

24th Meeting for Tandem Accelerator and their Associated Technologies, Nara, Nara Women's Univ.(July. 1-2,2011).

## 8.2 Nuclear Structure

### Meetings

M. Asai, H. Haba, K. Tsukada, N. Sato, Y. Kasamatsu, D. Kaji, K. Morimoto, K. Morita, T. K. Sato, A. Toyoshima, Y. Ishii, R. Takahashi, Y. Nagame, T. Ishii, I. Nishinaka, Y. Kojima and T. Ichikawa  
 *$\alpha$ -decay spectroscopy of Rf and Lr isotopes*

1st International Conference on Advances in Radioactive Isotope Science (ARIS 2011), Leuven, Belgium (May 29-Jun. 3, 2011).

M. Asai, H. Haba, K. Tsukada, N. Sato, Y. Kasamatsu, D. Kaji, K. Morimoto, K. Morita, T. K. Sato, A. Toyoshima, Y. Ishii, R. Takahashi, Y. Nagame, T. Ishii, I. Nishinaka, Y. Kojima and T. Ichikawa  
*Alpha-gamma and high-resolution  $\alpha$  fine-structure spectroscopy for the heaviest nuclei*

The 4th International Conference on the Chemistry and Physics of the Transactinide Elements, Sochi, Russia (Sep. 6-10, 2011).

M. Asai, H. Haba, N. Sato, Y. Kasamatsu, D. Kaji, K. Morimoto, K. Morita, Y. Shima, M. Shibata, K. Tsukada, T. K. Sato, A. Toyoshima, T. Ishii and Y. Nagame

*High-resolution  $\alpha$  fine-structure spectroscopy for studying nuclear structure of heavy nuclei*

55th Symposium on Radiochemistry, Nagano, Japan (Sep. 20-22, 2011).

M. Asai, K. Tsukada, Y. Kasamatsu, A. Toyoshima, T. K. Sato, Y. Nagame, N. Sato and T. Ishii  
*Energies of the first excited  $2+$  states in even-even actinide nuclei*

67th Annual Meeting of the Physical Society of Japan, Nishinomiya, Japan (Mar. 24-27, 2012).

## 8.3 Nuclear Reaction

### Journal/Proceedings

I. Sugai, Y. Takeda, H. Kawakami, N. Ohta, H. Makii and H. Miyatake

*Adhesion improvement of HIVIPP  $^{12}\text{C}$  targets on Au backings*

Nucl. Instrum. Methods Phys. Res., A655 (2011) 24-33.

H. Haba, D. Kaji, Y. Kudou, K. Morimoto, K. Morita, K. Ozeki, R. Sakai, T. Sumita, A. Yoneda, Y. Kasamatsu, Y. Komori, A. Shinohara, H. Kikunaga, H. Kudo, K. Nishio, K. Ooe, N. Sato and K. Tsukada

*Production of  $^{265}\text{Sg}$  in the  $^{248}\text{Cm}(^{22}\text{Ne},5n)^{265}\text{Sg}$  reaction and decay properties of two isomeric states in  $^{265}\text{Sg}$*   
Phys. Rev. C, **85**, 024611 (2012).

S. Antalic, F.P. Hessberger, D. Ackermann, S. Heinz, S. Hofmann, Z. Kalaninov'a, B. Kindler, J. Khuyagbaatar, I. Kojouharov, P. Kuusiniemi, M. Leino, B. Lommel, R. Mann, K. Nishio, S. Saro, B. Streicher, B. Sulignano and M. Venhart

*Isomeric states in  $^{253}\text{No}$  and  $^{253}\text{Fm}$*

Eur. Phys. J, **47**, 62 (2011).

K. Nishio

*Effects of nuclear orientation on fusion and fission process for reactions using  $^{238}\text{U}$  target nucleus* (Invited)  
24<sup>th</sup> International Nuclear Physics Conference 2010, Vancouver, Canada, 4-9 July, 2010 (INPC2010) (Sep. 5-8, 2006).

Journal of Physics: Conference Series **312**, 082007(1-10) (2011).

### Meetings

H. Makii, H. Miyatake, Y. Wakabayashi, H. Ishiyama, K. Niki, M. Okada, N. Imai, Y. Watanabe, Y. Hirayama, S. Jeong, T. Shima, I. Nishinaka, S. Mitsuoka and S. Chiba

*Measurement of the  $^{12}\text{C}(\alpha,\gamma)^{16}\text{O}$  reaction at TRIAC*

11th International Symposium on Origin of Matter and Evolution of Galaxies (OMEG 11), Wako, Japan (Nov. 14-17, 2011).

K. Nishio

*Study for fission properties and evaporation residue measurement in the heavy-ion induced reactions using  $^{238}\text{U}$  target nucleus*

5th International Conference FUSION11, Saint-Malo, France (May. 2-6, 2011).

K. Nishio

*Nuclear orientation in fusion and synthesis of heavy element at sub-barrier energy*

The 4<sup>th</sup> International Conference on the Chemistry and Physics of the Transactinide Elements (TAN11), Sochi, Russia (Sep. 5-11, 2011).

K. Nishio

*Nuclear orientation in fusion and synthesis of heavyelement at sub-barrier energy (Invited Talk)*

The 5<sup>th</sup> ASRC International Workshop “Perspectives in Nuclear Fission”, Tokai, Japan (Mar. 14-16, 2012).

K. Nishio

*Competition between fusion and quasifission in the heavy-ion induced reactions*

Meeting on the reaction theory based on microscopic approach, Kyoto, Japan (Sep. 28-30, 2011).

T. Nagayama, K. Nishio, S. Chiba, S. Mitsuoka, I. Nishinaka, H. Makii, K. Furutaka, Y. Wakabayashi and T. Ishii

*Development of silicon  $\Delta E$ -E detector for the surrogate reaction study*

2012 Annual Meeting of the Atomic Energy Society of Japan, (Mar.13-21, 2012).

I. Nishinaka, M. Tanikawa, K. Nishio, H. Makii, S. Mitsuoka, Y. Wakabayashi and A. Yokoyama

*Fission fragment anisotropy in heavy-ion-induced fission of actinides II*

Annual Meeting of the Japan Society of Nuclear and Radiochemical Sciences, Nagano, Japan (Sep. 20-22, 2011).

S. Ota, N. Yasuda, L. Sihver, S. Kodaira, S. Naka, Y. Ideguchi, M. Kurano and N. Hasebe

*Precise measurements of projectile charge-changing cross sections for intermediate energy heavy ions using CR-39 plastic nuclear track detectors*

11th Origin of Matter and Evolution of Galaxies, Wako, Japan, (Nov. 14-17, 2011).

Y.X. Watanabe and KISS collaboration

*Experimental project for production of neutron-rich nuclei by multinucleon transfer reaction (KISS project)*

YIPQS Long-term workshop Dynamics and Correlation in Exotic Nuclei (DCEN2011), Kyoto, Japan (Sep. 20-Oct. 28, 2011).

## 8.4 Nuclear Chemistry

### Journal/Proceedings

Y. Ishii, A. Toyoshima, K. Tsukada, M. Asai, Z. J. Li, Y. Nagame, S. Miyashita, T. Mori, H. Suganuma, H. Haba, S. Goto, H. Kudo, K. Akiyama, Y. Oura, A. Shinohara, M. Schädel, V. Pershina, and J. V. Kratz, Y. Ishii, A. Toyoshima, K. Tsukada, M. Asai, Z. J. Li, Y. Nagame, S. Miyashita, T. Mori, H. Suganuma, H. Haba, S. Goto, H. Kudo, K. Akiyama, Y. Oura, A. Shinohara, M. Schädel, V. Pershina and J. V. Kratz  
*Fluorido complex formation of element 104, rutherfordium (Rf)*  
Bull. Chem. Soc. Jpn. 84 (2011) 903.

R. Takayama, K. Ooe, W. Yahagi, H. Fujisawa, Y. Komori, H. Kikunaga, T. Yoshimura, N. Takahashi, K. Takahisa, H. Haba, Y. Kudou Y. Ezaki, A. Toyoshima, M. Asai, Y. Nagame, T. Saito, T. Mitsugashira and A. Shinohara  
*Solvent extraction of trivalent actinides with di(2-ethylhexyl) phosphoric acid*  
Proc. Radiochem. Acta 1 (2011) 157.

Z. J. Li, A. Toyoshima, M. Asai, K. Tsukada, T. K. Sato, N. Sato, T. Kikuchi, Y. Nagame, M. Schädel, V. Pershina, X. H. Liang, Y. Kasamatsu, Y. Komori, K. Ooe, A. Shinohara, S. Goto, H. Murayama, M. Murakami, H. Kudo, H. Haba, Y. Takeda, M. Nishikawa, A. Yokoyama, S. Ikarashi, K. Sueki, K. Akiyama and J. V. Kratz  
*Sulfate complexation of element 104, Rf, in  $H_2SO_4/HNO_3$  mixed solution*  
Radiochim. Acta 100, (2012) 157-164.

I. Nishinaka, Y. Kasamatsu, M. Tanikawa, S. Goto and M. Asai  
*Radiochemical study of sub-barrier fusion hindrance in the  $^{19}F + ^{209}Bi$  reaction*  
Proc. Radiochim. Acta 1 (2011) 117-121.

S. Hatsukawa, Y. Nagai, T. Kin, M. Segawa, H. Harada, O. Iwamoto, N. Iwamoto, K. Ochiai, K. Takakura, C. Konno and M. Hashimoto  
*Isotope production for medical usage using fast neutron reactions*  
Proc. Radiochim. Acta 1 (2011) 1-3.

### Meetings

N. Sato, M. Asai, K. Tsukada, T.K. Sato, A. Toyoshima, Z. J. Li, K. Ooe, T. Kikuchi, Y. Kaneya, M. Schädel, Y. Nagame and S. Ichikawa  
*Surface-ionization of lanthanides for the measurement of the first ionization potential of Lr*  
55th Symposium on Radiochemistry, Nagano, Japan (Sep. 20-22, 2011).

A. Toyoshima, Z. J. Li, M. Asai, N. Sato, T. K. Sato, K. Ooe, T. Kikuchi, Y. Kaneya, Y. Kitatsuji, K. Tsukada, Y. Nagame, M. Schädel, Y. Kasamatsu, Y. Kogama, A. Shinohara, H. Haba and J. Even  
*Determination of redox potential of mendelevium (Md)*  
 55th Symposium on Radiochemistry, Nagano, Japan (Sep. 20-22, 2011).

S. Ikarashi, K. Sueki, Z. J. Li, K. Tsukada and Y. Nagame  
*Study on cation-exchange kinetics of Zr and Hf as homologues of  $_{104}\text{Rf}$  with  $\text{H}_2\text{SO}_4$  solutions*  
 55th Symposium on Radiochemistry, Nagano, Japan (Sep. 20-22, 2011).

T. K. Sato, N. Sato, M. Asai, K. Tsukada, A. Toyoshima, Y. Kaneya, S. Ichikawa, Y. Nagame and M. Schädel  
*Development of Gas - jet coupled Surface Ion Source of ISOL for Measurement of First Ionization Potential of Lr*  
 55th Symposium on Radiochemistry, Nagano, Japan (Sep. 20-22, 2011).

Y. Kogama, Y. Kasamatsu, R. Takayama, H. Kikunaga, A. Toyoshima, K. Tsukada, M. Asai, T. K. Sato, Z. J. Li, N. Sato, T. Kikuchi, Y. Kaneya, Y. Nagame, K. Ooe, Y. Komori, T. Yoshimura, N. Takahashi and A. Shinohara  
*Solvent extraction of Bk and Md into HDEHP from  $\text{HNO}_3$  solution*  
 55th Symposium on Radiochemistry, Nagano, Japan (Sep. 20-22, 2011).

A. Toyoshima, K. Ooe, Z. J. Li, M. Asai, N. Sato, T. K. Sato, T. Kikuchi, Y. Kaneya, Y. Kitatsuji, K. Tsukada, Y. Nagame, M. Schädel, Y. Kasamatsu, Y. Kogama, A. Shinohara, H. Haba and J. Even  
*Electrochemical reduction of mendelevium in HCl solution*  
 4th International Conference on the Chemistry and Physics of the Transactinide Elements (TAN'11), Sochi, Russia (Sep. 5-11, 2011).

N. Sato, T. K. Sato, M. Asai, K. Tsukada, □A. Toyoshima, Z. J. Li, M. Schädel, □Y. Nagame, and S. Ichikawa  
*Development of a surface ionizer to measure the first ionization potential of Lr*  
 4th International Conference on the Chemistry and Physics of the Transactinide Elements (TAN'11), Sochi, Russia (Sep. 5-11, 2011).

Y. Nagame  
*Liquid Phase Experiments with the Heaviest Elements*  
 4th International Conference on the Chemistry and Physics of the Transactinide Elements (TAN'11), Sochi, Russia (Sep. 5-11, 2011).



T. K. Sato, N. Sato, M. Asai, K. Tsukada, A. Toyoshima, K. Ooe, Y. Kaneya, T. Kojima, Y. Nagame, M. Schädel and S. Ichikawa

*Study of determination of the first ionization potential of Lr - Ionization efficiencies of short-lived lanthanide isotopes -*

2012 Annual Meeting of the Chemical Society of Japan, Yokohama, Japan (Mar. 25-28, 2012).

A. Toyoshima, Z. J. Li, M. Asai, N. Sato, T. K. Sato, Y. Kaneya, Y. Kitatsuji, K. Ooe, K. Tsukada, Y. Nagame, M. Schädel, Y. Kasamatsu, A. Shinohara, H. Haba and J. Even

*Measurement of redox potential of element 101, Mendelevium*

2012 Annual Meeting of the Chemical Society of Japan, Yokohama, Japan (Mar. 25-28, 2012).

Y. Kaneya, T. K. Sato, M. Asai, K. Tsukada, A. Toyoshima, N. Sato, K. Ooe, Y. Miyamoto, K. Yasuda, K. Ninomiya, M. Matsuda, S. Mitsuoka, H. Ishiyama and Y. Nagame

*Distribution of radioisotopes on soil in north Ibaraki prefecture discharged from Fukushima Daiichi Nuclear Power Plant*

13th Symposium on Environmental Radioactivity, Tsukuba, Japan (Feb. 27-29, 2012).

M. Asai, Y. Kaneya, T. K. Sato, K. Tsukada, K. Ooe, N. Sato and A. Toyoshima

*Determination of  $\gamma$ -ray detection efficiency for  $^{134}\text{Cs}$  and  $^{131}\text{I}$  in soil sample and quantitative estimation of cascade summing effect*

Annual Meeting of the Japan Society of Nuclear and Radiochemical Sciences, Osaka, Japan, (Sept. 27, 2010).

I. Nishinaka, A. Yokoyama, K. Washiyama, R. Amano, N. Yamada, R. Ishiguro, H. Makii and K. Hashimoto

*Nuclear and radiochemical study of production and utilization of radioactive astatine isotopes using lithium ion beams at the tandem accelerator of JAEA-Tokai*

Annual Meeting of the Japan Society of Nuclear and Radiochemical Sciences, Nagano, Japan (Sep. 20-22, 2011).

## 8.5 Nuclear Theory

### Journal/Proceedings

Y. Aritomo, S. Chiba and K. Nishio

*Dynamical model of Surrogate reactions,*

Phys. Rev. C 84, (2011) 024602.

S. Chiba, O. Iwamoto and Y. Aritomo

*Spin-dependent observables in surrogate reactions*

Phys. Rev. C 84, (2011) 054602.

Y. Aritomo, K. Hagino, K. Nishio and S. Chiba

*Dynamical approach to heavy-ion induced fission using actinide target nuclei at energies around the Coulomb barrier*

Phys. Rev. C 85, (2012) 044614.

A. Gade, D. Bazin, B.A. Brown, C.M. Campbell, J.M. Cook, S. Ettenauer, T. Glasmacher, K.W. Kemper, S. McDaniel, A. Obertelli, T. Otsuka, A. Ratkiewicz, J.R. Terry, Y. Utsuno and D. Weisshaar

*In-beam  $\gamma$ -ray spectroscopy of  $^{35}\text{Mg}$  and  $^{33}\text{Na}$*

Phys. Rev. C, 83 (2011) 044305-1-5.

E.S. Diffenderfer, L.T. Baby, D. Santiago-Gonzalez, N. Ahsan, A. Rojas, A. Volya, I. Wiedenhover, A.H. Wuosmaa, M.P. Carpenter, R.V. F.Janssens, C.J. Lister, M. Devlin, D.G. Sarantites, L.G. Sobotka, Y. Utsuno and M. Horoi

*High-spin spectrum of  $^{24}\text{Mg}$  studied through multiparticle angular correlations*

Phys. Rev. C, 85 (2012) 034311-1-17.

Y. Utsuno, T. Otsuka, B.A. Brown, M. Honma and T. Mizusaki

*Structure of unstable nuclei around  $N=28$  described by a shell model with the monopole-based universal interaction*

Proceedings of the International Symposium on New Faces of Atomic Nuclei, AIP Conf. Proc., 1355 (2011) 161-166.

N. Sato, H. Haba, T. Ichikawa, D. Kaji, Y. Kudou, K. Morimoto, K. Morita, K. Ozeki, T. Sumita, A. Yoneda, E. Ideguchi, H. Koura, A. Ozawa, T. Shinozuka, T. Yamaguchi and A. Yoneda

*Production and Decay Properties of  $^{264}\text{Hs}$  and  $^{265}\text{Hs}$*

J. Phys. Soc. JPN 80, (2011) 094201-1-7.

O.V. Bessalova, I.N. Boboshin, V.V. Ermakova, B.S. Ishkhanov, A.A. Klimochkina, S.Yu. Komarov, H. Koura, E.A. Ramonovsky and T.I. Spasskaya  
*Shell Structure of Even-Even Nickel Isotopes Containing Twenty to Forty Neutrons*  
Phys. Atom. Nucl. 74, (2011) 1521-1536.

Y. Watanabe, H. Koura and S. Chiba  
*Proceedings of the 2010 Symposium on Nuclear Data*  
JAEA-Conf 2011-002 (2011).

H. Koura  
*Recent study of nuclear masses – Report of RIBF-ULIC Symposium: Physics of Rare-RI Ring –*  
*Nuclear Data News 101, (2012) 20-30 (in Japanese).*

## Meetings

Y. Aritomo, H. Hagino, K. Nishio and S. Chiba  
*Dynamical mechanism of fusion-fission process in superheavy mass region*  
The 4th International Conference on the Chemistry and Physics of the Transactinide Elements, TAN11  
Sochi, Russia (Sep. 5, 2011).

Y. Aritomo, H. Hagino, K. Nishio and S. Chiba  
*Dynamical process in heavy-ion reactions with actinide targets*  
The 7th International Conference on Dynamical Aspects of Nuclear Fission, Smolenice castle, Slovak Republic (Oct. 7, 2011).

Y. Aritomo, S. Chiba and K. Nishio  
*Dynamical model of surrogate reactions*  
Long-term Workshop on Dynamics and correlations in exotic nuclei (DCEN2011)  
Yukawa Institute for Theoretical Physics, Kyoto, Japan (Oct. 26, 2011).

Y. Aritomo, K. Hagino, K. Nishio and S. Chiba  
*Dynamical approach to heavy-ion fusion-fission reactions with deformed actinide targets at low incident energies*  
5th ASRC International Workshop :“Perspectives in Nuclear Fission”Japan Atomic Energy Agency (JAEA), Tokai, Japan (Mar. 16, 2012).

Y. Aritomo, S. Chiba and K. Nishio  
*Neutron Evaporation from fissioning nuclei by surrogate reaction*  
Annual Meeting of the Atomic Energy Society of Japan, Kokura, Japan (Sep. 21, 2010).

Y. Utsuno, T. Otsuka, B.A. Brown, M. Honma, T. Mizusaki and N. Shimizu

*Structure of exotic nuclei in the sd-pf shell described by a shell model with the monopole-based universal interaction*

The 1st International Conference “Advances in Radioactive Isotope Science (ARIS 2011)”, Leuven, Belgium (May 29-Jun. 3, 2011).

Y. Utsuno, T. Otsuka, N. Shimizu, T. Mizusaki and M. Honma

*Location of  $g_{9/2}$  orbit in neutron-rich Ca isotopes studied with the shell model*

RIBF ULIC and CNS Symposium “Frontier of gamma-ray spectroscopy (GAMMA11)”, Wako, Japan (Jun. 30-Jul. 2, 2011).

Y. Utsuno

*Evolution of the shell structure extracted from RIBF and RCNP experiments*

Fall Meeting of the Physical Society of Japan, Hirosaki, Japan (Sep. 16-19, 2011).

Y. Utsuno and S. Chiba

*Cluster states around  $^{16}\text{O}$  studied with the shell model*

YIPQS Long-term workshop “Dynamics and Correlations in Exotic Nuclei (DCEN 2011)”, Kyoto, Japan (Oct. 3, 2011).

Y. Utsuno, T. Otsuka, B.A. Brown, M. Honma, T. Mizusaki and N. Shimizu

*Shell evolution around and beyond  $N=28$  studied with a large-scale shells-model calculation*

YKIS2011 Symposium “Frontier Issues in Physics of Exotic Nuclei”, Kyoto, Japan (Oct. 11-15, 2011).

Y. Utsuno

*Recent development in the shell model: shell evolution and methodology*

ECT\* Workshop “Nuclear Structure Seen through Ground-State Properties of Exotic Nuclei”, Trento, Italy (Oct. 17-21, 2011).

Y. Utsuno

*Nuclear Physics Aspects of the Fukushima-Daiichi Accident*

The 44th Annual Meeting of the Japan Society for Safety Engineering, Yonezawa, Japan (Dec. 1-2, 2011).

Y. Utsuno

*Consideration of shell-model algorithms suitable for massively parallel computers*

HPCI Strategy Program Field 5 Workshop “Development of Nuclear Physics Study with Large-Scale Computation—Focusing on Nucleon Many-Body Systems”, Wako, Japan (Jan. 24-25, 2012).

Y. Utsuno

*Towards the establishment of the evolution of shell structure*

RCNP Workshop “Empirical Nuclear Physics”, Osaka, Japan (Feb. 22-23, 2012).

H. Koura, O. Iwamoto and S. Chiba

*Effect of Spin-parity on Surrogate Ratio Method*

Fall Meeting of the Atomic Energy Society of Japan 2011, Kita-Kyushu, (Sep. 18-21, 2011).

H. Koura

*Decay Modes and a Limit of Existence of Nuclei*

The 4th International Conference on the Chemistry and Physics of the Transactinide Elements (TAN11), Sochi, Russia, (Sep. 5-11, 2011).

H. Koura

*Importance of direct mass measurements of SHE for prediction of the island of stability*

RIBF-ULIC mini-WS on Possibility of Direct Mass Measurements of Super Heavy Elements, RIKEN (Wako), (Oct. 5, 2011).

H. Koura

*Current status on nuclear mass formulae*

RIBF-ULIC Symposium, Physics of Rare-RI Ring, RIKEN (Wako), (Nov. 10-12, 2011).

M.S. Smith, C.D. Nesaraja, E. J. Lingerfelt, H. Koura and F. G. Kondev

*Comparison of Nuclear Mass Models at nuclearmasses.org*

11th International Symposium on Origin of Matter and Evolution of Galaxies (OMEG2011), RIKEN (Wako), (Nov. 14-17, 2011).

H. Koura

*Effects of shape transitions and fission-fragment accumulations to the r-process in the neutron rich  $A=100$  region*

[RIBF-ULIC mini WS-012] Perspectives of shape transitions and beta-decay half-lives in the neutron rich  $A=100$  region near the r-process, RIKEN (Wako), (Dec. 27, 2011).

## 8.6 Atomic Physics and Solid-state Physics

### Journal/Proceedings

M. Imai

*Ion-Atom Collisions*

Handbook of Atomic and Molecular Processes in Plasmas (in Japanese), 133-179,

eds. S. Hamaguchi, I. Murakami, D. Kato, and the Japan Society of Plasma Science and Nuclear Fusion Research, Osaka University Press 2011.

### Meetings

N. Matsunami, Y. Sakuma, M. Sataka, S. Okayasu and H. Kakiuchida

*Ion irradiation effects copper-oxide(CuO) films*

2011 Fall Meeting, Japan Physical Society, Toyama, Japan (September 21, 2011).

N. Matsunami, T. Teramoto, Y. Sakuma, S. Okayasu and M. Sataka

*Ion irradiation effects on WN*

2012 Spring Meeting, Japan Physical Society, Nishinomiya, Japan (March 25, 2012).

## 8.7 Radiation Effects in Materials

### Journal/Proceedings

N. Ishikawa and K. Takegahara

*Radiation damages in CeO<sub>2</sub> thin films irradiated with ions having the same nuclear stopping and different electronic stopping powers*

Nucl. Instrum. Methods Phys. Res., B 272 (2012) 227.

N. Ishikawa, T. Sonoda, Y. Okamoto, T. Sawabe, K. Takegahara, S. Kosugi and A. Iwase

*X-ray study of radiation damage in UO<sub>2</sub> irradiated with high-energy heavy ions*

J. Nucl. Mater., 41 (2011) 392.

Y. Tahara, K. Shimizu, N. Ishikawa, Y. Okamoto, F. Hori, T. Matsui and A. Iwase

*Study on effects of energetic ion irradiation in Gd<sub>2</sub>O<sub>3</sub>-doped CeO<sub>2</sub> by means of synchrotron radiation X-ray spectroscopy*

Nucl. Instrum. Methods Phys. Res., B277(2011)53-57.

K. Shimizu, S. Kosugi, Y. Tahara, K. Yasunaga, Y. Kaneta, N. Ishikawa, F. Hori, T. Matsui and A. Iwase

*Change in magnetic properties induced by swift heavy ion irradiation in CeO<sub>2</sub>*

Nucl. Instrum. Methods Phys. Res., B: Corrected Proof, Available online (2012).

N. Ishikawa, T. Sonoda, Y. Okamoto, T. Sawabe, K. Takegahara, S. Kosugi and A. Iwase

*X-ray study of radiation damage in UO<sub>2</sub> irradiated with high-energy heavy ions*

J. Nucl. Mater., 41( 2011)392-396.

S. Kosugi, Nao Fujita, T. Matsui, F. Hori, Y. Saitoh, N. Ishikawa, Y. Okamoto and A. Iwase

*Effect of high temperature annealing on ferromagnetism induced by energetic ion irradiation in FeRh alloy*

Nucl. Instrum. Methods Phys. Res., B269(2011)869-872.

Y. Tahara, B. Zhu, S. Kosugi, N. Ishikawa, Y. Okamoto, F. Hori, T. Matsui and A. Iwase

*Study on effects of swift heavy ion irradiation on the crystal structure in CeO<sub>2</sub> doped with Gd<sub>2</sub>O<sub>3</sub>*

Nucl. Instrum. Methods Phys. Res., B269(2011)886-889.

S. Kosugi, T. Matsui, N. Ishikawa, M. Itou, Y. Sakurai, K. Aikoh, K. Shimizu, Y. Tahara, F. Hori and A. Iwase

*Study on ion-irradiation-induced ferromagnetism in FeRh intermetallic compound by means of magnetic Compton scattering*

J. Appl. Phys. 109, 07B737 (2011); 3559469.

Y.Sasaki and T.Suzuki,

*Formation of Ag Clusters by Electron Beam Irradiation on Ag-Zeolite*  
Materials Transactions, **50** (2009)1050.

H. Amekura, N. Ishikawa, N. Okubo, Y. Nakayama and K. Mitsuishi

*Asynchronous melting of embedded metal nanoparticles and silica matrix for shape elongation induced by swift heavy ion irradiation.*

Nucl. Instrum. Methods Phys. Res., B 269 (2011) 2730.

H. Amekura, M.L. Sele, N. Ishikawa and N. Okubo

*Thermal stability of embedded metal nanoparticles elongated by swift heavy ion irradiation: Zn nanoparticles in a molten state but preserving elongated shapes.*

Nanotechnology 23 (2012) 095704.

T. Sueyoshi, T. Nishimura, T. Fujiyoshi, F. Mitsugi, T. Ikegami and N. Ishikawa

*Influence of crossing angles of columnar defects on vortex glass transition in YBCO thin films*

Physica C 471 (2011) pp.1029-1032.

T. Sueyoshi, T. Nishimura, T. Fujiyoshi, F. Mitsugi, T. Ikegami and N. Ishikawa

*Influence of multiple angled columnar defects on critical current density and n-value in YBCO thin films*

Physics Procedia 36 (2012)1570-1575.

## Meetings

N. Ishikawa, T. Sonoda, T. Sawabe, H. Sugai and M. Sataka

*Ion-track formation in UO<sub>2</sub> irradiated with High-Energy Heavy Ions*

European Materials Research Society (E-MRS) , Nice, France (May 9-13, 2011).

N. Ishikawa, T. Sonoda, T. Sawabe and M. Sataka

*Ion track formation in UO<sub>2</sub> irradiated with high energy ions*

Annual meeting of the Physical Society of Japan, Nishinomiya, Japan (Mar. 24-27, 2012).

Y.Sasaki, M. Kobayashi, H. Kita and S. Okayasu

*Formation of metal microstructures induced by heavy ion irradiation in Ag-zeolite*

The 2nd International Symposium on Advanced Microscopy and Theoretical Calculations AMTC2.

H. Amekura, N. Ishikawa, N. Okubo, D. Tsuya, Y. Nakayama and K. Mitsuishi

*Embedded ZnO nanoparticles irradiated with swift heavy ions: Irradiation-induced formation of metal phase and elongation.*

The 21th MRS-Japan Academic Symposium, Yokohama, Japan (Dec. 19-21, 2011).



T. Sueyoshi, T. Nishimura, T. Fujiyoshi, F. Mitsugi, T. Ikegami and N. Ishikawa

*Influence of multiple angled columnar defects on critical current density and  $n$ -value in YBCO thin films*

Superconductivity Centennial Conference 2011 (SCC2011), Hague, Netherlands (Sep. 18-23, 2011).

This is a blank page.

## **CHAPTER 9**

### **Personnel and Committee**

9.1 Personnel

9.2 Research Planning and Assessment Committee

This is a blank page.

## 9.1 Personnel

### Department of Research Reactor and Tandem Accelerator

Takeshi	Maruo	Yamashita	Director
Tetsuo	Ishii		Deputy Director
Yoji	Murayama		Deputy Director
Shuji	Yoshinari		Manager of Administration Section
Masao	Sataka		(Temporary Staff)
Suehiro	Takeuchi		(Temporary Staff)

### Department of Research Reactor and Tandem Accelerator

#### *Tandem Accelerator Section (\*General Manager)*

##### *Scientific Staff*

Akihiko	Osa*
Makoto	Matsuda

##### *Technical Staff*

Susumu	Hanashima	
Shin-ichi	Abe	
Nobuhiro	Ishizaki	
Hidekazu	Tayama	
Takamitsu	Nakanoya	
Hiroshi	Kabumoto	
Masahiko	Nakamura	
Ken-ichi	Kutsukake	
Yoshinori	Otokawa	
Takuhiro	Asozu	
Yoshihiro	Tsukihashi	(Temporary Staff)

##### *Entrusted Operators*

Takahiro	Yoshida	
Takayuki	Ishiguro	(to Jun. 30)
Kazushi	Yamaguchi	
Ryo	Nukaga	(from Jul. 1)
Nobuo	Seki	
Takamasa	Mikami	
Teruo	Onodera	(to Apr. 30)
Hikaru	Nisugi	(to Nov. 30)
Masahiko	Sagawa	(from Dec 1.)

## Department of Radiation Protection

### *Facility Radiation Control Section I*

Katsunori	Sawahata	
Hayato	Hiraga	(to Jan. 31)
Tomoyo	Fukami	
Yumi	Ueno	
Susumu	Kinase	

## Advanced Science Research Center

Sadamichi	Maekawa	Director
Yuichiro	Nagame	Deputy Director
Tomotsugu	Sawai	General Manager of Research Coordination and Promotion Office
Hiroshi	Ikezoe	(Temporary Staff)

## Advanced Science Research Center

### *Research Group for Reactions involving Heavy Nuclei ( \* Group Leader )*

Satoshi	Chiba <sup>*</sup>	
Shin-ichi	Mitsuoka	
Katsuhisa	Nishio	
Ichiro	Nishinaka	
Hiroyuki	Koura	
Yutaka	Utsuno	
Hiroyuki	Makii	
Syuya	Ota	(Post Doc., JSPS)
Tatsuro	Nagayama	(Student)

## Advanced Science Research Center

### *Research Group for Superheavy Elements ( \* Group Leader )*

Matthias	Schädel <sup>*</sup>	
Kazuaki	Tsukada	
Masato	Asai	
Tetsuya K.	Sato	
Atsushi	Toyoshima	
Nozomi	Sato	(Post Doc.)
Kazuhiro	Ooe	(Post Doc.)
Yusuke	Kaneya	(Student)

## Advanced Science Research Center

### *Research Group for Mechanical Control of Materials and Spin Systems*

Satoru	Okayasu	(Deputy Group Leader)
--------	---------	-----------------------

## **Nuclear Technology and Education Center**

Nobuo Shinohara  
Hiroyuki Sugai

## **Nuclear Science and Engineering Directorate**

### ***Innovative Nuclear Science Research Group ( \* Group Leader )***

Hideo	Harada*	
Hideki	Iimura	
Mitsuo	Koizumi	
Kazuyoshi	Furutaka	
Fumito	Kitatani	
Shoji	Nakamura	
Yosuke	Toh	
Atsushi	Kimura	
Kaoru	Hara	(Senior Post Doc.)
Tadahiro	Kin	(Senior Post Doc.)
Futoshi	Minato	(Post Doc.)
Masumi	Oshima	(Temporary Staff)

## **Nuclear Science and Engineering Directorate**

### ***Research Group for Radiation Materials Engineering***

Shiro	Jitsukawa
Norito	Ishikawa
Nariaki	Okubo

## **Quantum Beam Science Directorate**

### ***Neutron Imaging and Activation Analysis Group***

Yuichi	Hatsukawa
--------	-----------

## 9.2 Research Planning and Assessment Committee

<i>Chairman</i>	Kouichiro	Asahi	(Professor, Tokyo Institute of Technology)
<i>Member</i>	Tadashi	Kambara	(Senior Scientist, RIKEN)
	Kenji	Kimura	(Professor, Kyoto University)
	Shigeo	Tomita	(Associate Professor, Tsukuba University)
	Toshiaki	Kaneko	(Professor, Okayama University of Science)
	Hisaaki	Kudo	(Professor, Niigata University)
	Eiji	Ideguchi	(Lecturer, The University of Tokyo)
	Hitoshi	Nakata	(Professor, Chiba University)
	Koichi	Hagino	(Associate Professor, Tohoku University)
	Tomotsugu	Sawai	(Nuclear Science and Engineering Directorate, JAEA)
	Hideo	Harada	(Nuclear Science and Engineering Directorate, JAEA)
	Yuichi	Hatsukawa	(Quantum Beam Science Directorate, JAEA)
	Tetsuro	Ishii	(Dep. Research Reactor and Tandem Accelerator, JAEA)
	Masao	Sataka	(Dep. Research Reactor and Tandem Accelerator, JAEA)
	Kiichi	Hojo	(Advanced Science Research Center, JAEA)
<i>Organizer Secretary</i>	Shin-ichi	Mitsuoka	(Advanced Science Research Center, JAEA)
	Norito	Ishikawa	(Nuclear Science and Engineering Directorate, JAEA)
	Masato	Asai	(Advanced Science Research Center, JAEA)
	Hiroshi	Ikezoe	(Advanced Science Research Center, JAEA)



## **CHAPTER 10**

### **New Research Programs**

10.1 New Research Programs Approved in the FY2011

10.2 New Research Programs Approved in the FY2010

This is a blank page.

**10.1 New Research Programs Approved in the FY2011**

<b>Title</b>	<b>Spokesperson &amp; Affiliation</b>
1. Shape and property control of Zn and ZnO nanoparticles by Swift Heavy Ions *	Hiroshi Amekura National Institute for Materials Science (NIMS)
2. Coulomb excitation experiment of $^{128,130}\text{Xe}$	Mitsuo Koizumi JAEA
3. Development and generalization of $^{211}\text{Rn}/^{211}\text{At}$ generator for long-distance shipping of short-lived radioisotope $^{211}\text{At}$ for medical use	Ichiro Nishinaka JAEA
4. Determination of reduction potential of mendelevium with electrochemistry technique	Atsushi Toyoshima JAEA
5. Study of nuclear transfer process for heavy-ion surrogate method	Shinichi Mitsuoka JAEA
6. Development of on-line $^{99\text{m}}\text{Tc}$ production system using gas phase reaction	Tetsuya Sato JAEA
7. Measurements of grazing angles at energy region around Coulomb barrier for $^{136}\text{Xe} + ^{198}\text{Pt}$	Yutaka Watanabe High Energy Accelerator Research Organization (KEK)
8. Assist-pin effect on critical current density in heavy-ion irradiated high- $T_c$ superconducting thin films *	Tetsuro Sueyoshi Kumamoto University
9. The first ionization potential measurement of Lr and No with a surface ionizer	Nozomi Sato JAEA
10. Fission of proton-rich nuclei in mercury region	Katsuhisa Nishio JAEA
11. Search for highly deformed states in $A=30\sim40$ nuclei	Eiji Ideguchi University of Tokyo
12. Measurement of branching ratio of $^{22}\text{Ne}(\alpha,\gamma)^{26}\text{Mg} / ^{22}\text{Ne}(\alpha,n)^{25}\text{Mg}$ reactions	Shuya Ota JAEA
13. Production of medical radio isotopes using accelerator	Yuichi Hatsukawa JAEA
14. Development of a novel technique for measurement of nuclear data influencing the design of advanced fast reactors: (1) Fission cross section measurement **	Katsuhisa Nishio JAEA

15. Development of a novel technique for measurement of nuclear data influencing the design of advanced fast reactors: (2) Determination of neutron capture cross section **	Hiroyuki Makii JAEA
16. Application of high-aspect-ratio nanoholes formed by etching of latent tracks for sensors *	Makoto Fujimaki National Institute of Advanced Industrial Science and Technology (AIST)

\* Approved as a Common Use Program of JAEA.

\*\* Approved as a JST Innovative Nuclear Research and Development Program entrusted to JAEA.

**10.2 New Research Programs Approved in the FY2010**

<b>Title</b>	<b>Spokesperson &amp; Affiliation</b>
1. Fabrication of optical waveguides by high energy heavy ion implantation *	Tadashi Narusawa Kochi University of Technology
2. Shape and property control of Zn and ZnO nanoparticles by Swift Heavy Ions *	Hiroshi Amekura National Institute for Materials Science (NIMS)
3. Heavy ion irradiation effects on nuclear energy-related oxide materials *	Akihiro Iwase Osaka Prefecture University
4. Gas-phase chemistry of Zr, Hf and Rf chlorides *	Shinichi Goto Niigata University
5. Morphological change in metal nano-particles induced by swift heavy ion irradiation *	Syo Matsumura Kyushu University
6. Study of damage formation process under high-energy fission fragment irradiation fields	Norito Ishikawa JAEA
7. Aqueous chemistry of the group 6th elements in the periodic table as a model experiment for Seaborgium	Kazuaki Tsukada JAEA
8. Investigation of the mass distribution of fission fragments for the reactions of $^{34}\text{S} + ^{208}\text{Pb}$ and $^{36}\text{S} + ^{206}\text{Pb}$	Jadambaa Khuyagbaatar GSI
9. Study of $^{218}\text{U}$ region with near N=126 closed shell	Yasuo Wakabayashi JAEA
10. Development of surrogate technique for determination of neutron capture cross sections	Hiroyuki Makii JAEA
11. Development of gas-cell laser spectroscopy for the measurement of nuclear radii of unstable tungsten isotopes	Hideki Iimura JAEA
12. Experimental assignment of single-particle configurations in superheavy nuclei by means of $\alpha$ fine structure spectroscopy	Masato Asai JAEA
13. Control of electronic and magnetic properties of heavy element oxides by using high density electronic excitation due to swift heavy ions	Akihiro Iwase Osaka Prefecture University
14. Electronic excitation effects and material modifications of non-metallic ceramics by high-energy ions	Noriaki Matsunami Nagoya University
15. Charge state evolution and energy loss of heavy ions passing through foil targets	Makoto Imai Kyoto University

16. Metal-semiconductor transition control on a FeSi <sub>2</sub> thin film with high energy heavy ion irradiations	Masato Sasase Wakasa-wan Energy Research Center (WERC)
17. Nano-fabrication of zeolite with high energy ion irradiations	Yukichi Sasaki Japan Fine Ceramics Center (JFCC)
18. Functional and structural properties of ceramic materials after high energy irradiation	Nariaki Okubo JAEA
19. Coulomb excitation experiment of <sup>126</sup> Xe	Mitsuo Koizumi JAEA
20. Fission fragment anisotropy in heavy-ion-induced fission of actinides	Ichiro Nishinaka JAEA
21. Study for quasi-fission process in the heavy-ion reactions using <sup>238</sup> U target nucleus (2)	Katsuhisa Nishio JAEA
22. Proton configuration of <sup>261</sup> Db	Masato Asai JAEA
23. Benchmark experiment of surrogate ratio method for neutron capture	Shengquan Yan China Institute of Atomic Energy (CIAE)
24. Development of experimental techniques for surrogate method using heavy-ion reactions	Tetsuro Ishii JAEA
25. Production of medical radio isotopes using accelerator	Yuichi Hatsukawa JAEA
26. Development of the accelerator system and the inventive ion beam application	Makoto Matsuda JAEA

\* Approved as a Common Use Program of JAEA.

# 国際単位系（SI）

表1. SI 基本単位

基本量	SI 基本単位	
	名称	記号
長さ	メートル	m
質量	キログラム	kg
時間	秒	s
電流	アンペア	A
熱力学温度	ケルビン	K
物質モル		mol
光度	カンデラ	cd

表2. 基本単位を用いて表されるSI組立単位の例

組立量	SI 基本単位	
	名称	記号
面積	平方メートル	m <sup>2</sup>
体積	立方メートル	m <sup>3</sup>
速度	メートル毎秒	m/s
加速度	メートル毎秒毎秒	m/s <sup>2</sup>
波数	数メートル	m <sup>-1</sup>
密度, 質量密度	キログラム毎立方メートル	kg/m <sup>3</sup>
面積密度	キログラム毎平方メートル	kg/m <sup>2</sup>
比体積	立方メートル毎キログラム	m <sup>3</sup> /kg
電流密度	アンペア毎平方メートル	A/m <sup>2</sup>
電界の強さ	アンペア毎メートル	A/m
量濃度 <sup>(a)</sup> , 濃度	モル毎立方メートル	mol/m <sup>3</sup>
質量濃度	キログラム毎立法メートル	kg/m <sup>3</sup>
輝度	カンデラ毎平方メートル	cd/m <sup>2</sup>
屈折率 <sup>(b)</sup>	(数字の) 1	1
比誘電率 <sup>(b)</sup>	(数字の) 1	1

- (a) 量濃度 (amount concentration) は臨床化学の分野では物質濃度 (substance concentration) ともよばれる。  
(b) これらは無次元量あるいは次元1をもつ量であるが、そのことを表す単位記号である数字の1は通常は表記しない。

表3. 固有の名称と記号で表されるSI組立単位

組立量	SI 組立単位			
	名称	記号	他のSI単位による表し方	SI基本単位による表し方
平面角	ラジアン <sup>(b)</sup>	rad	1 <sup>(b)</sup>	m/m
立体角	ステラジアン <sup>(b)</sup>	sr <sup>(c)</sup>	1 <sup>(b)</sup>	m <sup>2</sup> /m <sup>2</sup>
周波数	ヘルツ <sup>(d)</sup>	Hz		s <sup>-1</sup>
力	ニュートン	N		m kg s <sup>-2</sup>
圧力, 応力	パスカル	Pa	N/m <sup>2</sup>	m <sup>-1</sup> kg s <sup>-2</sup>
エネルギー, 仕事, 熱量	ジュール	J	N m	m <sup>2</sup> kg s <sup>-2</sup>
仕事率, 工率, 放射	ワット	W	J/s	m <sup>2</sup> kg s <sup>-3</sup>
電荷, 電気量	クーロン	C		s A
電位差 (電圧), 起電力	ボルト	V	W/A	m <sup>2</sup> kg s <sup>-3</sup> A <sup>-1</sup>
静電容量	ファラド	F	C/V	m <sup>-2</sup> kg <sup>-1</sup> s <sup>4</sup> A <sup>2</sup>
電気抵抗	オーム	Ω	V/A	m <sup>2</sup> kg s <sup>-3</sup> A <sup>-2</sup>
コンダクタンス	ジーメンズ	S	A/V	m <sup>-2</sup> kg <sup>-1</sup> s <sup>3</sup> A <sup>2</sup>
磁束密度	ウェーバ	Wb	Vs	m <sup>2</sup> kg s <sup>-2</sup> A <sup>-1</sup>
磁束	テスラ	T	Wb/m <sup>2</sup>	kg s <sup>-2</sup> A <sup>-1</sup>
インダクタンス	ヘンリー	H	Wb/A	m <sup>2</sup> kg s <sup>-2</sup> A <sup>-2</sup>
セルシウス温度	セルシウス度 <sup>(e)</sup>	°C		K
光束流	ルーメン	lm		cd sr <sup>(c)</sup>
照射度	ルクス	lx	lm/m <sup>2</sup>	m <sup>-2</sup> cd
放射性核種の放射能 <sup>(f)</sup>	ベクレル <sup>(d)</sup>	Bq		s <sup>-1</sup>
吸収線量, 比エネルギー分与, カーマ	グレイ	Gy	J/kg	m <sup>2</sup> s <sup>-2</sup>
線量当量, 周辺線量当量, 方向性線量当量, 個人線量当量	シーベルト <sup>(g)</sup>	Sv	J/kg	m <sup>2</sup> s <sup>-2</sup>
酸素活性	カタール	kat		s <sup>-1</sup> mol

- (a)SI接頭語は固有の名称と記号を持つ組立単位と組み合わせても使用できる。しかし接頭語を付した単位はもはやコヒーレントではない。  
(b)ラジアンとステラジアンは数字の1に対する単位の特別な名称で、量についての情報をつたえるために使われる。実際には、使用する時には記号rad及びsrが用いられるが、習慣として組立単位としての記号である数字の1は明示されない。  
(c)測光学ではステラジアンという名称と記号srを単位の表し方の中に、そのまま維持している。  
(d)ヘルツは周期現象についてのみ、ベクレルは放射性核種の統計的過程についてのみ使用される。  
(e)セルシウス度はケルビンの特別な名称で、セルシウス温度を表すために使用される。セルシウス度とケルビンの単位の大きさは同一である。したがって、温度差や温度間隔を表す数値はどちらの単位で表しても同じである。  
(f)放射性核種の放射能 (activity referred to a radionuclide) は、しばしば誤った用語で"radioactivity"と記される。  
(g)単位シーベルト (PV,2002,70,205) についてはCIPM勧告2 (CI-2002) を参照。

表4. 単位の中に固有の名称と記号を含むSI組立単位の例

組立量	SI 組立単位		
	名称	記号	SI 基本単位による表し方
粘着力のモーメント	パスカル秒	Pa s	m <sup>-1</sup> kg s <sup>-1</sup>
表面張力	ニュートンメートル	N m	m <sup>2</sup> kg s <sup>-2</sup>
角速度	ニュートン毎メートル	N/m	kg s <sup>-2</sup>
角加速度	ラジアン毎秒	rad/s	m m <sup>-1</sup> s <sup>-1</sup> =s <sup>-1</sup>
熱流密度, 放射照度	ラジアン毎秒毎秒	rad/s <sup>2</sup>	m m <sup>-1</sup> s <sup>-2</sup> =s <sup>-2</sup>
熱容量, エントロピー	ワット毎平方メートル	W/m <sup>2</sup>	kg s <sup>-3</sup>
比熱容量, 比エントロピー	ジュール毎ケルビン	J/K	m <sup>2</sup> kg s <sup>-2</sup> K <sup>-1</sup>
比エネルギー	ジュール毎キログラム毎ケルビン	J/(kg K)	m <sup>2</sup> s <sup>-2</sup> K <sup>-1</sup>
熱伝導率	ジュール毎キログラム	J/kg	m <sup>2</sup> s <sup>-2</sup>
体積エネルギー	ワット毎メートル毎ケルビン	W/(m K)	m kg s <sup>-3</sup> K <sup>-1</sup>
電界の強さ	ジュール毎平方メートル	J/m <sup>3</sup>	m <sup>-1</sup> kg s <sup>-2</sup>
電荷密度	ジュール毎メートル	V/m	m kg s <sup>-3</sup> A <sup>-1</sup>
電荷密度	クーロン毎立方メートル	C/m <sup>3</sup>	m <sup>-3</sup> sA
表面電荷	クーロン毎平方メートル	C/m <sup>2</sup>	m <sup>-2</sup> sA
電束密度, 電気変位	クーロン毎平方メートル	C/m <sup>2</sup>	m <sup>-2</sup> sA
誘電率	ファラド毎メートル	F/m	m <sup>-3</sup> kg <sup>-1</sup> s <sup>4</sup> A <sup>2</sup>
透磁率	ヘンリー毎メートル	H/m	m kg s <sup>-2</sup> A <sup>-2</sup>
モルエネルギー	ジュール毎モル	J/mol	m <sup>2</sup> kg s <sup>-2</sup> mol <sup>-1</sup>
モルエントロピー, モル熱容量	ジュール毎モル毎ケルビン	J/(mol K)	m <sup>2</sup> kg s <sup>-2</sup> K <sup>-1</sup> mol <sup>-1</sup>
照射線量 (X線及びγ線)	クーロン毎キログラム	C/kg	kg <sup>-1</sup> sA
吸収線量	グレイ毎秒	Gy/s	m <sup>2</sup> s <sup>-3</sup>
放射強度	ワット毎ステラジアン	W/sr	m <sup>3</sup> m <sup>-2</sup> kg s <sup>-3</sup> =m <sup>2</sup> kg s <sup>-3</sup>
放射輝度	ワット毎平方メートル毎ステラジアン	W/(m <sup>2</sup> sr)	m <sup>2</sup> m <sup>-2</sup> kg s <sup>-3</sup> =kg s <sup>-3</sup>
酵素活性濃度	カタール毎立方メートル	kat/m <sup>3</sup>	m <sup>-3</sup> s <sup>-1</sup> mol

表5. SI 接頭語

乗数	接頭語	記号	乗数	接頭語	記号
10 <sup>24</sup>	ヨタ	Y	10 <sup>-1</sup>	デシ	d
10 <sup>21</sup>	ゼタ	Z	10 <sup>-2</sup>	センチ	c
10 <sup>18</sup>	エクサ	E	10 <sup>-3</sup>	ミリ	m
10 <sup>15</sup>	ペタ	P	10 <sup>-6</sup>	マイクロ	μ
10 <sup>12</sup>	テラ	T	10 <sup>-9</sup>	ナノ	n
10 <sup>9</sup>	ギガ	G	10 <sup>-12</sup>	ピコ	p
10 <sup>6</sup>	メガ	M	10 <sup>-15</sup>	フェムト	f
10 <sup>3</sup>	キロ	k	10 <sup>-18</sup>	アト	a
10 <sup>2</sup>	ヘクト	h	10 <sup>-21</sup>	ゼプト	z
10 <sup>1</sup>	デカ	da	10 <sup>-24</sup>	ヨクト	y

表6. SIに属さないが、SIと併用される単位

名称	記号	SI 単位による値
分	min	1 min=60s
時	h	1 h =60 min=3600 s
日	d	1 d=24 h=86 400 s
度	°	1°=(π/180) rad
分	′	1′=(1/60)°=(π/10800) rad
秒	″	1″=(1/60)′=(π/648000) rad
ヘクタール	ha	1ha=1hm <sup>2</sup> =10 <sup>4</sup> m <sup>2</sup>
リットル	L, l	1L=1l=1dm <sup>3</sup> =10 <sup>3</sup> cm <sup>3</sup> =10 <sup>-3</sup> m <sup>3</sup>
トン	t	1t=10 <sup>3</sup> kg

表7. SIに属さないが、SIと併用される単位で表される数値が実験的に得られるもの

名称	記号	SI 単位で表される数値
電子ボルト	eV	1eV=1.602 176 53(14)×10 <sup>-19</sup> J
ダルトン	Da	1Da=1.660 538 86(28)×10 <sup>-27</sup> kg
統一原子質量単位	u	1u=1 Da
天文単位	ua	1ua=1.495 978 706 91(6)×10 <sup>11</sup> m

表8. SIに属さないが、SIと併用されるその他の単位

名称	記号	SI 単位で表される数値
バール	bar	1 bar=0.1MPa=100kPa=10 <sup>5</sup> Pa
水銀柱ミリメートル	mmHg	1mmHg=133.322Pa
オングストローム	Å	1 Å=0.1nm=100pm=10 <sup>-10</sup> m
海里	M	1 M=1852m
バイン	b	1 b=100fm <sup>2</sup> =(10 <sup>-12</sup> cm <sup>2</sup> )2=10 <sup>-28</sup> m <sup>2</sup>
ノット	kn	1 kn=(1852/3600)m/s
ネーパ	Np	SI単位との数値的な関係は、 対数量の定義に依存。
ベベル	B	
デジベル	dB	

表9. 固有の名称をもつCGS組立単位

名称	記号	SI 単位で表される数値
エルグ	erg	1 erg=10 <sup>-7</sup> J
ダイン	dyn	1 dyn=10 <sup>-5</sup> N
ポアズ	P	1 P=1 dyn s cm <sup>-2</sup> =0.1Pa s
ストークス	St	1 St =1cm <sup>2</sup> s <sup>-1</sup> =10 <sup>-4</sup> m <sup>2</sup> s <sup>-1</sup>
スチルブ	sb	1 sb =1cd cm <sup>-2</sup> =10 <sup>-4</sup> cd m <sup>-2</sup>
フォトリ	ph	1 ph=1cd sr cm <sup>-2</sup> 10 <sup>4</sup> lx
ガリ	Gal	1 Gal =1cm s <sup>-2</sup> =10 <sup>-2</sup> ms <sup>-2</sup>
マクスウェル	Mx	1 Mx = 1G cm <sup>2</sup> =10 <sup>-8</sup> Wb
ガウス	G	1 G =1Mx cm <sup>-2</sup> =10 <sup>-4</sup> T
エルステッド <sup>(c)</sup>	Oe	1 Oe ≐ (10 <sup>7</sup> /4π)A m <sup>-1</sup>

- (c) 3 元素のCGS単位系とSIでは直接比較できないため、等号「≐」は対応関係を示すものである。

表10. SIに属さないその他の単位の例

名称	記号	SI 単位で表される数値
キュリー	Ci	1 Ci=3.7×10 <sup>10</sup> Bq
レントゲン	R	1 R = 2.58×10 <sup>-4</sup> C/kg
ラド	rad	1 rad=1cGy=10 <sup>-2</sup> Gy
レム	rem	1 rem=1 cSv=10 <sup>-2</sup> Sv
ガンマ	γ	1 γ =1 nT=10 <sup>-9</sup> T
フェルミ	f	1フェルミ≐1 fm=10 <sup>-15</sup> m
メートル系カラット		1メートル系カラット = 200 mg = 2×10 <sup>-4</sup> kg
トル	Torr	1 Torr = (101 325/760) Pa
標準大気圧	atm	1 atm = 101 325 Pa
カロリ	cal	1cal=4.1858J (「15℃」カロリー) , 4.1868J (「IT」カロリー) 4.184J (「熱化学」カロリー)
ミクロン	μ	1 μ =1μm=10 <sup>-6</sup> m

